Theoretical and experimental studies of runaway electrons in the TEXTOR tokamak

S.S. Abdullaev, K.H. Finken, K. Wongrach, O. Willi

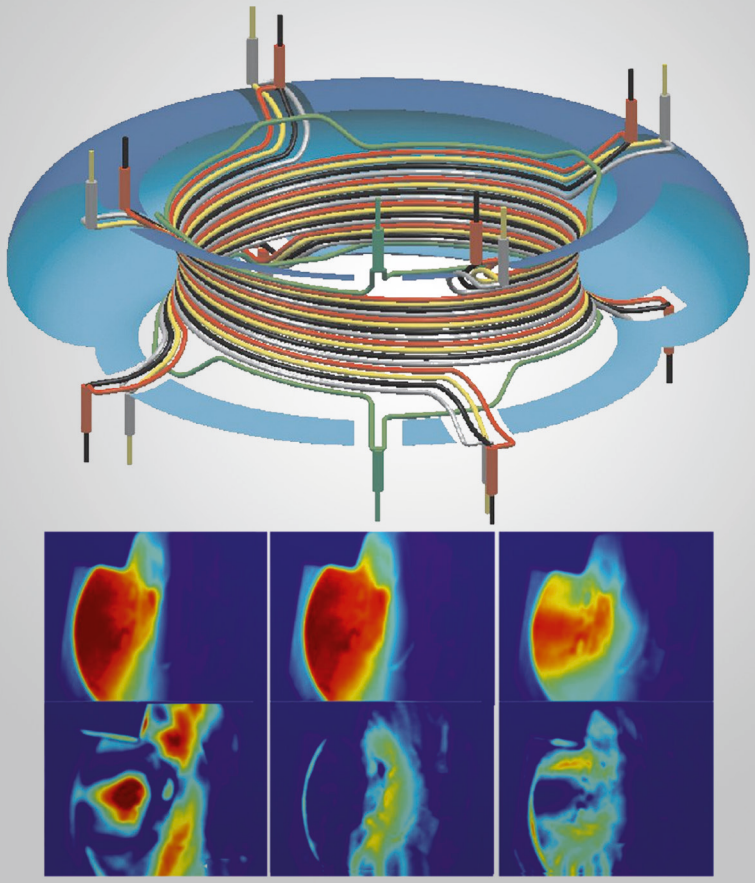

Energie & Umwelt/
Energy & Environment
Band/ Volume 318
ISBN 978-3-95806-140-8

JÜLICH
FORSCHUNGSZENTRUM

Schriften des Forschungszentrums Jülich
Reihe Energie & Umwelt / Energy & Environment Band / Volume 318

Forschungszentrum Jülich GmbH
Institute of Energy and Climate Research
Plasma Physics IEK-4

Theoretical and experimental studies of runaway electrons in the TEXTOR tokamak

S.S. Abdullaev, K.H. Finken, K. Wongrach, O. Willi

Schriften des Forschungszentrums Jülich
Reihe Energie & Umwelt / Energy & Environment Band / Volume 318

ISSN 1866-1793 ISBN 978-3-95806-140-8

Bibliographic information published by the Deutsche Nationalbibliothek.
The Deutsche Nationalbibliothek lists this publication in the Deutsche Nationalbibliografie; detailed bibliographic data are available in the Internet at http://dnb.d-nb.de.

Publisher and Distributor: Forschungszentrum Jülich GmbH
Zentralbibliothek
52425 Jülich
Tel: +49 2461 61-5368
Fax: +49 2461 61-6103
Email: zb-publikation@fz-juelich.de
www.fz-juelich.de/zb

Cover Design: Grafische Medien, Forschungszentrum Jülich GmbH

Printer: Grafische Medien, Forschungszentrum Jülich GmbH

Schriften des Forschungszentrums Jülich
Reihe Energie & Umwelt / Energy & Environment, Band / Volume 318

ISSN 1866-1793
ISBN 978-3-95806-140-8

The complete volume is freely available on the Internet on the Jülicher Open Access Server (JuSER) at www.fz-juelich.de/zb/openaccess.

Summary. Theoretical and experimental studies of runaway electrons in tokamaks and their mitigations, particularly the recent studies performed by a group of the Heinrich-Heine University Düsseldorf in collaboration with the Institute of Energy and Climate Research of the Research Centre (Forschungszentrum) of Jülich are reviewed. The main topics focus on (*i*) runaway generation mechanisms, (*ii*) runaway orbits in equilibrium plasma, (*iii*) transport in stochastic magnetic fields, (*iv*) diagnostics and investigations of transport of runaway electron and their losses in low density discharges (*v*) runaway electrons during plasma disruptions, and (*vi*) runaway mitigation methods. The development of runaway diagnostics enables the measurement of runaway electrons in both the centre and edge of the plasma. The diagnostics provide an absolute runaway energy resolved measurement, the radial decay length of runaway electrons and, the structure and dynamics of runaway electron beams. The new mechanism of runaway electron formation during plasma disruptions is discussed.

In dieser Zusammenfassung werden experimentelle und theoretische Untersuchungen zur Erzeugung von hochenergetischen Runaway-Elektronen und die Abschwächung ihrer schädlichen Effekte beschrieben, die durch eine Gruppe an der Heinrich Heine Universität in Düsseldorf in Zusammenarbeit mit dem Institut für Energie und Klimaforschung des Forschungszentrums Jülich durchgeführt wurden. Der Hauptaugenmerk liegt bei dem Erzeugungsmechanismus der Runaway Elektronen (*i*), bei der Untersuchung des Transportes und des Verlustes dieser Elektronen in Niedrig–Dichte–Entladungen (*ii*) der Analyse der Runaway-Bahnen in Gleichgewichts-Plasmen, (*iii*) dem Transport in stochastischen Magnetfeldern, (*iv*) den Diagnostiken und dem Transport und Verlust bei Niedrig-Dichte-Entladungen, (*v*) den Runaway-Elektronen bei Plasmadisruptionen und (*vi*) bei der Entwicklung von Methoden, um die schädlichen Auswirkungen der Runaway–Elektronen abzumildern (*iii*). Die Entwicklung neuer Diagnostiken erlaubt die Messung der Runaways sowohl im Entladungszentrum als auch am Rand; sie erlauben eine Messung der Runaway–Energieverteilung, der radialen Verteilung der Runaways sowie der Struktur und der Dynamik des Runaway–Strahls. Das theoretiesche Verfahren, das entwickelt wurde um den Transport und den Verlust der Runaways zu beschreiben, wird ebenfalls kurz diskutiert.

Contents

List of main notations

(R, Z, φ)	cylindrical coordinates
(r, θ, φ)	quasitoroidal coordinates
$\mathbf{A}$	vector potential of a magnetic field
(A_R, A_Z, A_φ)	components of a vector potential
ε_0	vacuum permittivity (electric constant)
$\mathcal{E}$	toroidal electric field
$\mathbf{B}$	magnetic field vector
(B_R, B_Z, B_φ)	components of a magnetic field
R_0	major radius of torus center
B_0	magnitude of the toroidal magnetic field at the torus center
I_p	plasma current
ρ	minor radius of magnetic surfaces
$\psi \equiv \psi_\varphi$	poloidal magnetic flux
ψ_t	toroidal magnetic flux
ϑ	poloidal angle in which field lines are straight
φ	toroidal angle
$q(\psi)$	safety factor
$q_p(J, E)$	effective safety factor
(m, n)	poloidal and toroidal mode numbers
γ	relativistic factor
c	speed of light in vacuum
m_e	electron mass
e	elementary charge
Z_q	particle charge [in unit e]
$\omega_0 = eB_0/m_e c$	reference electron gyrofrequency
$E_{ref} = m_e \omega_0^2 R_0^2$	the reference energy

$E = m_e c^2 \gamma$	full electron energy
$E_k = m_e c^2 (\gamma - 1)$	kinetic energy
$e_0 = m_e c^2 / E_{ref}$	normalized electron energy at rest
ϵ	dimensionless perturbation parameter
D_r	radial diffusion coefficient

1 Introduction

In tokamaks, electrons gain energies from the induced toroidal electric field. However, they also lose energy in collisions. The high energy electrons have a lower collision cross section than the low energy ones. Therefore, a group of electrons called "runaway electrons (REs)" can gain such a high energy that the drag force by collisions is smaller than the electrical force. They are freely accelerated up to relativistic energies. In the normal operating regime of the present day tokamaks REs are rarely generated because the typical toroidal electric field is less than the critical field for RE generation, below which RE generation is not possible [1, 2, 3]. Additionally, the toroidal magnetic field is low, i.e. close to the minimum magnetic field strength required for runaway generation, $B_t \approx 2$ T and the low plasma current results in the low runaway avalanche gain. In the low-density regime as well as during disruptions, observations of REs have been reported in several present day tokamaks [4, 5, 6, 7, 8, 9]. Not only in tokamaks or fusion plasmas, REs are also found in astrophysics [10] and in lightning [11].

Since REs in tokamaks, especially during disruptions, can gain energies up to several tens of MeVs, they become an important threat to the plasma facing components. The lost REs hit the plasma facing components locally and may cause severe damage to the components [12]. Effect of the REs becomes more crucial in the next generation tokamak such as ITER as they are expected to gain energies upto a few hundreds of MeVs during plasma disruptions [13]. Several techniques have been proposed in order for runaway mitigation. Massive gas injection (MGI) is commonly used due to its straightforward implementation. A number of experimental researches on tokamak disruptions [14, 15, 16, 17, 18] have been conducted to investigate the effect of massive gas injection (MGI) on the runaway suppression in different machines. Enormous amounts of neutral gas ($>10^{21}$ atoms) are injected into the vacuum vessel. The REs are collisionally suppressed by an increased density at the start of the current quench [19]. Main drawbacks of this technique is the slow impurity delivery and a poor mixing efficiency [16]. Moreover, the injection hardware and technologies available to date are not capable of complete runaway suppression during tokamak disruptions.

An alternative concept for mitigation of REs is to deconfine the REs before they have time to gain high energies from the induced toroidal electric

fields. Perturbation fields which cause an enhancement of the RE loss can be initiated, e.g. by externally applied non-axisymmetric magnetic fields. The perturbation fields are resonant with the specific magnetic surface giving rise to the ergodization. In the ergodic layer, the radial transport of the particles is enhanced [20, 21]. The position control of the runaway beam is an attractive option in case the applied runaway mitigation methods fail and a large number of high energy REs are generated. Control of the runaway beam position has been demonstrated in Tore-Supra [22], DIII-D [23] and TEXTOR [24]. The interaction between runaway beam and the wall can be minimized by keeping the beam within the "safe zone". This offers an opportunity to apply other mitigation methods such as massive gas injection and runaway current ramp-down to dissipate the runaway energy.

This work reviews the theoretical and experimental studies of REs in the TEXTOR tokamak performed during the last decade by the group at Heinrich-Heine University Düsseldorf in collaboration with the Institute of Energy and Climate Research of the Research Centre (Forschungszentrum) of Jülich. The studies on the REs carried out in this tokamak in the 1990s are summarized in the theses by R. Jaspers [25] and I. Entrop [26].

The present review consists of main eight chapters and four supplementary sections, appendices. The theoretical studies of REs are presented in the first three chapters. The next three chapters are devoted to the description of experimental studies of REs carried out in the TEXTOR tokamak.

We have briefly presented the mechanisms of the RE generations in chapter 2. The main features of RE orbits in equilibrium plasmas are discussed in chapter 3. Particularly we describe a new effect of outward drift of electron orbits induced by the toroidal electric field. The radial transport of REs in tokamak plasmas is discussed in chapter 4. There we present the Hamiltonian equation of guiding–center motion in a stochastic magnetic field, the onset of global chaotic motion, and the quasilinear diffusion of REs. Particularly, we describe the asymptotical theory of RE transport in a turbulent magnetic field and the fractional nature of RE diffusion established by direct numerical simulations. The main features of the interaction of REs with large–scale magnetic perturbations are discussed in Sec. 4.6. In Sec. 4.6.1 we consider the chaotic dynamics of REs affected by the dynamic ergodic divertor (DED) of the TEXTOR tokamak in two regimes: in a steady–state operation and post–disruption regimes. The effect of magnetic perturbations of the internal magnetohydrodynamical (MHD) modes on REs is discussed in Sec. 4.6.2. The analytical models of a tokamak plasma and magnetic perturbations, particularly, the TEXTOR-DED employed in these sections are given in Appendices A and B.

Diagnostic techniques, i.e., synchrotron radiation and the scintillator, heat load, and calorimeter probes developed by our group for the experimental study of REs are described in chapter 5. The experimental studies of REs in the low density regime is presented in chapter 6. There we describe the

radial transport of REs, it's dependence on the level magnetic turbulence, and the effect of the TEXTOR-DED. The experimental studies of REs generated during plasma disruptions are presented in chapter 7. They include measurements of RE energies by the calorimeter probe, the impact of REs on the heat load probe, synchrotron radiation patterns, the mitigations of REs by the massive gas injection and the applied resonant magnetic perturbations (RMPs) created by the TEXTOR–DED.

In chapter 8 a brief description of the recently proposed mechanism of RE formation during a plasma disruption is given. There we describe the main conjecture of RE formation, and present the experimental evidences supporting it. Possible generic structures of stochastic magnetic field during a plasma disruption is studied in Appendix C. The theoretical treatment of the related heat and particle transport in a stochastic magnetic field is given in Appendix D. Finally, all theoretical and experimental results on RE studies presented in the review are summarized in Sec. 9.

Acknowledgments

This work was supported by the Royal Thai Government, an R&D contract, the Trilateral Euregio Cluster (TEC), and the DFG program GRK 1203. The authors thank Dr. M. Forster, Dr. T. Kudyakov and the TEXTOR team for their support.

2 Generation of REs in tokamaks

The first theoretical analysis of RE generation has been performed by Dreicer [1, 2]. The Dreicer generation is a primary runaway generation which can be observed both in the low density regime and during the disruption. The hot tail generation is expected to play important role during disruptions when the thermal quench is sufficiently rapid. Tritium decay and Compton scattering may also lead to primary RE generation. REs can be generated by the primary generation mechanisms even if there were no runaways in the plasma. Runaway avalanche which is a secondary runaway generation mechanism, in contrast, occurs only if REs already exist in the plasma.

2.1 Primary generation mechanism

This mechanism of electron acceleration in plasmas, referred as the Dreicer mechanism is a relatively simple (see, e.g., [27, 53]). In the presence of electric field $\mathcal{E}$ an electron is accelerated due to the the electrical force, $F_e = e\mathcal{E}$. However, this motion is slowed down by by electron–electron and electron–ion collisions. The collision frequency ν decreases with electron velocity v as $\nu(v) = n_e e^4 \ln \Lambda / 4\pi\varepsilon_0^2 m_e^2 v^3 \propto v^{-3}$, where n_e is the electron density, $\ln \Lambda$ the Coulomb logarithm and ε_0 the vacuum permittivity (or electric constant), m_e is the electron mass, and c is the velocity of light in a vacuum. Therefore the corresponding friction force $F_{fr}(v) = m_e \nu(v) v$ decreases with increasing electron velocity v as $F_{fr}(v) \propto v^{-2}$. By setting the electrical force, F_e, equal to the friction force $F_{fr}(v)$, we obtain the critical velocity v_c,

$$v_c^2(\mathcal{E}) = \frac{n_e e^3 \ln \Lambda}{4\pi\varepsilon_0^2 m_e \mathcal{E}}, \tag{2.1}$$

above which ($v > v_c$) electrons would accelerate. For the weak electric field, only high-energy part of the Maxwell distribution is accelerated and runs away. REs occur even for the electrons with the thermal velocity $v = v_T$ if the electric field $\mathcal{E}$ exceeds the critical (Dreicer) field $\mathcal{E}_D$ determined by the condition $v_c^2(\mathcal{E}_D) = v_T^2 = T_e/m_e$,

$$\mathcal{E}_D = \frac{n_e e^3 \ln \Lambda}{4\pi\varepsilon_0^2 T_e}, \tag{2.2}$$

where T_e is the electron temperature of plasma.

The determination of RE birth rate, $\lambda_r = dn_r^{pr}/dt$, where n_r^{pr} is the density of REs, by this mechanism has been studied in several works (see references in [3, 27, 28]). The most correct formula for λ_r obtained in the non–relativistic approach reads as

$$\lambda_r = k\nu n_e \left(\frac{\mathcal{E}}{\mathcal{E}_D}\right)^{-3(1+Z_{eff})/16} \exp\left(-\frac{\mathcal{E}}{4\mathcal{E}_D} - \sqrt{\frac{\mathcal{E}(1+Z_{eff})}{\mathcal{E}_D}}\right), \qquad (2.3)$$

where k is a factor of order unity, Z_{eff} is the effective ion charge. It predicts exponentially small in $\mathcal{E}/\mathcal{E}_D$ RE birth rate.

The relativistic effects significantly change the RE birth rate [3]. Particularly, in the limit $\mathcal{E}/\mathcal{E}_D \gg T_e/m_e c^2$ the birth rate of REs becomes

$$\lambda_r^{rel} \approx \lambda_r \exp\left(-\frac{T_e}{m_e c^2}\left[\frac{\mathcal{E}^2}{8\mathcal{E}_D^2} + \frac{2\sqrt{1+Z_{eff}}}{3}\left(\frac{\mathcal{E}}{\mathcal{E}_D}\right)^{3/2}\right]\right). \qquad (2.4)$$

The friction force does not fall to zero but remains finite at the speed of light. The RE birth rate in both cases depends on the electric field $\mathcal{E}$, electron density n_e, electron temperature T_e and effective ion charge Z_{eff}.

2.2 Hot tail generation

Since the collision frequency decreases with increasing velocity, the high energy electrons need longer times to slow down than low energy ones. During the transient event such as the thermal quench in a disruption, the high energy electrons may not have enough time for complete thermalization and form a hot tail of the Maxwellian distribution with a decreasing temperature of the rest of the distribution [29]. As the plasma cools down, the critical velocity for runaway acceleration decreases. The electrons in this hot tail can thus become REs resulting in a rapid growth of the runaway population.

In [30, 31, 32] the hot tail runaway generation has been analyzed for certain plasma cooling models. The cooling rate is assumed to be proportional to the collision frequency of thermal electrons. At low temperature in a post-thermal quench the cooling rate is constant or decreasing with time. The hot tail runaway generation for general cooling scenarios is given by

$$\frac{dn_r^{hot}}{dt} \simeq -\frac{du_c}{dt}\frac{2u_c^2 H(-du_c/dt)}{(u_c^3 - 3\tau)^{1/3}} \int_{u_c}^{\infty} \frac{e^{-u^2}u^2 du}{(u_c^3 - 3\tau)^{2/3}}, \qquad (2.5)$$

where $u_c = (v_c^3/v_T^3 + 3\tau)^{1/3}$, $H(x)$ is the Heaviside function, and τ is the time–dependent parameter given by $\tau = \nu_0 \int_0^t n(t)/n_0 dt$, where n_0 is the initial electron density and ν_0 is the initial collision frequency ν. The parameter τ

can be approximated as $\tau(t) \approx H(t-t_*)(n_f/n_0)\nu_0(t-t_*)$, where n_f is the final thermal electron density, $t_* \approx t_0$ is the thermal quench time.

An experimental study of the hot tail generation was performed in DIII-D [33]. It has been found that during the disruption induced by killer pellet injection, the cooling rate and the final temperature of the plasma has significant influence on the RE generation. The experimental evidence of hot tail RE generation has been recently identified during plasma disruptions in the TEXTOR tokamak [34].

2.3 Runaway avalanche

As the generation rate in Eq. (2.3) is exponentially small in the ratio $\mathcal{E}/\mathcal{E}_D$, the RE generation is negligible for $\mathcal{E}/\mathcal{E}_D \lesssim 0.03$ [27]. Another production mechanism which is more effective was pointed out by Sokolov [35]. Although a close Coulomb collision, i.e. "hard" collision, has a small probability in plasmas with $\ln\Lambda \gg 1$, this collision can kick a thermal electron into the runaway region while the colliding RE still stays in the runaway region. The runaway population grows exponentially due to this mechanism, referred as "secondary" runaway generation or runaway avalanche.

Many studies have been devoted to an analysis of runaway avalanche [36, 37, 38]. The most complete mathematical treatment of the runaway avalanching process was done by Rosenbluth and Putvinski [38]. The gyrokinetic relativistic Fokker-Planck equation for the evolution of the electron distribution function $f \equiv f(p,\lambda,t)$ averaged over a particle bounce period reads as (see, e.g., [39])

$$\frac{\partial f}{\partial t} - \frac{e\mathcal{E}_\parallel \xi}{m_e c}\left(\frac{\partial f}{\partial p} - \frac{2\lambda}{p}\frac{\partial f}{\partial \lambda}\right) = C(f) + S, \tag{2.6}$$

where $p = \gamma v/c$ is the normalized relativistic momentum, $\gamma = 1/\sqrt{1-v^2/c^2}$ is the relativistic factor, $\lambda = (1-\xi^2)B/B_{max}$ the magnetic moment variable, $\xi = p_\parallel/p$, B_{max} is the maximum value of the magnetic field on the flux surface. In (2.6) the term $C(f)$ describes the Fokker–Plank collision operator, and the source term S describes the production of fast electrons by close collisions of REs with slow electrons.

In [38] the stationary solutions ($\partial f/\partial t \equiv 0$) of (2.6) were obtained analytically in several limits. An interpolation formula for the runaway production rate due to the secondary generation is given by

$$\frac{dn_r^{sec}}{dt} \simeq n_r \nu_{rel} \frac{(\mathcal{E}/\mathcal{E}_c - 1)}{\ln\Lambda}\sqrt{\frac{\pi\phi}{3(Z_{eff}+5)}} \times \left(1 - \frac{\mathcal{E}_c}{\mathcal{E}} + \frac{4\pi(Z_{eff}+1)^2}{3\phi(Z_{eff}+5)(\mathcal{E}^2/\mathcal{E}_c^2 + 4/\phi^2 - 1)}\right)^{-1/2}, \tag{2.7}$$

where $\mathcal{E}_c = m_e c \nu_{rel}/e$ is the critical electric field, $\nu_{rel} = (v/c)^3 \nu$ is the collision frequency for relativistic electrons, and $\phi \approx \left[1 + 1.46(r/R)^{1/2} + 1.72 r/R\right]^{-1}$ describes the effect of finite aspect ratio R/r. In the limit $\mathcal{E}/\mathcal{E}_c \gg 1$, $Z_{eff} = 1$ and $r/R \to 0$, the simpler growth rate is obtained:

$$\frac{dn_r^{sec}}{dt} \simeq n_r \nu_{rel} \sqrt{\frac{\pi}{2}} \left(\frac{\mathcal{E}/\mathcal{E}_c - 1}{3 \ln \Lambda} \right). \tag{2.8}$$

The secondary generation rate is proportional to the product of the density of the existing REs n_r and the frequency of hard collisions $\nu_{rel}/\ln \Lambda$. The avalanche growth time is $t_{av} \sim \nu_{rel}^{-1} \ln \Lambda \, (\mathcal{E}_c/\mathcal{E})$. Runaway avalanche is dominant at a sufficiently weak electric field if there are REs present in the plasma. When a considerable fraction of the initial current is converted to the runaway current, the electric field decreases and the runaway current becomes saturated before it reaches the initial current [40].

The observation in ohmic low density discharges of the TEXTOR tokamak [41] has been interpreted as the first experimental evidence of the runaway avalanching in tokamaks. The secondary generation seems to be dominant in the low density regime. During disruptions, the avalanching mechanism is also expected to play a dominant role in the runaway generation [42, 43].

2.4 Other possible primary RE sources

In most of the simulations, the Dreicer and the hot tail generation provide significant number of primary REs and other primary RE sources are negligible. In ITER, however, the tritium decay and Compton scattering of gamma-rays cannot be neglected if the Dreicer and the hot tail generation are suppressed [44]. The RE generation rate of both methods depends on the activation of the wall. The activated ITER wall can emit gamma-rays with energies of several MeV. Compton scattering of these gamma-rays with electrons can lead to runaway generation. The RE generation rate is estimated by

$$\frac{dn_r^{\gamma}}{dt} = \sigma \Gamma_r n_e, \tag{2.9}$$

where σ is the Compton scattering cross section and Γ_r the gamma-ray flux.

The efficiency of each runaway generation mechanism is mainly influenced by different parameters. The Dreicer generation is sensitive to the initial current, post-thermal quench density and post-thermal quench temperature while the hot tail generation is sensitive to $\mathcal{E}/\mathcal{E}_D$ and the cooling rate. An increase in post-thermal quench density lead to a reduction of the efficiency of both mechanisms. In JET, the hot tail generation dominates for the thermal quenches faster than 0.3 ms, otherwise the Dreicer mechanism dominates [32]. The most important parameter for the avalanche mechanism is the initial current.

3 Runaway electrons in equilibrium plasmas

This chapter is devoted to the description of RE orbits in an axisymmetric magnetic field configuration corresponding to an equilibrium toroidal plasma. For this purpose we will use the Hamiltonian formulation of relativistic guiding–center motion of charged particles proposed in Refs. [45, 46, 47]. The corresponding equations are briefly presented in Sec. 3.1. The action–angle variables are introduced in Sec.3.2. These variables are very convenient to describe particle orbits in equilibrium plasmas as well as in the presence of magnetic perturbations. The description of drift motion of REs in equilibrium plasma configuration is given in Sec. 3.3. Finally in Sec. 3.4 the outward drift motion of RE orbits induced by the toroidal electric field is presented.

3.1 Equations of guiding–center motion

We briefly describe the relativistic Hamiltonian equations of guiding–center motion of electrons. Let (R, Z, φ) be a cylindrical coordinate system. Since REs are passing particles we will use the simplified version of Hamiltonian equations reformulated by introducing the toroidal angle φ as the independent, time-like variable and the corresponding canonical toroidal momentum p_φ as a new Hamiltonian $K = -p_\varphi$. Then the canonical guiding–center variables $(q_1, q_2, p_1, p_2) = (z, t, p_z, -E)$ satisfy the Hamiltonian equations (see Refs. [45, 46, 47])

$$\frac{dq_i}{d\varphi} = \frac{\partial K}{\partial p_i}, \qquad \frac{dp_i}{d\varphi} = -\frac{\partial K}{\partial q_i}, \quad (i = 1, 2). \tag{3.1}$$

The simplified form of the Hamiltonian function is given by

$$\begin{aligned} K = -p_\varphi &= -Z_q \psi_\varphi - \sigma(R/R_0) u_\varphi, \\ u_\varphi &= \sqrt{e_0(\gamma^2 - 1) - 2\omega_R I_R}. \end{aligned} \tag{3.2}$$

The variable z and t are normalized vertical coordinate Z and time t: $z = Z/R_0$ and $t = \omega_0 \tilde{t}$, p_z is a momentum conjugated to z The relativistic factor γ in (3.2) is written in terms of the full particle energy E, i.e., $\gamma = (E - Z_q\phi)/e_0$, where $e_0 = m_e c^2/E_{ref} = (c/\omega_0 R_0)^2$ is a normalized energy of

particle at the rest, $E_{ref} = m_e R_0^2 \omega_0^2$ is the reference energy. The quantity $\psi_\varphi(R, Z, \varphi, t) = RA_\varphi / B_0 R_0^2$ is the normalized vector potential or the poloidal flux, $\phi = e\Phi / E_{ref}$ is the normalized electric field potential, I_R is the action variable conjugated to the radial gyro-phase $\vartheta_R = \omega_R T + \vartheta_{R0}$ describing the fast gyro-oscillations along the radial coordinate R, where the radial gyrofrequency ω_R is given by $\omega_R = e^{-p_z}$. The quantity $R_c = R_0(1 + e^{p_z})$ is the radial coordinate of a guiding-center.

The coordinates (R_g, Z_g) of a gyrating particle are related to the guiding center coordinates (z, p_z),

$$R_g = R + \rho_g \sin\vartheta_R, \qquad Z_g = R_0 z + \rho_g \cos\vartheta_R, \tag{3.3}$$

where $\rho_g = R_0 e^{p_z/2}\sqrt{2I_R}$ is a radial gyroradius.

The parameter σ ($\sigma = \pm 1$) determines the direction of motion with respect to the toroidal angle φ. For REs $\sigma = -1$. One should note that the field line equations can be obtained from the Hamiltonian equations (3.1), (3.2) by putting $\sigma = 0$.

The ratio of the radial gyromotion energy, $T_R = \sqrt{e_0^2 + 2\omega_R I_R} - e_0$, to the full kinetic energy of a particle, $T_K = e_0(\gamma - 1)$, i.e., $\lambda_I = T_R / T_K$, is considered as the initial parameter of motion. Experimental measurements show that for the RE the parameter λ_I may reach values 0.1, i.e., $\lambda \leq 0.1$ [4, 25].

The system of equations (3.1) for the GC motion can be presented in a form similar to the equations for the magnetic field lines in the cylindrical coordinate system (R, Z, φ). Using the definitions, $B_R = B_\varphi \partial\psi/\partial z$ and $B_Z = -(B_0/x)\partial\psi/\partial x$ for the poloidal components of the magnetic field ($B_\varphi = R_0 B_0 / R$ is the toroidal magnetic field), one can reduce the system of equations (3.1) to the form [48],

$$\begin{aligned} \frac{dZ}{d\varphi} &= \frac{RB_Z^*}{B_\varphi}, & \frac{dR}{d\varphi} &= \frac{RB_R}{B_\varphi}, \\ \frac{d\tilde{t}}{d\varphi} &= \frac{\sigma R}{v_\varphi}, & \frac{dH}{d\varphi} &= -Z_q \frac{\partial(RA_\varphi)}{\partial\tilde{t}}, \end{aligned} \tag{3.4}$$

where $v_\varphi = u_\varphi R_0 \omega_0 / \gamma_t$ is the toroidal velocity, B_Z^* is the effective poloidal field defined as

$$B_Z^* = B_Z + \frac{\sigma B_\varphi}{Z_q}\left(u_\varphi + \frac{\omega_x I_x}{u_\varphi}\right). \tag{3.5}$$

Furthermore for specific examples we will use the analytical model of the equilibrium plasma with a circular cross–section given in Appendix A.

3.2 Action–angle variables

Consider an axisymmetric tokamak configuration with the poloidal magnetic flux $\psi_\varphi(R, Z)$ and $\phi = \phi(R, Z)$. In this case the toroidal momentum p_φ

is a constant of motion and the electron orbits lie on the toroidal surface $p_\varphi(R,Z)$ =const also known as a drift surface. The drift surface does not coincide with the magnetic surface $\psi \equiv \psi_\varphi(R,Z)$ =const.

To describe such a drift motion one can introduce the action–angle variables (ϑ_z, J) associated with the canonical variables (z, p_z):

$$J = \frac{1}{2\pi}\oint_{C_z} p_z(z;E)dz, \qquad \vartheta = \frac{\partial}{\partial J}\int^z p_z(z';J,E)dz'. \tag{3.6}$$

The integrals in (3.6) ares taken along the closed contour C_z formed by the

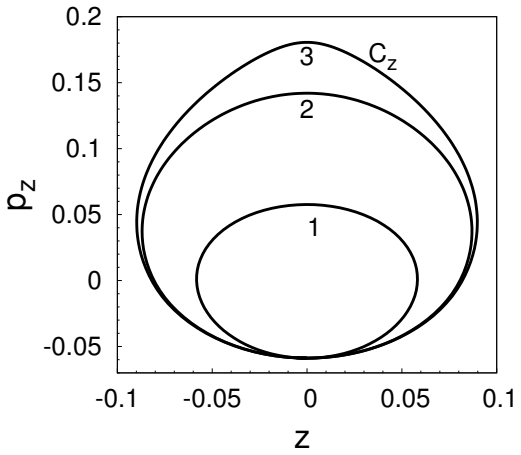

Fig. 1. Closed contours C_z of orbits in the (z, p_z) plane. Curve 1–3 correspond to RE with different energies: $1 - E = 10$ keV, $2 - E = 40$ MeV, and $3 - E = 42.5$ MeV. The plasma parameters: $B_t = 2.5$ T, $I_p = 150$ kA.

projection of the drift orbit in the $(z, p_z)-$ plane as shown in Fig. 1.

One should note that the action variable J can be used to label the drift surfaces. It is similar to the toroidal flux ψ_t which is used to label the magnetic surfaces.

One of the important parameter of the GC orbit is the effective safety factor q_p defined as a ratio $q_p = \Delta\varphi/2\pi$ where $\Delta\varphi$ is the increment of the toroidal angle φ per one poloidal turn. It is a function of the drift surface J and the particle energy W. For low–energy electrons the quantity $q_p(J,E)$ coincides with the safety factor $q(\psi)$ of the equilibrium magnetic field. With increasing the electron energy the effective safety factor strongly deviates from $q(\psi)$.

In the action–angle variables the Hamiltonian K depends on the action variable (J), $K = K_0(J,E)$. The effective safety factor is determined by $q_p(J,E) = \partial K_0/\partial J$ while the transition time $T(J,E) = \partial K_0/\partial E$. The particle trajectories $(z(t), p_z(t), \varphi(t), p_\varphi)$ are $2\pi-$periodic functions of the angle variables $\vartheta, \vartheta_\varphi$:

$$z(\vartheta, J, E) = z(\vartheta_z + 2\pi, J, E), \qquad p_z(\vartheta, J, E) = p_z(\vartheta_z + 2\pi, J, E). \tag{3.7}$$

The angle variable ϑ and time t are the linear functions of φ,

$$\vartheta = \varphi/q_p(J,E) + \vartheta_{z0}, \qquad t = T(J,E)\varphi + t_0. \tag{3.8}$$

3.3 Runaway electron orbits

In this section we discuss essential features of RE orbits in equilibrium plasmas with the different values of plasma current I_p: (i) with the values of I_p, ($\sim$ 300 kA), corresponding to the typical steady–state operation of the TEXTOR, and (ii) the small values of I_p, ($\sim 100 \div 200$ kA) corresponding to the post–disruption plasma with the RE beams.

As seen from Eq. (3.4) for low–energy electrons with the relativistic factor $\gamma \gtrapprox 1$ and the velocity $v_\varphi \ll c$ the quantity $u_\varphi = v_\varphi\gamma/(R_0\omega_0)$ is negligible compared to B_z/B_φ, $u_\varphi \ll B_z/B_\varphi$. For these electrons the effective poloidal magnetic field $B_Z^* \approx B_Z$ and electron orbits coincide with magnetic field lines. From (3.2) it follows that the drift surfaces coincide with the magnetic surfaces $\psi_\varphi(R,Z)$ =const, i.e., $p_\varphi(R,Z) \approx \psi_\varphi(R,Z)$ =const.

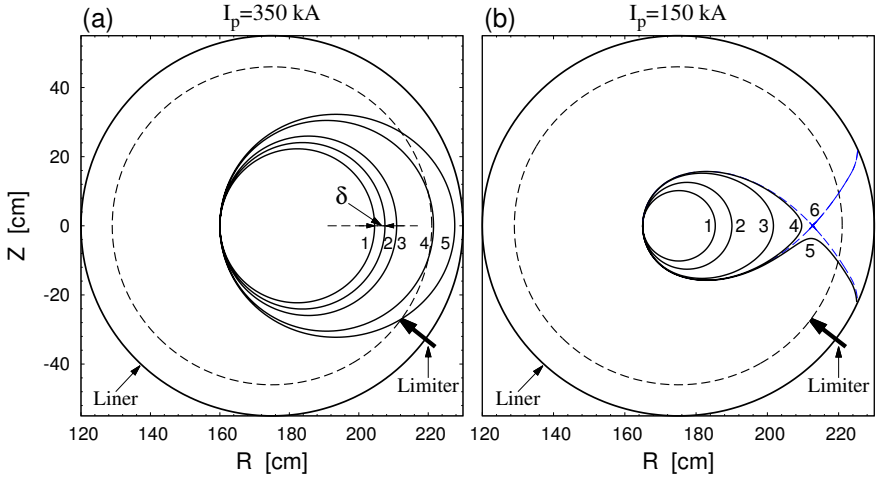

Fig. 2. **(a)** Guiding-center orbits of electrons corresponding to the different energies in the plasma with the plasma current $I_P = 350$ kA and the toroidal field $B_t = 2.5$ T: curves 1−5 correspond to energies $E = 10$ keV, 10 MeV, 20 MeV, 40 MeV, and 46 MeV, respectively; **(b)** the same as in (a) but for the plasma current $I_p = 150$ kA: curves 1−5 correspond to energies $E = 10$ keV, 20 MeV, 40 MeV, 42.5 MeV, and 42.7 MeV, respectively. Curve 8 corresponds to the separatrix with the energy $E_s = 42.646$ MeV.

For high–energy electrons with $\gamma \gg 1$ the velocity $v_\varphi \approx c$ the quantity u_φ becomes non–negligible compared to B_z/B_φ. Then the drift surfaces

$p_\varphi(R,Z)$ =const do not coincide with magnetic ones $\psi_\varphi(R,Z)$ =const. Figures 2 (a) and (b) illustrate the poloidal projections of drift orbits corresponding to the different energies having a common intersecting point at the high–field side. Curve 1 corresponds to the electron energy of 10 keV which coincides with the magnetic surface. The shape of electron orbits changes with increase of energy. At high plasma current I_p shown in Fig. 2 (a) the shape of orbits remains close to circular one. However the radius of orbits grows with increase of electron energy. At certain energy the radius becomes sufficiently large that the electron hits the limiter or the wall (a liner) as shown by curve 5.

With an increase the electron energy the corresponding drift surfaces deviate from the magnetic surface shifting outwards. The radial shift δ of the outermost point R_o of the electron orbit from the magnetic one can be obtained from (3.2) (see Fig. 2 (a)). For the small shift, $\delta \ll a$, and the small radial oscillation energy, $2\omega_R I_R \ll e_0(\gamma^2-1)$, one can obtain

$$\delta \approx \frac{(R_o - R_i)E}{ecR_0B_z} = 2\frac{\widetilde{q}E}{ecB_0}, \tag{3.9}$$

where $\widetilde{q} = rB_0/R_0B_z$, $(r = (R_o - R_i)/2)$, reminds the safety factor in a cylindrical geometry, where R_o and R_i are the outermost and innermost points of electron orbit.

At low plasma current I_p with increasing the electron energy the shape of orbits evolves as shown in Fig. 2 (b): initial circular orbits become oval ones. At the certain value of energy E_s the orbit bifurcates creating the X-point and the associated separatrix inside the plasma region as shown by curve 9. The value of E_s depends on the plasma parameters, particularly, on the plasma current I_p. Electrons with higher energies $E > E_s$ and located outside the separatrix region are no longer confined. They escape the plasma region.

As seen from Fig. 2 (b) the confined orbits (curves 1–4) are located inside the separatrix (curve 6), i.e. the boundary separating the confined and the loss orbit (curve 5). The area S_{conf} of confined orbits depends on the electron energy E and the plasma current I_p. At the given current the confined particle's area shrinks with increasing energy E. This tendency is shown in Fig. 3 (a), where the separatrices of the guiding center orbits are plotted for the four different values of the electron energies: curves 1-4 correspond to the energies 1, 10, 20, and 40 MeV, respectively.

The particles with the energy E exceeding the critical value E_{cr} are not confined in the plasma. The value E_{cr} depends on the plasma current I_p. The numerical calculations show that E_{cr} grows quadratically with I_p. The dependence of E_{cr} on the square root of the current I_p is plotted in Fig. 3 (b). This dependence can be fitted by the linear function (solid curve) $E_{cr} = a + bI_p^{1/2}$ with the constant coefficients a and b. Such a dependence is an agreement with the qualitative theoretical estimation given in Ref. [49].

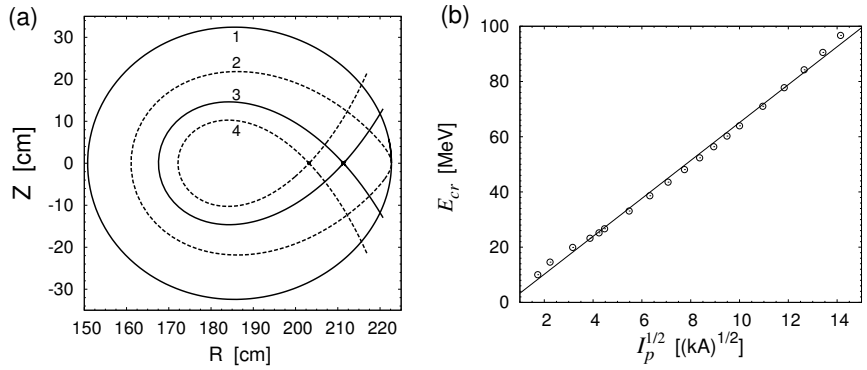

Fig. 3. **(a)** Separatrices of runaway electron orbits for the four values of the electron energies: curves 1-4 correspond to $E = 1$, 10, 20,and 40 MeV, respectively. **(b)** Critical energy E_{cr} versus the plasma current I_p: The symbols $\odot$ correspond to the numerical calculations, the solid line corresponds to the fitting by the straight line $E_{cr} = a + bI_p^{1/2}$ ($a = -2.1285, b = 6.88258$).

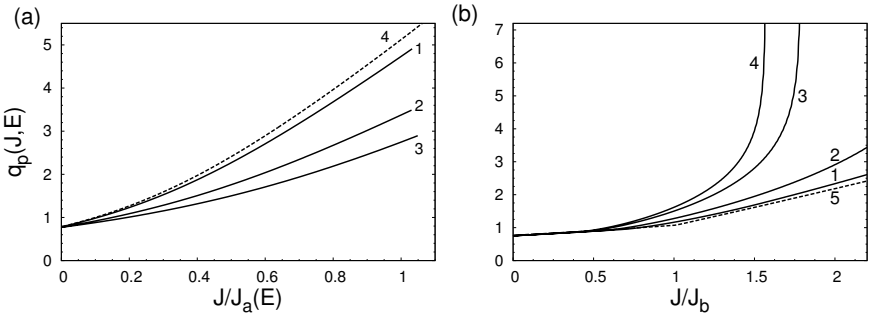

Fig. 4. Effective safety factors, $q_p(J, E)$, of REs with different energies and two different plasma currents. **(a)** $I_p = 300$ kA: The curves 1 – 3 correspond to $E_k = 1$ MeV, 10 MeV, and 20 MeV. Curve 4 corresponds to the magnetic field. **(b)** $I_p = 200$ kA with the profile $I_{RE}(\rho)$ given by (A.8): curves 1–4 correspond to $E_k = 20$ MeV, 30 MeV, 40 MeV, and 43 MeV, curve 5 − to magnetic field. The parameter $\lambda_I = 0.1$.

One should note the dependence of the effective safety factor q_p on the particle energy. For low–energy electrons q_p coincides with the safety factor $q(\psi)$ of the equilibrium magnetic field. With increasing the electron energy the effective safety factor strongly deviates from $q(\psi)$. Figure 4 shows the radial profiles of the effective safety factors $q_p(J, E)$ along the action variable J for REs with several energies in plasmas with two current $I_p = 300$ kA (a) and $I_p = 200$ kA (b): in (a) $J_a(E)$ is the value of J corresponding the last confined RE orbit at the plasma edge $r = a$, curves 1, 2, and 3 correspond to the electron energies $E_k = 1$ MeV, 10 MeV, and 20 MeV, respectively, and curve 4 corresponds to the safety factor $q(\psi)$ of the equilibrium magnetic

field. [The quantity $J_a(E)$ depends on RE energy, and $J_a \equiv J_a(0)$ is equal to the toroidal magnetic flux ψ_t through the last magnetic surface. In plasmas with the circular cross–sections of radius a one has $J_a = 1 - \sqrt{1 - a^2/R_0^2}$ (see, e.g., [47]).] In (b) $J_b = 1 - \sqrt{1 - b^2/R_0^2}$ is the value of the toroidal flux through the last magnetic surface of radius b (see (A.8) and Fig. 53); curves 1–4 correspond to $E_k = 20$ MeV, 30 MeV, 40 MeV, and 43 MeV, respectively, curve 5 corresponds to $q(\psi)$.

One should note that for high–energy REs confined by the separatrix as shown in Fig. 3 (a) the transit time $T(J, E)$ as well as $q_p(J, E)$ diverge near the separatrix as

$$T(J, E) \propto \ln \frac{B}{|p_\varphi - p_s|}, \qquad q_p(J, E) \propto \ln \frac{C}{|p_\varphi - p_s|}, \tag{3.10}$$

where p_s is the value of the toroidal momentum p_φ at the X-point, and B and C are constant coefficients (see, e.g., [47]). Such a divergence of $q_p(J, E)$ is shown by curves 3 and 4 in Fig. 4 (b).

The coordinates (R_s, Z_s) of the X-point are determined by the hyperbolic fixed point of the equation (3.4), $dR/d\varphi = 0$, $dZ/d\varphi = 0$, i.e., by the zeroes of the effective poloidal field (3.5) [48]

$$B_z^*(R_s, Z_s) = 0, \qquad B_R(R_s, Z_s) = 0. \tag{3.11}$$

Using (3.5) and (3.11) one can obtain the critical energy of the creation of the X-point,

$$E_{cr} \approx ceR_s|B_z| = 3.0 \times 10^2 R_s|B_z|, \qquad [\mathrm{MeV}]\,, \tag{3.12}$$

where B_z is expressed in Tesla (T) and R_s is given in meter (m).

One should note that the formation of the separatrix of RE GC orbits during the acceleration process in tokamaks has been first predicted in Ref. [50]. The numerical study of this process in a realistic tokamak configuration has been carried out in Ref. [24].

3.4 Outward drift of electron orbits induced by the toroidal electric field

In the start-up of plasmas or plasma disruptions the inductive toroidal electric field $\mathcal{E}_\varphi$ is generated. This electric field can be described by the inductive poloidal flux $\psi_\varphi^{(ind)}(t) = -RA_\varphi^{(ind)}(t)/B_0R_0^2$ determined the inductive vector potential $A_\varphi^{(ind)}(t) = \int^t \mathcal{E}_\varphi(t)dt$. Electrons gain the energy due to accelerating in the toroidal electric field and their orbits continuously moves (drifts) outwardly. Such a drift of electron orbits can be quantified by the outward drift velocity v_{dr} [51, 48].

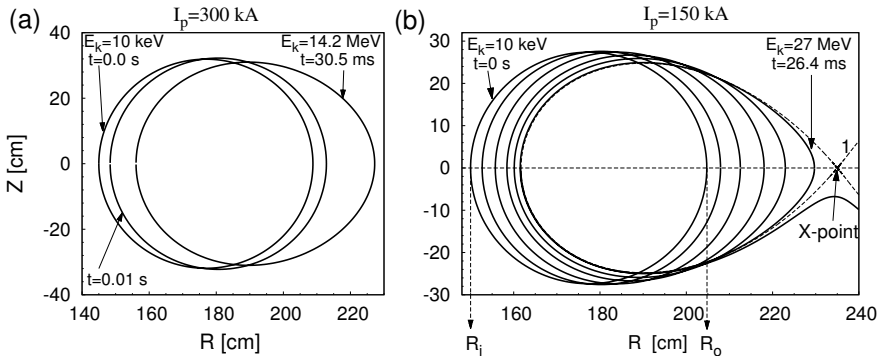

Fig. 5. Outward drift of electron orbits for the plasma current $I_p = 300$ kA **(a)** and $I_p = 150$ kA **(a)**. The toroidal magnetic field $B_t = 2.5$ T, the loop voltage $V_{loop} = 40$ V, the major radius $R_0 = 175$ cm, the minor radius a =46 cm, R_i, R_o are the innermost and outermost points of the electron orbit.

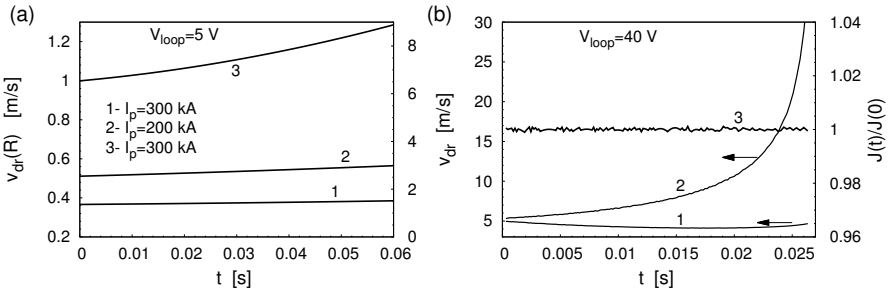

Fig. 6. **(a)** Time–evolution of the drift velocities v_{dr} of electron orbits in a toroidal electric field at the different plasma currents. The loop voltage $V_{loop} = 5$ V. **(b)** The same as in **(a)** but for the electron orbit in Fig. 5 **(b)**. Curve 1 corresponds to the innermost point R_i of electron orbit, curve 2 corresponds to the outermost point R_o of electron orbit, curve 3 corresponds to the action variable J, i.e., the normalized area encircled by an RE orbit in one poloidal turn (right hand side axis).

The drift velocity v_{dr} can be found using the fact that the toroidal momentum p_φ (3.2) is a constant of motion in the presence of a toroidal electric field. As was shown in [48] the drift velocity is given by

$$v_{dr} = \frac{R_0 \mathcal{E}_\varphi}{R B_Z^*} \left(1 - \frac{R T_{av}}{R_0 T}\right), \tag{3.13}$$

where $T_{av} = 2\pi q_p R_0 / v_\varphi$ is the average transition time, T is the transition time, v_φ is the toroidal velocity, the effective poloidal field B_Z^* is given by (3.5). The drift velocity is inverse proportional to the aspect ratio R_0/a and the plasma current I_p, ($I_p \propto B_z$): $v_{dr} \propto (a/R_0) I_p^{-1}$.

Equation (3.13) describes not only the outward drift of passing particles but also the inward drift of trapped particles known as the *Ware pinch* [52]

(see, also [53]). Indeed, for trapped particles the quantity T_{av} is much smaller than the transit time T and the expression (3.13) is reduced to

$$v_{dr} = \frac{R_0 \mathcal{E}_\varphi}{R B_Z^*} \approx \frac{R_0 \mathcal{E}_\varphi}{R B_Z}. \tag{3.14}$$

The average value of v_{dr} (3.14) over the radial coordinate R coincides the standard formula for the Ware pinch $v_p = -\mathcal{E}_\varphi / |B_Z|$.

Figures 5 (a) and (b) illustrate the time evolution of electron orbits in the toroidal electric field $\mathcal{E}_\varphi$ that is a constant in time (the toroidal electric field is determined by the loop voltage V_{loop}: $\mathcal{E}_\varphi = V_{loop}/2\pi R_0$). Figures 6 (a) and (b) show the time–evolution of the outward drift velocities at different plasma currents I_p. One should note that the acceleration of electrons in the toroidal electric field is a adiabatic dynamical process. The area in the poloidal section encircled by the GC orbit, which is proportional to the action J (3.6), is an adiabatic invariant as shown by curve 3 in Fig. 6 (b).

4 Transport of REs in a stochastic magnetic field

From the first experiments on REs generated in plasmas are observed by the hard X-ray emitted from wall of tokamaks due to their impact with high–energy electrons (see, e.g., [54]). It was commonly accepted that these events are caused by the radial transport of REs in plasmas. The estimated from measurements the radial diffusion coefficients were of order $10^{-2} \div 10^{-1}$ m^2/s. Since this could not be explained by the collisional diffusion which is of the order 10^{-4}, it is believed that the radial transport of REs is mainly caused by non–axisymmetric magnetic perturbations in tokamaks while the effect of electric field fluctuations on the high–energetic electrons of energy of order of several MeVs is usually negligible. Importantly that one should distinguish the RE transports caused by ambient magnetic turbulence, i.e., small–scale magnetic perturbations, and large–scale magnetic fields of the magnetohydrodynamic (MHD) modes and external magnetic perturbations. In the former case the radial diffusion coefficient D_r is small, i.e., in order of $10^{-2} \div 10^{-1}$ m^2/s. In the latter case the diffusion coefficient may reach values up to several 10^2 m^2/s.

Beside of magnetic perturbations the radial transport of REs can be also caused by outward drift motion of RE orbits in the presence of toroidal electric field [51, 48]. This mechanism of RE losses has been discussed above in Sec. 3.4. We consider the transport of REs caused by small–scale magnetic perturbations in Sec. 4.5. The effect of large–scale magnetic perturbations, particularly, the externally created magnetic perturbations is briefly discussed in Sec. 4.6.1. Below we present the theory of RE transport in a stochastic magnetic field.

4.1 Equations of motion in the presence of perturbations

Below we present the equations of motion in the presence of magnetic perturbations taking into account gyro–oscillations of electron orbits. In the action–angle variables (J, ϑ) (3.6) the equations of motion (3.1) have the following form,

$$\frac{d\vartheta}{d\varphi} = \frac{\partial K}{\partial J}, \qquad \frac{dJ}{d\varphi} = -\frac{\partial K}{\partial \vartheta},$$
$$\frac{dt}{d\varphi} = \frac{\partial K}{\partial E}, \qquad \frac{dE}{d\varphi} = -\frac{\partial K}{\partial t}, \tag{4.1}$$

where the Hamiltonian K (3.2) is given by

$$K = K_0(J,E) + \epsilon K_1(\vartheta, J, E, \varphi),$$
$$K_0(J,E) = \int \left[q_p(J,E)\right]^{-1} dJ. \tag{4.2}$$

The unperturbed Hamiltonian $K_0(J,E)$ corresponds to the equilibrium configuration of the plasmas. The perturbation Hamiltonian K_1 is determined by the normalized perturbation poloidal flux,

$$\epsilon K_1(\vartheta, J, E, I_R, \vartheta_R, \varphi, t) = \psi_\varphi^{(1)}(R_g, Z_g, \varphi, t), \tag{4.3}$$

where (R_g, Z_g) are the spatial coordinates of the gyrating electron and given by (3.3). The dimensionless perturbation parameter ϵ is determined by ϵ_{mn} (B.3) or ϵ_{ded} (B.7).

Since the system is a periodic function of angular variable $(\vartheta, \varphi, \vartheta_R)$ the perturbation Hamiltonian $K_1 \equiv K_1(\vartheta, J, E, I_R, \vartheta_R, \varphi, t)$ can be presented as a Fourier series

$$K_1 = \sum_{m,n,p} K_{mnp}(J,E,I_R) \exp\left[i\left(m\vartheta - n\varphi + p\vartheta_R + \Omega_{mn}t\right)\right], \tag{4.4}$$

with the Fourier coefficients $K_{mnp}(J,E,I_R)$ determined by integrals

$$K_{mnp} = (2\pi)^{-3} \int_0^{2\pi}\!\!\!\int\!\!\!\int \psi_\varphi^{(1)}(R_g, Z_g, \varphi, t) e^{[i(-m\vartheta + n\varphi - p\vartheta_R)]} d\vartheta d\vartheta_R d\varphi, \tag{4.5}$$

where the coordinates (R_g, Z_g) are considered as functions of angular variables ϑ, ϑ_R.

Furthermore, we consider separately the cases of the small–scale and the large–scale magnetic perturbations. The magnetic turbulence corresponds to the first case. The internal MHD modes and the applied external magnetic perturbations are considered as large–scale magnetic perturbations.

One should note that from the system of equations (4.1) for guiding–center motion one can obtain the Hamiltonian equations for magnetic field lines,

$$\frac{d\vartheta}{d\varphi} = \frac{\partial \psi}{\partial \psi_t}, \qquad \frac{d\psi_t}{d\varphi} = -\frac{\partial \psi}{\partial \vartheta}, \tag{4.6}$$

with the poloidal flux $\psi \equiv K$ is being the Hamiltonian function $\psi \equiv K$, and the toroidal flux ψ_t is being as a canonical momentum.

4.2 Resonance interactions and onset of chaotic motion

The presentation of the equations of motion in the action–angle variables (ϑ, J) allows one to describe the resonant interactions of RE orbits with perturbations. Let $J_{mn}, I_\varphi^{(mn)}$ be the value of J and I_φ (or energy E) corresponding to the isolated resonant surface (m, n). According to (4.4) the resonant drift surfaces in this case are determined by the conditions (see, e.g., [47])

$$m/q_p(J, p_t) - n + p\omega_R + s\Omega_{mn}\omega_t(J, p_t) = 0. \tag{4.7}$$

The width of resonances ΔJ in action variable J is given by through the amplitudes of K_{mnp} at the resonant drift surfaces,

$$\begin{aligned} \Delta J_{mn} &= 4\sqrt{\epsilon|K_{mnp}/\tilde{\kappa}_{mn}|}, \\ \tilde{\kappa}_{mn} &= \left.\frac{\partial\left[q_p(1 - s\Omega_{mn}\omega_t/n)\right]^{-1}}{\partial J}\right|_{J=J_{mn}}. \end{aligned} \tag{4.8}$$

The resonant condition (4.7) for the REs in the presence of low–frequency magnetic perturbations can be simplified in a more simple form. Indeed, for the typical MHD frequency $\Omega_{mn} \sim 10^5$ s^{-1} and $\omega_t = 1/(q_p\omega_z) = T/(2\pi q_p) \approx (2\pi R_0/c) \sim 10^{-7}$ s one can neglect the product $\Omega_{mn}\omega_t \sim 10^{-2} \ll 1$. In the order hand for moderately large mode numbers (m, n) one can neglect the effect of gyro-oscillations, i.e., one can set $p = 0$ (see Sec. 4.4). Then we have

$$m - nq_p(J, E) = 0, \tag{4.9}$$

which similar to the condition for resonant magnetic surfaces, but the safety factor q of magnetic surfaces is replaced by the effective safety factor $q_p(J, I_\varphi)$ of drift surfaces.

4.3 Onset of chaotic motion and the rate of diffusion

If there are several closely located resonant islands in a system determined by (4.7) and (4.8), they may overlap at the certain level of perturbation. The latter may lead the chaotic motion of particles across the drift surfaces. The structure of the stochastic zone and its extend depend on the spectrum of K_{mns} and the locations of the resonant drift surfaces J_{mn}. Below we introduce the diffusion coefficients characterizing the rate of the radial chaotic transport of particles in the stochastic zone across the drift surfaces J.

The rate of particle diffusion in the real space coordinate X normal to the drift surface can be quantified by the diffusion coefficient $D_r(J, E) = \langle(\Delta X(t))^2\rangle/2t$. Suppose that the relation between J and X is described by

the function $X = X(J, E)$. The diffusion coefficient $D_r(J, E)$ can be expressed through the diffusion coefficient $D_\varphi(J, E)$ of the action variable J,

$$D_r(J, E) = \frac{v_\varphi}{R_0} \left(\frac{dX}{dJ} \right)^2 D_\varphi(J, E), \tag{4.10}$$

where

$$D_\varphi(J, E) = \frac{\langle (J(\varphi) - \langle J(\varphi) \rangle)^2 \rangle}{2\varphi} = \frac{1}{2\varphi N} \sum_{j=1}^{N} \left(J_j(\varphi) - \langle J(\varphi) \rangle \right)^2 . \tag{4.11}$$

Here $\langle (\cdots) \langle$ stands for the averaging over a large number N, ($N \gg 1$), orbits $(\vartheta_j(t), J_j(t))$ with the uniformly distributed positions at the drift surface J at the initial time $t = 0$ (or the toroidal section $\varphi = 0$), i.e., $(\vartheta_j(0) = 2\pi j/N, J_j(0) = J)$, $j = 1, \ldots, N$. In (4.10) v_φ is the parallel velocity of particles. [For for nonrelativistic electrons $v_\varphi \approx v_{Te} = 1.33 \times 10^7 E_k^{1/2}$ m/s, where E_k is the kinetic energy in keV, for the REs with $E_k > 1$ MeV one can set $v_\varphi \approx c = 3.0 \times 10^8$ m/s, where c in the light velocity.].

In the quasilinear approximation the diffusion coefficient D_φ which can be presented in the following form (see Ref. [55, 56, 47])

$$D_\varphi = \frac{\pi \epsilon^2}{2} \sum_{m,n} m^2 \left| K_{mn} \right|^2 \delta \left(m/q_p(J) - n \right). \tag{4.12}$$

As seen from (4.12) due to the presence of $\delta-$ functions the diffusion coefficient is defined only at the resonant drift surfaces J_{mn}, $q_p(J_{mn}, E) = m/n$. Introducing the function $R_n^{(reg)}(J, E) = 2\pi q_p(J, E) K_{mn}(J, E)$ obtained by extension the discrete mode number m to the continuous one $m = n q_p(J, E)$, one reduce (4.12) to

$$D_\varphi = \frac{\epsilon^2 q_p}{8\pi} \sum_n n^2 \left| R_n^{(reg)}(J) \right|^2 . \tag{4.13}$$

This formula for D_J is defined for the arbitrary values of the action variable J.

We would like emphasize on the fact that according to Eqs. (4.8), (4.13) the resonant interaction of particle with perturbations and the chaotic transport are mainly determined by the values of the perturbation spectrum K_{mn} at the resonant drift surfaces $J = J_{mn}$, $q_p(J_{mn}, E) = m/n$. It means that these processes can be quantitatively described by the only one function $R_n^{(reg)}(J, E)$ of J instead of the entire set of K_{mn}. The function $R_n^{(reg)}(J, E)$ is a regular part of the integral $R_n(J, E)$ defined as

$$\begin{aligned} R_n(J, E) &= \int_{-\pi q_p}^{\pi q_p} \widetilde{K}_1(\vartheta(\varphi), t(\varphi)) e^{-in\varphi} d\varphi, \\ \widetilde{K}_1(\vartheta, t) &= \sum_{m,p} K_{mnp}(J, E, I_R) \exp\left[i \left(m\vartheta + p\vartheta_R + \Omega_{mn} t \right) \right], \end{aligned} \tag{4.14}$$

where the integral is taken along the unperturbed orbit of particle. The function $R_n(J,E)$ called the Poincaré integrals are introduced and studied in [57, 47].

The function $R_n(J,E)$ can be presented as a sum $R_n(J,E) = R_n^{(reg)}(J,E) + R_n^{(osc)}(J,E)$ of the regular $R_n^{(reg)}(J,E)$ and oscillatory $R_n^{(osc)}(J,E)$ parts. At the resonant surfaces $J = J_{mn}$ the regular $R_n^{(reg)}(J,E)$ coincides with $R_n(J,E)$, i.e.,$R_n^{(osc)}(J,E) = 0$. Figure 7 illustrates the function $R_n(J,E)$ and its regular part $R_n^{(reg)}(J,E)$ for RE orbits in the presence of magnetic perturbations created by the DED coils (see Sec. B and Eq. (B.6)).

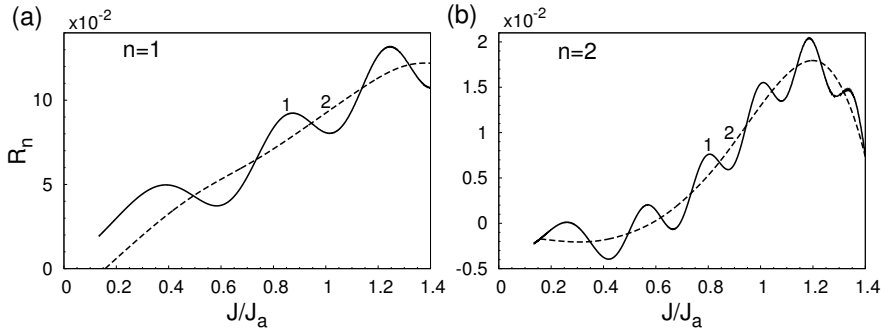

Fig. 7. Radial profiles of the function $R_n(J,E)$ (curve 1) and its regular part $R_n^{(reg)}(J,E)$ (curve 2) along the action variable J for the two toroidal modes of the DED magnetic perturbation: **(a)** $n = 1$ and **(b)** $n = 2$. The RE energy $E = 10$ MeV.

4.4 Asymptotic behavior of spectrum amplitudes K_{mnp}

The turbulent magnetic field can be presented a sum of large number $(m,n)-$modes with random phases. Similar to (B.2) the perturbation poloidal flux of this field can be written as

$$\psi_\varphi^{(1)}(R,Z,\varphi,t) = \epsilon \sum_{mn} U_{mn}(\psi)\cos(m\vartheta_M)\cos(n\varphi + \chi_{mn}(t)), \qquad (4.15)$$

where ϵ is the dimensionless amplitude of the turbulent magnetic field, the function $U_{mn}(\psi)$ describes the radial dependence of the $(m,n)-$mode. It is localized near the rational drift surface ψ_{mn}, $q(\psi_{mn}) = m/n$.

The phases $\chi_{mn}(t)$ are supposed random functions of time t with a correlation time τ_c, i.e., the correlation function $\langle \exp(i(\chi_{mn}(t+\tau_c) - \chi_{mn'}(t)\rangle = \delta_{nn'}\exp(-\tau/\tau_c)$. The typical value of the correlation time is of the order $\tau_c \sim 10^{-5}$ s. The latter is much larger than the characteristic transition time

$T = 2\pi R_0/q_p \sim 10^{-7}$ s of REs of energies $E \gtrsim 1$ MeV, i.e. the Kubo number $K = \tau_c/T \sim 10^2$. Such REs "feel" the turbulent magnetic field as a frozen one. In this case the radial transport is mainly caused by the resonance interactions of (m, n)-modes with RE orbits.

Substituting (4.15) into (4.5) and integrating over the gyrophase ϑ_R and φ the Fourier coefficients K_{mnp} (4.5) can be reduced to

$$K_{mnp}(J, I_R, E) = e^{i\chi_n} \frac{1}{2\pi} \sum_{m'} J_p\left(m'\delta\right) \int_0^{2\pi} U_{m'n}(\psi) e^{i(m'\vartheta_M - m\vartheta)} d\vartheta, \quad (4.16)$$

where $J_p(z)$ is the Bessel function of order p, δ is a small parameter of order of the ratio of gyroradius ρ_g to the radius of RE orbit $\rho = a\sqrt{J/J_a}$, $\delta \sim \rho_g/\rho$. For large $m \gg 1$ the integral and the sum over m' in (4.16) can estimated asymptotically. The corresponding asymptotical formula for the main coefficient $K_{mn}(J, I_R, E) \equiv K_{mnp=0}(J, I_R, E)$ is given by (see [47, 55])

$$K_{mn}(J, I_R, E) \approx e^{i\chi_n} \left(C/\gamma_1\right) J_0\left(m'\delta\right) U_{m'n}, \quad (4.17)$$

where $m' \approx m/\gamma_1$, r is a minor radius, C is a factor weakly depending on J,$C \approx 1$. The parameter γ_1, $(\gamma_1 \neq 1)$, takes into account the drift of the guiding center orbit with respect to the magnetic surface. It is given by the first derivative of the poloidal angle ϑ_M of the magnetic field line with respect to the corresponding angle ϑ of the guiding–center orbit taken on the low field side $(\vartheta = 0)$ of the torus, i.e. $\gamma_1 = d\vartheta_M/d\vartheta$ at $\vartheta = 0$. For the low–energy electrons $\gamma_1 \to 1$. The radial profiles of γ_1 for several energies of REs is shown in Fig. 8.

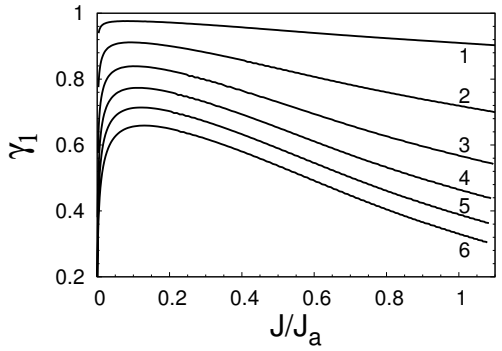

Fig. 8. Radial profiles of γ_1 for the different energies of REs: curves 1-6 correspond to $E = 1$ MeV, 5 MeV, 10 MeV, 15 MeV, 20 MeV, and 25 MeV, respectively.

From the asymptotical form (4.17) of K_{mn} follows that for the given toroidal mode n the poloidal mode m of the perturbation spectra K_{mn} is determined by the $m' \approx m/\gamma_1$ poloidal mode of the turbulent field. This effect leads to the dependence of the turbulent transport on the particle energy. This can be illustrated by the specific form of the profile of $U_{mn}(\psi) \propto$

$\exp\left[-(m-nq(\psi))^2/4w_n^2\right]$, localized near the rational magnetic surface ψ_{mn}, $q(\psi_{mn}) = m/n$. Then according to (4.17) we have

$$K_{mn}(J, I_R, E) \propto \gamma_1^{-1} \exp\left[-(m/\gamma_1 - nq(\psi))^2/4w_n^2\right]. \quad (4.18)$$

The magnitude of K_{mn} at the resonant drift surface J_{mn}, $q_p(J_{mn}) = m/n$ is not equal to the function U_{mn} at the corresponding rational magnetic surface ψ_{mn},

$$\frac{K_{mn}(J_{mn})}{U_{mn}(\psi_{mn})} \approx J_0\left(\frac{m\rho_g}{\rho}\right)\gamma_1^{-1}\exp\left[-\frac{n^2}{w_n^2}\left(\frac{q_p(J_{mn})}{\gamma_1} - q(\psi)\right)^2\right] \neq 1. \quad (4.19)$$

Typically this ratio is less than unity, thus leading to decrease the effect of the magnetic perturbation on REs with increasing their energy. This phenomenon is known as an *orbit–averaging effect*.

In Eq. (4.17) the term with the Bessel function $J_o(m\delta)$ takes into account the *gyro-averaging effect* of the turbulent field modes m, that effectively cuts off the contributions of the higher poloidal modes $m > m_c$ to the turbulent transport, where $m_c = \gamma_1/\delta$ is the critical poloidal mode number. The corresponding toroidal mode number n_c is equal to $n_c = m_c/q_p = \gamma_1/q_p\delta$.

4.5 Transport of REs due to magnetic turbulence

As was noted above for REs the Kubo number $K \gg 1$. In this case the radial transport of REs occurs due to a chaotic motion caused by the interaction of neighboring resonances between RE orbits with the $(m, n)-$modes of turbulent field. The rate of radial transport depends on the level of turbulent magnetic field ϵ and on its spectrum K_{mn}. In the quasilinear approximation the diffusion coefficient D_r is given by Eqs. (4.10), (4.13).

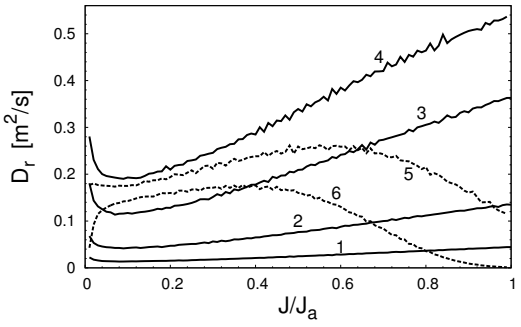

Fig. 9. Radial profiles of the diffusion coefficients D_r (4.10) for different RE energies: curve 1 corresponds to $E = 1$ keV; curve 2 – $E = 10$ keV; curve 3 – $E = 10^2$ keV; curve 4 – $E = 1$ MeV; curve 5 – $E = 10$ MeV; curve 6 – $E = 20$ keV. The turbulent level $\epsilon = \delta B/B_0 = 10^{-4}$.

Figure 9 illustrates the radial profiles of the diffusion coefficients D_r for different electron energies. The diffusion coefficients D_r change non-monotonically with the energy. Since $D_r \propto v_\parallel D_J$ the diffusion coefficient

D_r grows in the energy interval from 1 keV to 1 MeV because of the increase of the parallel velocity $v_\parallel$ with the energy E and reaches the maximal value at $E \sim 1$ MeV. If the energy is increased further D_r starts to decrease due to the decay of D_{FL} due to the screening effect, while $v_\parallel$ approaches the speed of light c.

According to the quasilinear formula (4.13) with the spectrum (4.19) the decrease of the diffusive transport with increasing electron energies occurs at small radii ρ, ($\rho = a\sqrt{J/J_a}$) due to the effect of the gyro–averaging of a turbulent field and at large radii ρ due to the orbit averaging effect. The latter is believed to be responsible for the improved confinement of REs with increasing energies.

4.5.1 Fractional diffusion

Direct numerical calculations of diffusion coefficients D_r, however, shows that the radial profiles of D_r are not smooth functions of J, but they are irregular fractal–like functions of J. Figure 10 illustrates such a fractal-like dependence of D_r on the radial coordinate J for the electron of energy 10 MeV. One can see that near the low-order rational drift surfaces J_{mn}, $q_p(J_{mn}) = m/n$, shown by vertical lines, $m/n = 1/1, 3/2, 2/1, 5/2, 3/1$, the diffusion coefficient D_r drops to lower values significantly deviating from the quasilinear values shown by curve 2. One can say that effective barriers to the radial transport are formed. The reduced radial transport near the low-order rational drift surfaces is related to the gaps in the density of the rational drift surfaces there [56].

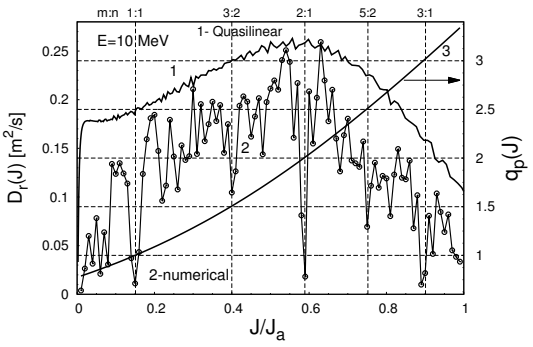

Fig. 10. Numerically calculated radial profile of the diffusion coefficient D_r (curve 1) for the RE of energy $E = 10$ MeV. Curve 2 corresponds to the quasilinear formula (4.10), (4.13) curve 3 – the effective safety factor $q_p(J)$ vs J (r.h.s axis). The positions of the rational drift surface J_{mn}, $q_p(J_{mn}) = m/n$, are shown by dashed vertical straight lines.

The described mechanism of the turbulent transport of energetic electrons can be one of the main reasons for the improved confinement of REs in tokamaks additional to the effects of the gyro–averaging and the orbit–averaging mechanisms. One can expect that this effect may lead to the formation of the nested beams of REs. The ring–like structure in the synchrotron radiation

pattern recently observed in the EAST tokamak [58, 59] is probably related to the formation of transport barriers for high–energetic REs.

4.5.2 Historical remarks

For the low–energy electrons the perturbation spectrum K_{mn} can be replaced by the spectrum of magnetic perturbations $B_{mn} = mU_{mn}$ in (B.1). Then the diffusion coefficient D_r of electrons (4.10) is expressed through the diffusion coefficient of field lines $D_{FL}(\rho)$,

$$D_r = v_{||} D_{FL},$$
$$D_{FL}(\psi) = \frac{\pi q(\psi) R_0}{2} \sum_{mn} \left| \frac{B_{mn}}{B_0} \right|^2 \delta\left(m - nq(\psi)\right). \tag{4.20}$$

This formula describes the diffusion of thermal electrons in a stochastic magnetic field in a collisionless approximation [60, 61, 62] (see also [47]). The formula (4.20) called the Rechester and Rosenbluth formula has been often applied to estimate the diffusion rate of REs in a stochastic magnetic field.

However, the estimations of D_r for REs based on this collisionless diffusion coefficient $D_r = cD_{FL}$ in a stochastic magnetic field *exceeds the measured ones from the experimental observations*. This discrepancy between the experimentally measured diffusion coefficient of REs and the ones expected from the theory of radial transport in a stochastic magnetic field has been subject numerous studies since 1980s (see, e.g., [63, 64, 65, 66, 67, 68, 69, 13, 70, 55] and references therein). Particularly, it has been suggested that due to the displacement of RE GC orbits from magnetic surface and their large gyro–radius the REs do not experience the full strength of the magnetic perturbation. These effects were taken into account by introducing the so–called *shielding factor* Υ in the diffusion coefficient D_r, i.e.,

$$D_r \simeq \Upsilon v_{\|} D_{FL}. \tag{4.21}$$

The factor Υ describes the deviation of the RE diffusion from the thermal electron diffusion due to the displacement of the RE orbits from the magnetic surfaces (*orbit–averaging*) and their large gyro-radii, i.e., *gyro–averaging*. In Ref. [70] the validity of the orbit–averaging due to the so-called *orbit decorrelation* effect and and its role in the possible decrease of the runaway diffusion has been discussed. The general asymptotical formula for D_r of REs has been derived in [55] (see also [56, 47]).

4.6 Transport of REs induced by large–scale magnetic field perturbations

Now we consider the transport of REs caused by magnetic perturbations of low–mode number MHD modes and applied external currents. This problem has been a subject of numerous studies since middle 1990s due to its

importance to control of the generation of REs and to suppress them. Particularly, the effect of the drift motion of RE orbits on their interactions with magnetic perturbations has been investigated in [67, 68, 69, 71] (see also references therein). Suppression of REs by the external magnetic perturbations to suppress REs has been intensively discussed since late 1990s (see, e.g., [72, 73, 39, 74, 75, 20, 76, 77, 78, 79, 80] and references therein). Particularly, the effect of the resonant magnetic perturbations (RMPs) on REs in the TEXTOR-DED has been theoretically and experimentally studied in [81, 46, 82, 21] in a steady–state operation, and in [20, 83, 84, 85] during plasma disruption. The suppression of disruption–generated REs by the RMPs in ITER tokamak has been explored in [78, 79]. In [86] a localized vertical magnetic perturbation applied at one toroidal location has been used to mitigate REs during plasma disruption in ADITYA tokamak. RE bursts experimentally observed during plasma disruptions in the TEXTOR tokamak are related to the interaction of MHD modes with RE orbits [87].

Below we describe the main features of the interactions of REs with external magnetic perturbations created by the DED of TEXTOR tokamak and internal MHD modes. The models of magnetic perturbations associated by the MHD modes and the TEXTOR-DED coils used to study this problem are described in Appendix B. Experimental results are described in Sec. 6.4.

4.6.1 Losses of REs caused by DED field perturbations in steady–state plasmas

Consider first the effect of the DED perturbations on RE orbits and its dependence RE energy. The DED magnetic field perturbations are designed to create stochastic magnetic field lines at the plasma edge that are open the wall. The structure of low–energy (thermal) electron orbits affected by these magnetic perturbations will be similar to the one of magnetic field lines since these electrons closely follow magnetic field lines (see Fig. 13 (c) below).

However with increasing the energy of electrons their interaction with the DED perturbation field starts to deviate from the ones of thermal electrons. The quantitative characteristics of this interactions is given by the spectra of perturbations K_{mn} or more precisely by the Poincaré integrals $R_n^{(reg)}(J,E)$ (4.14). Figure 11 (a) and (b) illustrates the radial profiles of $R_n^{(reg)}(J,E)$ of different energies of REs in the presence of the DED field perturbations with the toroidal modes $n=2$ and $n=4$, respectively. Curves 1–4 correspond to RE energies $E_k = 1$ keV, 1 MeV, 5 MeV, and 10 MeV, respectively.

As seen from Figure although the positions of resonant drift surfaces J_{mn} (shown by symbols $\odot$, $\boxdot$, $\triangle$) are slightly shifted outward, the functions $R_n^{(reg)}(J,E)$ change significantly with the increase of RE energy E_k: the group of resonances with maxima values of $R_n^{(reg)}(J,E)$ shift outward. The latter leads outward shift of the stochastic zone of RE orbits.

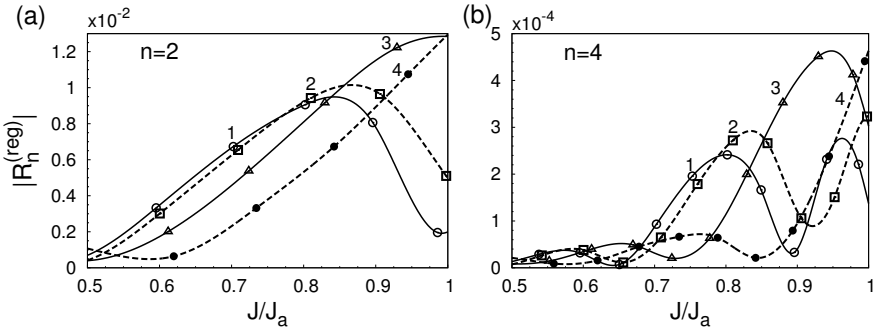

Fig. 11. Radial profiles of the functions $R_n^{(reg)}(J,E)$ for the different electron energies E_k in the presence of the DED perturbations: **(a)** the toroidal mode $n=2$; **(b)** $n=4$. Curves 1–4 correspond to RE energy: $E_k = 1$ keV, 1 MeV, 5 MeV, and 10 MeV, respectively. Symbols $\odot$, $\boxdot$, $\triangle$ correspond to the positions of resonant drift surfaces J_{mn}, $q_p(J_{mn}) = m/n$. The plasma current $I_p = 350$ kA, the toroidal field $B_t = 2.2$ T, the minor radius $a = 0.46$ m, the major radius $R_0 = 1.75$ m.

The typical Poincaré sections of RE orbits in the $(R,Z)-$plane of the section $\varphi = 0$ are shown in Figs. 12 for the two different energies and the DED field perturbations with the two toroidal modes n: (a) $E_k = 10$ MeV, $n = 1$; (b) $E_k = 20$ MeV, $n = 1$; (c) $E_k = 10$ MeV, $n = 2$; (b) $E_k = 20$ MeV, $n = 2$. The Poincaré sections of RE orbits in the $(\theta, r)-$ and $(\vartheta, J)-$ planes are shown in Figures 13 (a), (b), (c); and (d) for the DED perturbation mode $n = 2$ and two RE energies: (a), (c) $E_k = 1$ keV and (b), (d) $E_k = 10$ MeV, respectively. They are similar the typical structure of magnetic field lines created by the DED perturbation field at the plasma edge (see, e.g., [47]). Other examples of Poincaré sections of RE orbits are given in Sec. 6.4 (Fig. 26) where the experimental results of the RE transport in the DED field perturbations are discussed.

The stochastic zone is open to the wall and orbits except those trapped in the stability islands leave it by hitting the wall. The orbits near the inner boundary of the stochastic zone stay longer than those close to the wall. The latter leave the stochastic layer along stripes in a few poloidal turns. This zone of the stochastic layer is known as *a laminar zone*. As seen from Figs. 12 and 13 (a), (b) the stochastic zone of RE orbits shifts outward with the increase of electron energy. The inner boundary of the stochastic zone shifts outward with increase RE energy and the stochastic layer shrinks. The stochastic layer also becomes thinner in the case of DED field with higher toroidal mode $n = 4$. *These two effects make inefficient to mitigate high–energy REs in plasma by applying the RMPs with higher toroidal modes* n.

Figure 13 (e) and (f) show the dependences of $R_n^{(reg)}(J,E)$ (curves 1), the width of resonances ΔJ_{mn} (segments 2), the quasilinear diffusion coefficients $D_r(J,E)$ (4.10), (4.13) (curves 3), and the numerically calculated diffusion

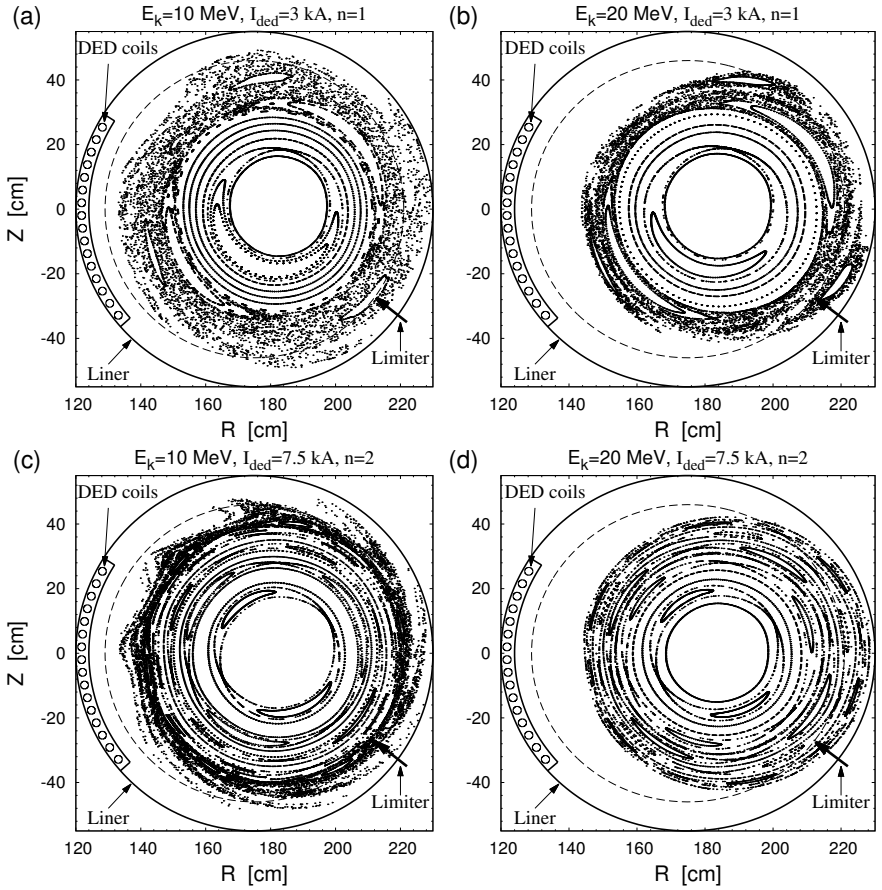

Fig. 12. Poincaré sections of guiding–center orbits of REs in the $(R, Z)-$plane of the section $\varphi = 0$. The parameters are the same as in Fig. 11.

coefficients (shown by symbols $\odot$), corresponding to these stochastic orbits of REs shown in (a)–(d).

The transport rate of REs in the innermost zone of the stochastic layer can be satisfactorily described by the quasilinear diffusion coefficient $D_r(J, E)$ (4.10), (4.13). As seen from Fig. 13 (e) and (f) the latter (solid curve 3) closely follow the numerically calculated diffusion coefficients (symbols $\odot$). However, in the laminar zone the numerical diffusion coefficients strongly deviate from the quasilinear formula. Actually, in this zone the description of transport of REs as well as field lines as a diffusion process fails (see, e.g., [47]).

One can estimate the characteristic escape time τ_{esc} of REs from the stochastic layer. In the inner stochastic layer it is determined by the diffusion time $\tau_D = \delta^2/2D_r$, where δ is the width of the stochastic layer. The latter is of order of 0.1 m. Then for the RE with the energy $E_k = 10$ MeV and

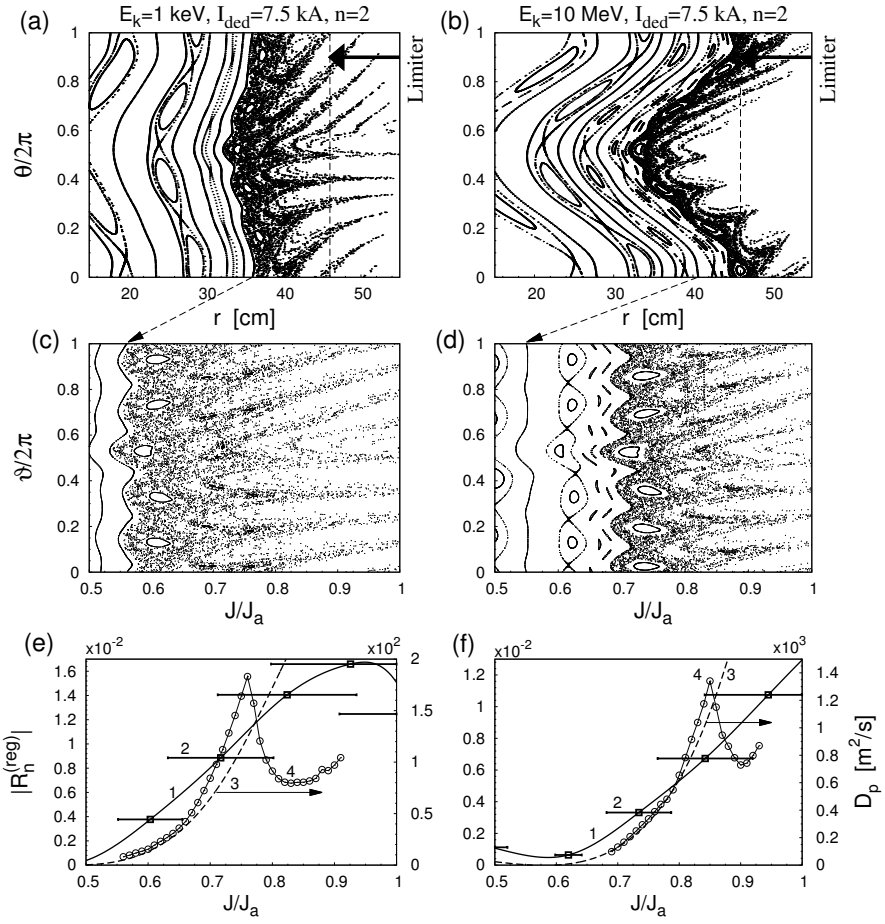

Fig. 13. **(a)** and **(b)**: Poincaré sections of guiding–center orbits of REs in the $(\theta, r)-$plane of the section $\varphi = 0$; **(c)** and **(d)**: The same but in the $(\vartheta, J)-$plane; **(e)** and **(f)**: Radial profiles of the functions $R_n^{(reg)}(J, E)$ (red curves 1), the width of resonances ΔJ_{mn} (4.8) (green horizontal segments 2), and the quasilinear diffusion coefficients $D_r(J, E)$ (4.10), (4.13) (curves 3 on the right–hand axis), and symbols $\odot$ correspond to the numerically obtained diffusion coefficients. In **(a)**, **(c)**, and **(e)**: RE energy $E_k = 1$ keV; in **(b)**, **(d)**, and **(f)** $E = 10$ MeV. The toroidal mode of the DED perturbation $n = 2$. The other parameters are the same as in Fig. 11. The DED current $I_{ded} = 7.5$ kA.

$D_r = (0.2 \div 1) \times 10^3$ m^2/s (see Fig. 13 (f)) we have $\tau_D \approx (2.5 \div 0.5) \times 10^{-5}$ s. For electrons with $E_k = 1$ keV and D_r in Fig. 13 (a) the time τ_D is in order of 10^{-4} s $=10^2 \mu$s [1].

The escape time of REs from the laminar zone can be determined as $\tau_{esc} = N l_c / v_\varphi$, where N is the number poloidal turns before hitting the wall, $l_c = 2\pi R_0 q_p$ is the connection length. For the typical value of $N \lesssim 10$ we have $\tau_{esc} \approx 10^{-6}$ s $= 1\mu$s.

4.6.2 Effect of MHD mode and DED field perturbations on REs in post–disruption plasmas

As we have discussed in Sec. 3.3 for the small values of the plasma current I_p corresponding to the post–disruption plasma with REs the shape of their orbits evolves from circular one to the oval one with increasing electron energy. The REs loose confinement at the certain value of energy E exceeding the certain energy E_s by crossing the separatrix as shown in Fig. 2 (b). The magnetic perturbations of MHD modes and external coils may also cause the loss of REs due to their resonance interactions with RE orbits. Below we discuss main features of this interaction.

The interaction of REs with magnetic perturbations and the onset of chaotic motion depends on the locations J_{mn} of resonances (4.9), their widths ΔJ_{mn} (4.8). Typically the post–disruption plasma which leads the formation of REs has the safety factor profile $q(J)$ with the value $q_b(J_b)$ less than nearest low–order rational number 5/4 (or 4/3, ...) (see curve 5 in Fig. 4 (b) and Sec. 8.1). Therefore in the plasma region $J \le J_b$ there is only one low–order rational magnetic surface $q = m/n$, namely, $q = 1$. In such a plasma the magnetic perturbations containing the low–order (m, n) harmonics K_{mn} do not cause the loss of low–energy REs. This is because of that the drift surfaces of low–energy REs are close to magnetic surfaces and the one $(m = 1, n = 1)$ resonance do not produce the stochastic zone open to the wall.

However, for the high–energy REs the effective safety factor $q_p(J, E)$ take higher values and the number of possible resonances (4.9) grows as was shown in Fig. 4 (b). It leads also to the growth of the higher order harmonics K_{mn} of the perturbations.

To be specific consider the effect of the $(m = 1, n = 1)$ MHD mode on REs of different energies. Figures 14 (a) and (b) show REs orbits in the $(R, Z)-$plane for several RE energies E_k and the corresponding them the spectra of perturbations K_{mn}. The orbits are chosen to have a common point at the low–field side of the torus. As seen from (b) the amplitudes K_{mn} of

[1] One should note that these estimates are applicable only to the transport of REs, but not the transport of thermal electrons in plasma. In the latter case D_r describes the electron heat diffusion but not a particle diffusion. The diffusion of thermal particles in the stochastic magnetic field has an ambipolar nature and has much lower rate.

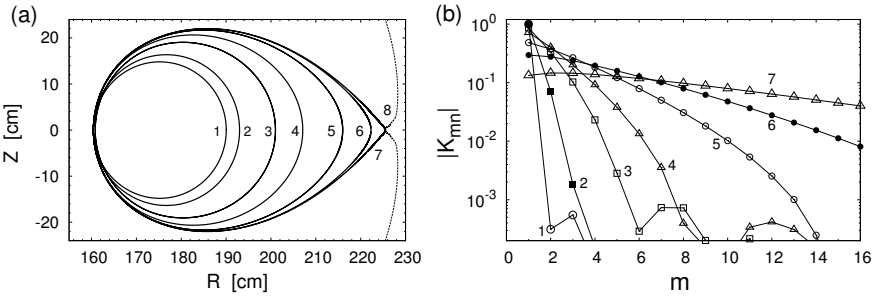

Fig. 14. **(a)** RE orbits in the (R, Z)-plane and **(b)** corresponding spectrum of perturbations K_{mn} in the presence of the magnetic perturbations of the $(m = 1, n = 1)$ MHD mode. Curves 1–7 correspond to RE energy: $E = 1$ keV, 10 MeV, 30 MeV, 35 MeV, 39 MeV, 39.9 MeV, and 40 MeV, curve 8 corresponds to the separatrix. The plasma current profile $I_{RE}(\rho)$ is given by (A.8) and curve 2 in Fig. 53 with $I_{RE}^{(0)} = 200$ kA, the toroidal field $B_t = 2.2$ T, the minor radius $b = 0.185$ m, the major radius $R_0 = 1.75$ m.

the higher mode harmonics $m > 1$ grow with increasing the RE energy. For the spectrum K_{mn} corresponding to the RE orbits close to the separatrix one can obtain the following asymptotical formula (see, [47]),

$$K_{mn} \approx \frac{A(J)}{q_p(J,E)} \exp\left(-\frac{mC(J)}{q_p(J,E)}\right), \tag{4.22}$$

where $A(J)$ and $C(J)$ are smooth functions of J with finite values $A(J_s) \neq 0$ and $C(J_s) \neq 0$ at the separatrix J_s, where $q_p(J,E)$ has a logarithmic singularity (3.10).

On the other hand the rational drift surfaces J_{mn}, $q_p(J_{mn}, E) = m/n$, in the plasma region become dense which leads to overlapping of the corresponding resonances and the formation of stochastic zone open to the wall. Figure 15 illustrates the described mechanism of the effect of the $(m = 1, n = 1)-$ MHD mode on the low–energy electron of energy $E_k = 1$ keV and the high–energy RE of $E_k = 40$ MeV, respectively: (a) and (b) shows the effective safety factor profiles $q_p(J,E)$ (curve 1) and the widths of resonances ΔJ_{mn} (horizontal segments 2). The Poincaré sections of RE orbits in the $(\vartheta, J)-$plane are plotted in Fig. 15 (c) and (d).

The effect REs of the $n = 1$ operational mode of the DED magnetic perturbations on REs is similar to that of the $(m = 1, n = 1)-$ MHD mode. The examples of the structure of REs affected of the TEXTOR–DED are shown in Figs. 16 (a) and (b) where the Poincaré sections of RE orbits in the $(R, Z)-$plane are plotted for the two different RE energies: $E_k = 10$ MeV (a) and $E_k = 30$ MeV, respectively. REs of 10 MeV energy interact with the $(m = 1, n = 1)$ magnetic perturbations forming a number of high–order isolated resonances shown in Fig. 16 (a). For the high–energy REs the region

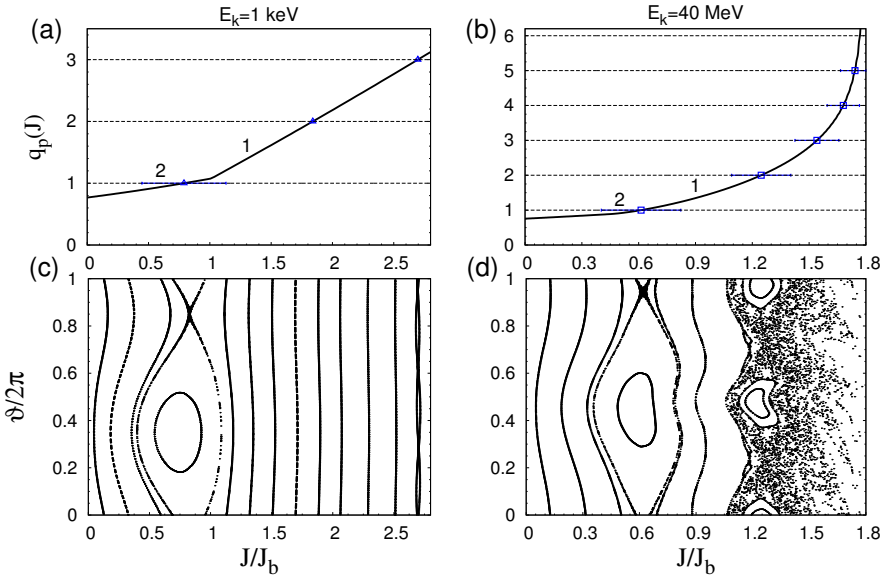

Fig. 15. **(a)** and **(b)**: Effective safety profiles $q_p(J, E)$ (curves 1) and the width resonances (horizontal segments 2) for REs with energies $E = 1$ keV and 40 MeV. **(c)** and **(d)** Poincaré sections of the RE guiding center orbits in the $(\vartheta, J)-$plane corresponding to **(a)** and **(b)**, respectively. The other parameters are the same as in Fig. 14.

of confined REs shrinks and the interaction of resonances near the near the separatrix (blue curve) forms a stochastic zone open to the wall as shown in Fig. 16 (b).

The characteristic escape time τ_{esc} of REs from the stochastic zone can be estimated similar to one made above in the previous subsection. It has the order of several microseconds.

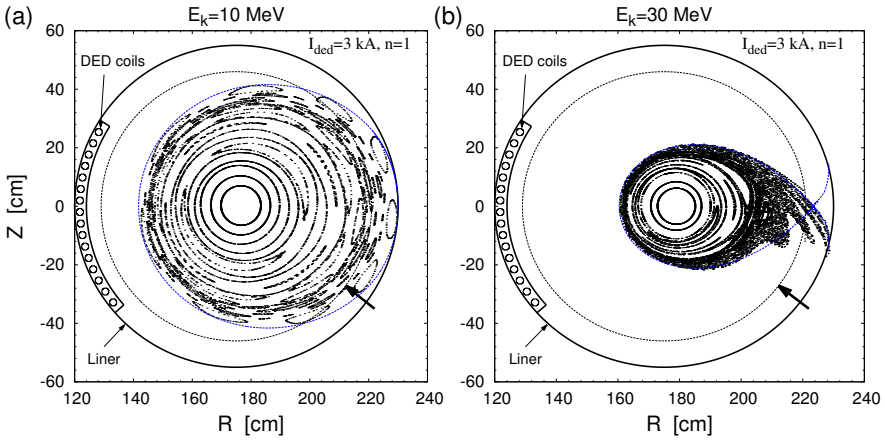

Fig. 16. Poincaré section of the RE guiding center orbits in the $(R, Z)-$plane in the DED perturbation field. **(a)** RE energy $E_k = 10$ MeV; **(b)** $E_k = 30$ MeV. The RE current is $I_{RE}^{(0)} = 150$ kA, the toroidal mode $n = 1$, the DED current $I_{ded} = 3$ kA. The blue curves correspond to the separatrix.

5 Diagnostic techniques of runaway electrons

The techniques used to diagnose REs can be classified as direct and indirect measurements. The direct methods use properties of the runaways during their flight while the indirect ones mainly use the runaway-wall interactions of the lost runaways.

In early experiments, such as in the Princeton Model C-Stellarator [88, 89], ORMAK [90], T-6 [91], ATC [92], TFR [93], Alcator [94] and others, runaway beams have been detected by the emission of hard X-rays, γ-ray and neutrons which have been created when the runaways hit the vessel components of the devices (see a review [49]). In addition an enhanced microwave radiation, synchrotron radiation and spiky losses in the magnetic flux have been observed. Dramatic damages have been discovered in TFR and Alcator from runaways trapped in non-axisymmetric magnetic ripples.

Synchrotron radiation, in particular its 2-D recording by an IR camera, is a direct observation and allows the observation of the confined REs, i.e. their location in the discharge, their growth and their loss. Additionally, special probes have been developed at the Düsseldorf University to measure REs at different positions including a scintillator probe [95, 96, 97], a heat load probe [98] and a calorimeter probe [99] (see [100] for more details). In this context, we describe only those diagnostics which are here of particular interest, namely the synchrotron radiation and the different probes.

5.1 Synchrotron radiation

In magnetically confined plasmas, electrons gyrate around the magnetic field lines and emit the radiation at the cyclotron frequency $\omega_{c,e}$ and its harmonics perpendicular to the direction of acceleration. The frequency of the radiation is typically in the microwave range. With higher electron energies, more and more harmonics are generated which finally leads to the continuum synchrotron radiation in the relativistic limit. In contrast to the cyclotron emission, the synchrotron radiation is forward in the direction of the instantaneous flight with an opening angle $\theta \approx 1/\gamma$. In fusion devices, the observed emission angle is considerably larger because the electron gyrate in a helix around the magnetic field lines such that the velocity vector covers the area with the pitch angle $\Theta = v_\perp / v_\parallel$ where $v_\perp$ and $v_\parallel$ are the perpendicular and

parallel velocity components of the runaways with respect to the magnetic field lines, respectively. The spectral density of the synchrotron emission from a single electron is given by [1]

$$\frac{dP(\lambda)}{d\lambda} = \frac{2\pi e^2 R_c}{\sqrt{3}\epsilon_0 \gamma^2 \lambda^3} \int_{\lambda_c/\lambda}^{\infty} K_{5/3}(\xi) d\xi, \tag{5.1}$$

where $K_p(\xi)$ is the modified Bessel function of the order p and $\lambda_c = 2\pi c/\omega_c = 4\pi R_c/3\gamma^3$ is a critical wavelength, R_c is the instantaneous time–dependent radius of curvature of the RE orbit. Figure 17 (a) shows the wavelength distribution of the normalized spectral density $AdP/d\lambda$, $(A = \varepsilon_0 \lambda_c^3/\sqrt{3}e^2\gamma)$. At the limiting cases $\lambda \ll \lambda_c$ and $\lambda \gg \lambda_c$, the spectral density has the

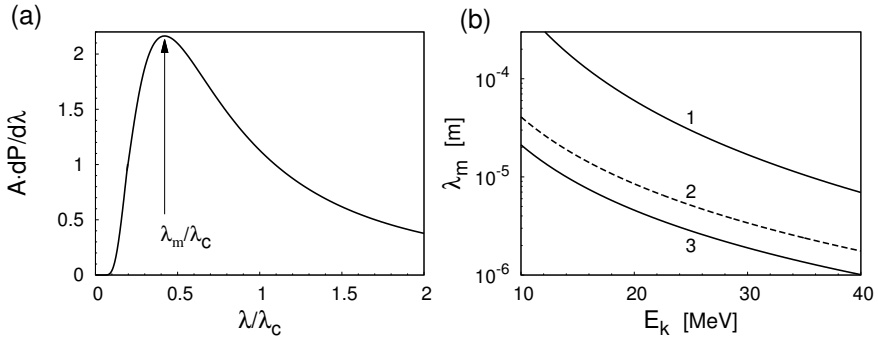

Fig. 17. **(a)** Normalized spectral density of synchrotron radiation $dP/d\lambda$. The normalization constant $A = \varepsilon_0 \lambda_c^3/\sqrt{3}e^2\gamma$. **(b)** the maximum wavelength $\lambda_m = 0.421\lambda_c$ as a function of electron kinetic energy E_k for the different pitch angles $\Theta = v_\perp/v_\parallel$: curve 1 − $\Theta = 0$, curve 2 − $\Theta = 0.1$, curve 3 − $\Theta = 0.2$.

following asymptotical behavior,

$$\frac{dP(\lambda)}{d\lambda} \approx \frac{e^2}{2\varepsilon_0} \begin{cases} (2\pi R_c)^{1/3} \lambda^{-7/3}, & \text{if } \lambda \gg \lambda_c, \\ \sqrt{\dfrac{3\pi\lambda_c}{2}} \gamma \lambda^{-5/2} e^{-\lambda_c/\lambda}, & \text{if } \lambda \ll \lambda_c. \end{cases} \tag{5.2}$$

As seen from (5.2) towards shorter wavelengths $\lambda \gg \lambda_c$, the synchrotron radiation drops exponentially. The characteristic wavelength $\lambda_c = 4\pi R_c/3\gamma^3$ depends on the electron energy $E = m_e c^2 \gamma$ and the radius of curvature R_c of orbit. The maximum of the spectrum reaches at the wavelength $\lambda_m \approx 0.421\lambda_c$. The dependences of λ_m on the electron energy E_k at the different

[1] The formula for the spectral density of the synchrotron radiation has been derived in 1940s in [101, 102].

pitch angles Θ are shown in Fig. 17 (b) where we have used the average value of R_c approximated through the pitch angle Θ and γ: $1/R_c = (1-\Theta^2)/R_0 + \omega_0\Theta/c\gamma$ (see [25]).

One should note that the above formula (5.1) for the spectral density of the synchrotron radiation is obtained for a circular orbit of electrons. The corresponding formula for the electron orbits in a tokamak magnetic field has been derived in [103].

In medium size tokamaks such as TEXTOR [42] and HT-7 [104], the synchrotron radiation is limited to the IR wavelength range. Particularly, in the TEXTOR tokamak the synchrotron radiation is observed in the wavelength range between 3 and 6 μm. The observation of synchrotron radiations in the visible range has been reported in EAST [105] and DIII-D [106]. The synchrotron radiation enables the observation of the runaway structure and dynamics [24]. The pitch angle and the absolute number of REs are deduced from the 2D image of the runaway beam recorded by an IR camera and its energy from the spectrum, e.g. by applying different filters on front of the camera. For visible synchrotron radiation, it is possible to obtain the spectral information of the REs during a disruption because each pixel of the visible camera contains RGB (red green blue) color data. By comparing the signals of different color channels, one gets the radiated spectrum. The principles of the synchrotron radiation and experimental results are presented in references [4, 107, 26, 108].

5.2 Scintillator probes

The scanning probes were developed at Heinrich-Heine University Düsseldorf in order to study REs in the TEXTOR tokamak [95, 109, 96]. Their active part consists of a set of scintillating YSO crystals; an advantage of the YSO crystal is that the energy absorbed by the crystal is a slowly varying function of an incident energy for γ-ray with energy higher than 100 keV [110]. For an electron in the same energy range, the absorbed energy is also expected to change slowly with the energy of the electron. The characteristics of the YSO crystal are shown in table 1. The crystal is sensitive not only to electrons but also to γ-rays. However, the signal produced by electrons is twice as high as the signal generated by γ-rays.

Characteristics of the YSO crystal	
light output	30000 photons/MeV
melting point	2470°C
decay time	42 ns
peak emission	420 nm

Table 1. Characteristics of the YSO crystal [111].

The probes were placed at the equatorial midplane of TEXTOR at the low field side. They provide a direct measurement of the REs near the plasma boundary. The measured energy range of the probes is analyzed by using the Monte Carlo GEANT4 simulation code [112, 113]. GEANT4 code was designed and developed by an international collaboration between physicists and software engineers from cooperating institutes and universities. The source code, the installation and user guide as well as the training kits are freely available online [114]. User can arbitrarily define the materials and shapes of the geometrical models or use a library of shapes, materials and elements contained in the toolkit. The test particles can also be chosen from the GEANT4 library. The code contains a set of physics models used to describe the interaction between test particles and matter. Tracks of test particles and the detector response as well as the creation of the daughter particles can be achieved. For the study on REs the GEANT4 code was used for the probe design and calibration.

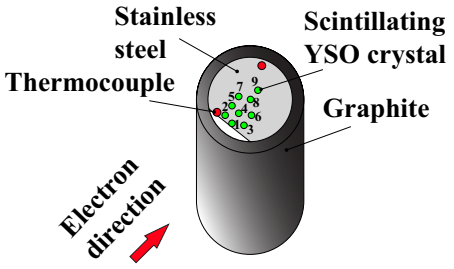

Fig. 18. Schematic of the final scintillator probe. The probe consists of 9 YSO crystals and 2 thermocouples. Each crystal is separated by a stainless steel slab with different thickness. The tungsten filter is placed on the top of the probe in order to block the electrons coming from the top [97].

Two probe designs had been tested before the final probe, which is used throughout this article, was developed. The first probe consists of two YSO crystals separated by 8 mm thick tungsten. The crystals are shielded from ambient light and electrons with energies less than 3 MeV by the 5 mm thick graphite housing. The crystals are connected to a Hamamatsu R928 photomultiplier tubes. When electrons hit the crystals, light is produced. The light is transferred to the photomultiplier by optical fibers. The light output is proportional to the number of the incident electrons. The second probe aims at spectrally and temporally resolved measurements of REs. Ten of YSO crystals were separated by tungsten with thickness from 0 to 6 mm. The probe is sensitive to REs with energies between 4 and 40 MeV and has an energy resolution of about 4 MeV and a temporal resolution of about 0.05 ms. The high temporal resolution of the probe enables the measurement of REs during disruptions.

Since the maximum energy of REs in TEXTOR is 30 MeV [4], in the third probe, stainless steel is used instead of tungsten. For REs with energies exceeding some 10 MeV, they lose their energy mainly due to γ radiation when they penetrate through tungsten while they lose energy by elastic col-

lisions in lower Z material like iron. As the YSO crystal is sensitive to both energetic electrons and γ radiation, the lower Z material allows for a more precise measurement of the spectrum than the previous probes.

The final probe consists of 9 crystals and 2 thermal couples separated from each other by stainless steel (see Fig. 18). From the electron approach direction, crystals 1 - 9 are placed behind stainless steel slabs with a thickness of 0 mm, 1 mm, 2 mm, 2.5 mm, 3.5 mm, 4.6 mm, 5.5 mm, 7 mm and 9.5 mm, respectively. Its temporal resolution depends on the RC loading time which can be adjusted by using variable resistors. The absolute calibration of the probe is performed by applying the monoenergetic electron beam generated by the accelerator ELBE at the Forschungszentrum Dresden Rossendorf [96]. The probe calibration obtained from the GEANT4 simulation shows that the effect of bremsstrahlung and neutrons are negligible.

5.3 Heat load probes of REs

The purpose of the heat load probe is the investigation of the damage of this probe by the energy deposition of the REs. The inner cylinder of the probe consists of spherical copper particles with maximum diameter of 100 μm embedded in a matrix of an epoxy resin (88% Cu : 12% epoxy resin). Copper powder is chosen as a high Z-material which strongly absorbs the runaways while the resin melts at sufficient low temperature and releases the heated copper powder. The probe head is attached to a stainless steel cylinder. The cylinders are shielded from the ions and electrons with energies below 4 MeV by a 5 mm thick EK 98 fine grain graphite housing (see Fig. 19). The vacuum gap between the inner core and the housing minimizes the conduction heat loss.

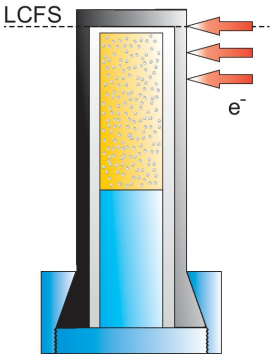

Fig. 19. Schematic of the longitudinal cross section of the heat load probe. The probe core, which consists of epoxy resin and copper particles, is attached to the stainless steel mounting and covered by the graphite housing [98].

High energy REs penetrate through the graphite housing and deposit their energies mostly in the copper particles because of the high stopping power of

copper [115]. The copper particles are heated up above 300°C. The damages observed in the probe indicate the presence of REs. The energy spectrum and the decay length of the REs can be obtained by comparing the experimental results with three-dimensional GEANT4 code based simulations. The probe has been designed for the analysis of a single disruption. Therefore, it was expected that the probe should be de-structured by the runaway impact.

5.4 Calorimeter probe of REs

This probe consists of 4 layers separated from each other by a vacuum gab. The first and the fourth layers are 4 mm thick slabs of a carbon fiber composite (CFC) which can withstand high heat load. The CFC layers shield the second and third layers against the thermal plasma. The second and third layers are a 35 mm thick slab of isotropic EK98 fine grain graphite and a 6 mm thick slab of molybdenum, respectively. The vacuum gaps between the layers reduce the conduction heat loss. The probe is thermally insulated against the stainless steel holder by Sintimid, an amorphous high temperature polyimide. The radiation is another source of heat loss. The heat radiation of the graphite and the molybdenum surfaces can be, nevertheless, assumed as minor. The graphite radiates 0.6 W and the molybdenum 0.1 W through the surfaces at the temperature of 300°C. The thermocouples are placed 5 mm below the plasma facing surfaces and the opposite ends of the second and third layers as well as in the Sintimid as shown in Fig. 20.

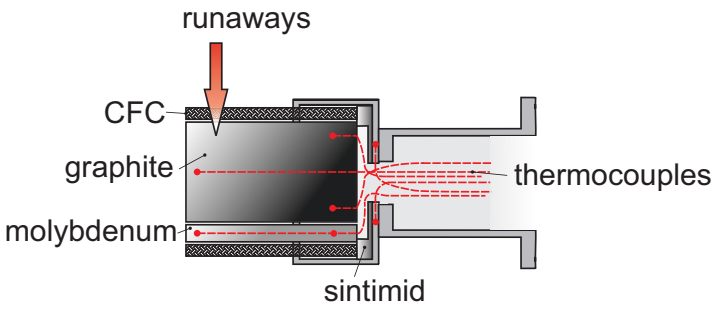

Fig. 20. Scheme of the calorimeter probe (top to bottom): a 4 mm thick slab of CFC, a 35 mm thick slab of EK 98 graphite, a 6 mm thick slab of molybdenum and a 4 mm thick slab of CFC. Each slab is separated from each other by a vacuum gap and all slabs are separated from the holder by a slab of Sintimid. (Reproduced with permission from [99]. Copyright 2012, AIP Publishing LLC.)

A GEANT4 based simulation shows that the REs with energies exceeding 2 MeV can penetrate through the CFC slab and heat up the graphite and molybdenum slabs. The maximum temperature of the molybdenum is at the

front surface. The temperature then decreases exponentially with radius. In case of graphite, the position of the maximum temperature is shifted a few mm away from the front surface due to the edge layer effect of runaway scattering in the CFC slap.

All probes are mounted on a fast radial drive. This makes the probes very suitable for the analysis of the edge of the runaway beam, in particular for the analysis of the edge gradient in a stable and reproducible discharge. This type of low density discharges has been intensively studied at TEXTOR for many years. Most measurements had been performed by the synchrotron radiation. The probe technique is a very suitable supplement to the previous measurements and, in addition, it provides information about the low energy part of the runaway spectrum which we did not have before.

6 Runaway electrons in low–density discharges

Although REs are unlikely to be generated during normal operations of present-day tokamaks, a runaway discharge can be obtained under certain conditions. In TEXTOR, the line average electron density has to be lower than $1{\times}10^{19}$ m^{-3} and the toroidal magnetic field greater than 2 T. As the critical field is proportional to the electron density, a low electric field is required for RE generation in the low density regime. The REs are created throughout the discharge.

6.1 Previous experiments on TEXTOR

On TEXTOR, the emission of synchrotron radiation in the mid IR spectral region ($4\mu m \leq \lambda \leq 8\mu m$) has been discovered in 1990 [4, 25, 26] which means that the high energy runaways have an energy exceeding $E_k \geq 25$ MeV. The experimental conditions for the creation of REs are low density discharges (Ohmic or with NBI / ICRH heating) at a line averaged density of $n_e \leq 0.5\ 10^{19}\ m^{-3}$. The spectral range is well accessible by IR-cameras which normally are used for thermography of plasma facing components. Because the synchrotron radiation is emitted only in a narrow angle in forward direction of the path of the REs, the integration along the line of sight can be ignored in a tokamak if the observation direction is toroidally. The first investigations have confirmed that the radiation is indeed synchrotron radiation and that the orbits of the REs have a perpendicular component of about $v_\perp/v_\parallel \approx 0.1$. The energy of the REs has been measured from the synchrotron spectrum by using different IR-interference filters in front of the camera; the spectrum shows a characteristic exponential decay towards smaller wavelengths, which depends on the RE energy and the perpendicular momentum. The total number of the high energy REs in low density discharges has been determined to a few times 10^{14} while the total number of electrons amounts to about $3.5\ 10^{19}$ particles.

An important part of the investigations has been the analysis of the importance of the secondary generation of the REs after their initial creation in the early phase of the discharge. The runaway development agrees well with the model of Besedin and Pankratov [36].

A highlight of the observations has been the detection of a runaway beam trapped in a magnetic island [116]. The discharge has been initiated in the normal way as at low densities. At t 2.5 s a pellet has been injected into the discharge which led to a sudden loss of a large fraction of the REs. However, by the injection a major size magnetic island has been created in which the REs remained confined. In the picture of the IR-camera the image of the island beam appeared several times during a frame because the plasma was rotating and therefore the beam reappeared in the image. It should be noted that at this time an IR-scanner was used as camera; this scanner creates its picture by two scanning mirrors (a fast sweeping one for the horizontal deflection and a slower one for the vertical one). By this technique a high time resolution is kept even during one frame; this finally was important for the interpretation of the pictures.

6.2 Energy spectrum of REs

The scintillator probe has been used to measure the runaway losses from the plasma in TEXTOR [117]. Each scintillator crystal inside the probe is sensitive to REs with different energies depending on the position of the crystal. Assuming that the probe acts as a limiter and all REs which are leaving the plasma strike the probe, the energy spectrum of REs can be deduced from the probe signal. In this way it is possible to measure not only the high energy part of the RE-spectrum but also the runaways in the energy range of 4 MeV $\leq$ 25 MeV.

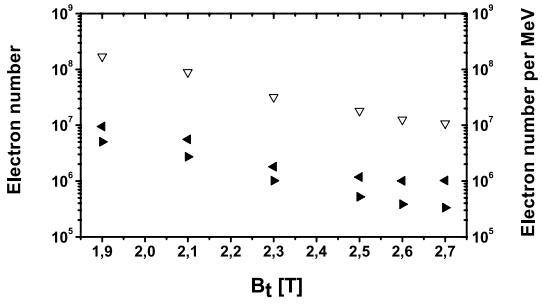

Fig. 21. The number of REs in the low density discharge regime as a function of the toroidal magnetic field: ($\bigtriangledown$) the total number of REs integrated over energy and the averaged number of REs per 1 MeV with energies of (◀) 6 MeV and (▶) 16 MeV at 3 s after the start up of the discharge [117].

As the runaway spectrum becomes stationary at t $\geq$ 2 s, the ratio between RE number at 6 MeV and 16 MeV does not change significantly with B_t (see Fig. 21). The number of REs at 6 MeV is larger than those of the higher energies as expected. They are different by a factor of 2 or 3. In comparison with the total RE number ($\bigtriangledown$), the spectral runaway numbers (◀ and ▶) are

about one order of magnitude smaller and their exponential decay is about similar.

6.3 Diffusion coefficients at different B_t and magnetic turbulence level

At different devices, several techniques have been applied to measure the runaway diffusion coefficient, D_r. The perturbation techniques, namely a plasma shift and an externally applied helical resonance magnetic field, enables the measurement of the D_r. When the plasma column is suddenly shifted inward, the runaway orbits are dragged away form the outer limiter. The runaway flux at the outer limiter then drops and the REs have to diffuse over a longer distance. This technique provides the D_r in the plasma edge region. In ORMAK [54], the D_r in the range of 0.01 - 1 m^2s^{-1} was estimated from the flux of runaways to the outer limiter under various discharge conditions. In the stochastic magnetic field layer generated by externally applied magnetic fields, the runaway transport is enhanced. The REs are expected to diffuse immediately to the boundary. This technique allows the measurement of the D_r in a deeper region in the plasma compared with the plasma shift technique [118]. Without externally applied perturbations, the D_r can be deduced from bremsstrahlung radiation spectra and from sawtooth oscillations of HXR flux and SXR intensity. In TJ-I [119], the D_r obtained from both methods are similar, i.e. in the range of 4 - 10 m^2/s.

In TEXTOR [120] and JET [121], the D_r at the plasma core were studied. The measurement of the synchrotron radiation emitted by REs at the plasma core provides the runaway density. By using a simple diffusion model, the runaway diffusion coefficient profile can be deduced from the gradient of the REs density. Another method of estimating the D_r is the measurement of the perpendicular X-rays emitted by REs. A diffusion model, which simulates the evolution of the line integrated X-ray signals, was used to determine the D_r in JET. It has been found that the diffusion coefficient of thermal electrons is 2-3 orders higher than that of the REs. One possible cause for the difference is the electrostatic turbulence which influences the diffusion of thermal electrons but not the runaway transport. The REs are affected only by the magnetic turbulence.

In order to derive a diffusion coefficient, we used Ficks equation Γ: $D_r = \Gamma/\nabla n_r$ where Γ is the runaway loss at the boundary. The absolute number of runaways and its gradient ∇n_r are taken from the synchrotron measurements.

In Fig. 22 the synchrotron intensity is given in arbitrary units as a function of B_t. One clearly sees that the runaway number increases as a function of B_t while the edge loss decreases (see Fig. 21). Therefore, the underlying diffusion coefficient drops strongly with increasing B_t as shown in Fig. 23. The diffusion coefficient is of the order of 10^{-3} m^2/s and decreases between 2 T and 2.7 T by an order of magnitude.

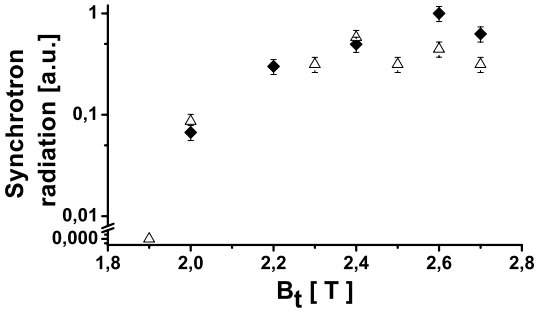

Fig. 22. Synchrotron radiation intensity for plasma currents of 300 kA (△) and 400 kA (⧫) as a function of the toroidal magnetic field. The error bars show the standard deviation [117].

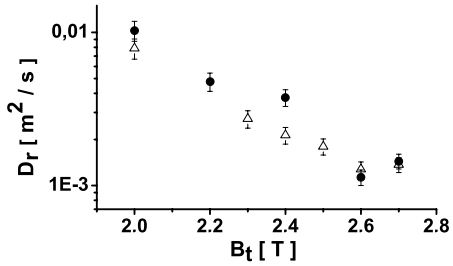

Fig. 23. The diffusion coefficient for plasma currents of 300 kA (△) and 400 kA (•) as a function of the toroidal magnetic field [117].

The result of the calculation of magnetic fluctuation during the stationary phase of the discharge by using the formula (4.21) is shown in Fig. 24. The magnetic turbulence level of the order of 10^{-5} T is estimated. The turbulence level decreases by an order of magnitude between 1.6 T and 2.7 T, i.e. the losses of the runaways are substantially larger at low B_t.

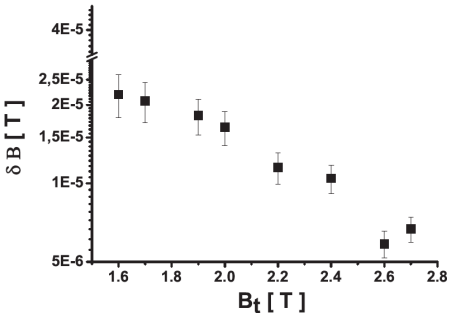

Fig. 24. Fluctuation level during the stationary phase of the discharge determined by using Myra and Catto's model [65] as a function of the toroidal magnetic field [97].

6.4 Losses of REs due to magnetic perturbations of the TEXTOR–DED

Now we discuss the experimental measurements of RE losses induced by the DED magnetic field perturbations. As have been shown in Sec. 4.6.1 in the

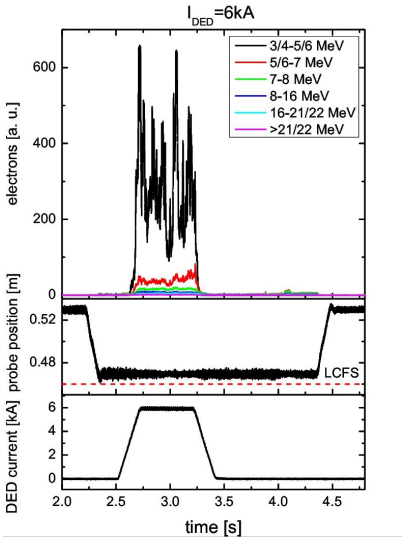

Fig. 25. Temporal evolution of (a) the RE probe signal, (b) the radial position of the probe head and (c) the DED current with a plateau at 6 kA [21]. The TEXTOR discharge #112914.

presence of this perturbation magnetic field the magnetic surfaces and drift surface close to the plasma edge are destroyed forming the stochastic layer open to the wall. REs in this stochastic layer are quickly lost due to radial transport.

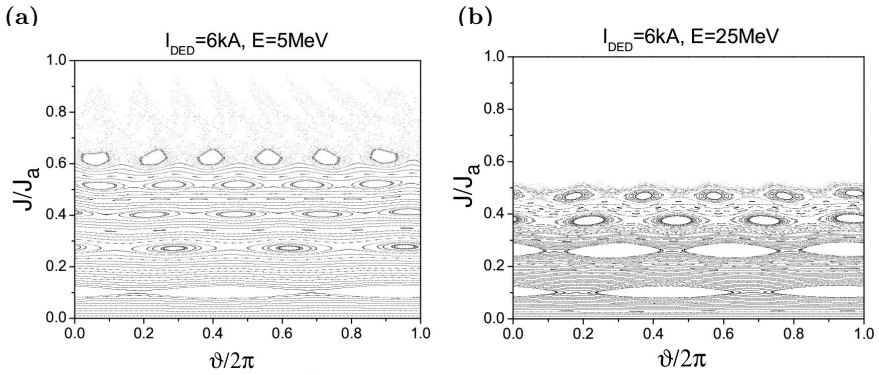

Fig. 26. Poincaré plot of REs with an energy of **(a)** 5 MeV and **(b)** 25 MeV for the DED current of 6 kA and the amplitude of the magnetic turbulence of $\epsilon = 1.41 \times 10^{-5}$ [21].

Figure 25 shows traces of the loss of REs with different energies in a low density discharge regime. Here, the DED is operated in the $m/n = 6/2$ operational mode with $I_{DED} = 6$ kA. This mode is favourable for the in-

vestigations because the perturbation field penetrates deep enough into the plasma but does not excite a tearing mode as it tends to happen in the $m/n = 3/1$ operational mode. The probe is moved shortly before the onset of the DED to the plasma edge at a radius of $r = 0.46$ m and stays there until $t = 4.3$ s (see Fig. 25 (b)). Figure 25 (a) shows the loss of REs in energy ranges hitting the scintillator probe. One clearly sees that the low–energy REs have the largest loss because their population is naturally higher than that of the high–energy REs. On the other hand as was discussed in Sec. 4.6.1 the effect of perturbation magnetic field on the low–energy REs is less screened than on the high–energy REs.

Below we model the transport of REs affected of the TEXTOR–DED coils taking into account the turbulent magnetic background field [21]. We first evaluate Poincaré plots of the orbits of the REs with different energies for the DED current of 6 kA. Figure 26 shows Poincaré plots for the energy of 5 MeV and 25 MeV. The innermost flux surfaces are regular, followed by island formations and ergodic zones further outside. The low energy orbit plot shows a higher ergodicity than the high energy one. In the upper part of the Poincaré plots, data dots are missing because the orbits intersect the wall. Since the high energy runaways are more shifted to the outside than the low energy ones, the data for the flux function of higher than about 0.5 are missing (see Fig. 26 (b)).

In Sec. 4.6.1 we calculated the diffusion coefficients D_r of REs in the presence of DED perturbations alone. Now we calculate D_r taking into account the magnetic turbulence. To simplify the calculations the latter will be considered as random kicks to the action variable. After each integration step $\Delta\varphi$ the action variable J is randomly kicked up or down by an amplitude ΔJ,

$$\Delta J = \sqrt{2D_{\varphi}^{(turb)}(J)\Delta\varphi}, \tag{6.1}$$

determined by the turbulent diffusion coefficient $D_{\varphi}^{(turb)}$ (4.11) with $K_{mn}(J, E)$ given by (4.17) (see also Secs. 4.4 and 4.5).

The diffusion coefficient D_r of REs affected by the both, DED perturbations and and the turbulent magnetic perturbations, is calculated numerically similar to the one in Sec. 4.6.1. We recall that the relation between the diffusion coefficient D_r in the normal space and $D_{\varphi}(J)$ is given (4.10). Figure 27 shows the diffusion coefficient for the DED current of $I_{DED} = 6$ kA.

To study the evolution of the RE density $n = n(r, E, t)$ we have used the diffusion equation in a cylindrical geometry,

$$\frac{\partial n(r,t,E)}{\partial t} = \frac{1}{r}\frac{\partial}{\partial r}\left[rD_r\frac{\partial n}{\partial r}\right] - \frac{c}{2\pi R}V_{loop}\frac{\partial n}{\partial E}, \tag{6.2}$$

satisfying the boundary conditions,

$$n(r,t,E)\big|_{r=a} = 0, \qquad \frac{\partial n(r,t,E)}{\partial r}\Big|_{r=0} = 0, \tag{6.3}$$

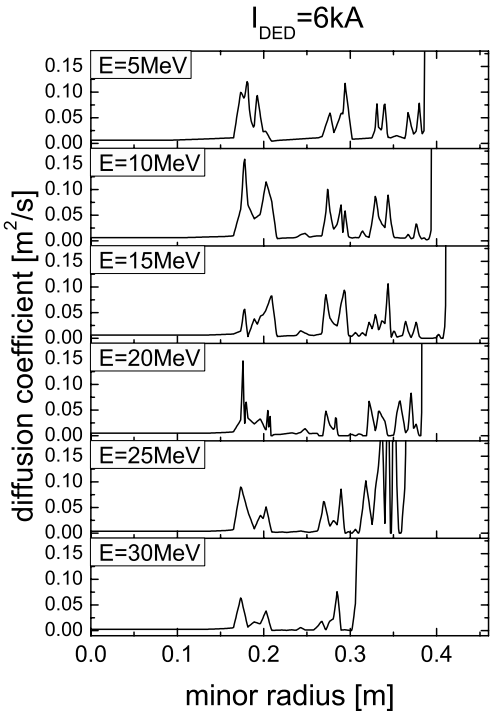

Fig. 27. Local diffusion coefficient of REs with different energies. The DED current of 6 kA is applied and the amplitude of the magnetic turbulence is of $\epsilon = 1.41 \times 10^{-5}$ [21].

at the plasma edge $r = a$ and at the plasma center $r = 0$. The last term in the right–hand side of (6.2) describes the acceleration of electrons by the loop voltage V_{loop}. The secondary generation of REs is implemented by the condition,

$$\frac{\partial n(r,t,E)}{\partial t} = \beta n_{e0} F(r) \int_{E_{min}}^{E_{max}} n(r,t,E) dE, \tag{6.4}$$

where $F(r)$ is the form function $F(r)$ chosen as

$$F(r) = \left[1 - (r/a)^2\right]^{\nu}, \qquad \nu = 2,$$

and β is the fitting parameter describing the efficiency of the secondary RE generation. We have set the following limits of the integral: $E_{min} = 5$ MeV and $E_{max} = 15$ MeV, and assumed that the secondary REs are generated at $E = 4$ MeV. This assumption is in accordance with the predictions of the avalanche theory that the secondary REs are generated at $E \leq 4$ MeV.

The number of the RE population by the secondary generation is controlled by setting $\beta n_{e0} = 0.38\,(\mathrm{MeV} \cdot \mathrm{s})^{-1}$ where $n_{e0} = 5 \times 10^{18}\,\mathrm{m}^{-3}$ is the central thermal electron density. By varying β, the slope of the increase of

the RE density throughout the discharge can be fitted to experimental observations. Choosing n_{e0} determines the absolute level of the generated RE density. As initial condition $n(r, t = 0; E) = n_0 F(r) \exp(-E/E_0)$ is chosen with the central RE density $n_0 = 5 \times 10^{11}\,\mathrm{m}^{-3}$ and the e-folding energy $E_0 = 10\,\mathrm{MeV}$.

The RE flux Γ at the plasma edge and the RE number N_{RE} in the plasma volume are determined by

$$\Gamma(r = a, t, E) = D_r \frac{\partial n(r = a)}{\partial r} 4\pi^2 aR,$$
$$N_{RE}(t, E) = 4\pi^2 R \int_0^a n(r, t, E) r dr. \tag{6.5}$$

Since the Dreicer effect is not taken into account, this model is valid for the REs with energies above 4 MeV.

The equation (6.2) with the boundary condition (6.3) is solved numerically by the 2D partial differential equation (PDE2D) solver [122]. A special difficulty is that the higher diffusion coefficient of the low energy fraction of the runaways influences also the high energy part, because the runaways are gradually accelerated from low energy to larger energies. Finally, we compare the experimental results to the results of the model and iterate our model assumptions until a good agreement is obtained. The model provides information of the time development of the runaways and their radial profile. It was up to now only applied to the slowly developing runaways of the low density plasmas including those plasmas with additional resonant magnetic perturbations provided by the Dynamic Ergodic Divertor (DED) in TEXTOR. The numerical approach has not yet been applied to the disruption because there are too many uncertainties.

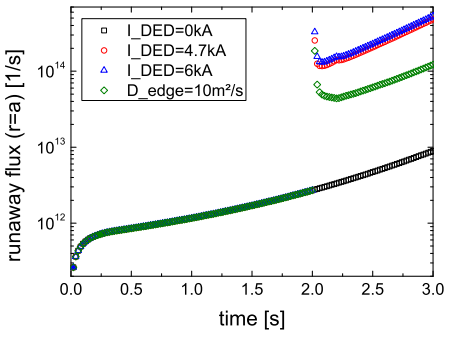

Fig. 28. The simulation result of the runaway flux at the plasma edge integrated over the electron energy for different DED currents [21].

The runaway flux of unperturbed discharges increases smoothly. When the RMPs are applied, the sudden rise in the runaway flux is observed (see

Fig. 28). At t = 2 s, the DED current is ramped up slowly until it reaches the value of 4.7 kA or 9.7 kA at $t \leq 2.2$ s. Then it is kept constant until the end of the simulation, i.e. $t = 3$ s. Due to the large amplitude of the RMPs in case of $I_{DED} = 6$ kA, the runaway flux is higher than that in case of $I_{DED} = 4.7$ kA. After the rapid increases in the runaway flux at $t \approx 2$ s, the runaway flux in both cases develops with the same slope as in case of the unperturbed discharge. In the last case, in which the diffusion coefficient at the edge is set to 10 m^2/s in order to obtain the open trajectories at the edge, the runaway flux also increases. However, the runaway flux in this case is much lower than the previous cases. This indicates that not only the stochastization of the magnetic field at the plasma edge but also the change of the magnetic topology inside the plasma has a strong influence on the runaway transport.

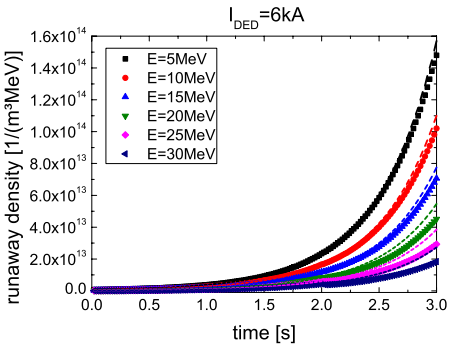

Fig. 29. Temporal evolution of the RE density at different RE energies for a DED current of 6 kA [21].

The time evolution of the runaway density in case of $I_{DED} = 0$ kA (dashed lines) and $I_{DED} = 6$ kA (data markers) are presented in Fig. 29. Without perturbed field, the runaway density increases exponentially according to the secondary generation. As the DED field is applied, the runaway density drops slightly and then deviates from the previous case. The growth rate of the high REs decreases more strongly than that of the lower ones because the REs are lost before they have enough time to gain high energies.

Figure 30 shows the RE flux spectra $\Gamma(r = a, E)$ at $t = 3$ s. The unperturbed case in Fig. 30(a) is characterized by a peaked flux spectrum. The maximum is at about 8 MeV. In contrast, for $I_{DED} = 6$ kA the flux shows a steep decrease coming from $E = 4$ MeV. Going to higher energies the behavior seems to be noisy and it shows a peak at 15 MeV. This peak remains the same when the grid size or the number of time steps used by PDE2D are changed. Instead, flattening the profile of the diffusion coefficient, leads to a reduction of the "noise" and the peak which suggests that both are real physical effects rather than artifacts of the model. The discussion of this result in comparison with the measurements adds a new issue to the understanding of the RE transport.

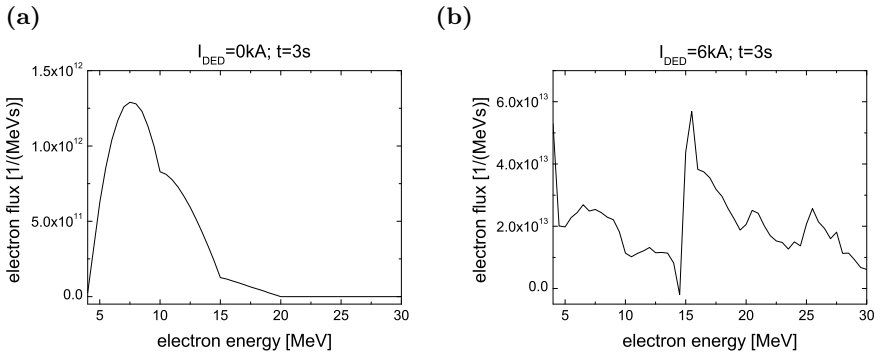

Fig. 30. Runaway flux spectra taken at the end of the simulations: (a) Without external perturbations; (b) With the RMP at $I_{DED} = 6\,\mathrm{kA}$ [21].

Many details of the model agree well with the experimental results, e.g. the growth of runaways in the plasma center (synchrotron observation) and the loss at the plasma edge. A critical parameter for the simulation is the amplitude of the magnetic turbulence. Only with the given amplitude we can reproduce the growth rate of the runaway number; a lower (higher) value of the amplitude would lead to a too fast (slow) growth of the runaway number relative to the observation. This modeling is an interesting means to determine the loss rate of the REs.

7 Runaway electrons during plasma disruptions

REs are not only observed in low density discharges but also during disruptions. The low density discharges are a niche for performing basic physics experiments. In fusion devices, REs are a crucial issue for tokamaks because of the possible damage resulting from their impact at the vessel wall. Decades ago, tokamaks consisted of pure metal components. Melting traces of runaways were usually found at the limiters. In the devices with graphite walls, limiters or divertors the damage traces are no longer obvious. Nevertheless, runaways are still observed during disruptions. A means to create the REs regularly is a massive injection of gases, particularly argon. For this purpose, a large amount of gas is injected by a disruption mitigation valve. The experiments are performed under constant conditions in order to create reproducible disruptions.

In low density discharges, the runaways are well reproduced and their position is well controlled. During disruptions, the position control is much more difficult. The main reason is that the feedback circuits for the position control become saturated during the thermal quench and therefore the regular position feedback is no longer useful. The only means of influencing the runaway position is a preprogrammed setting of the control currents. However, this method is not always reliable and it may change from day to day. In the following we present the results of the total energy content of the runaways during TEXTOR disruptions, runaway structures at the plasma center and the edge and runaway mitigations.

Previous observations. As in other devices disruptions are rather reproducibly triggered by the fast injection of about 10^{22} atoms of argon. Aim of investigations of M.Lehnen [20] on TEXTOR was the search for possibilities the eliminate those runaways again. This task was performed by the use of the Dynamic Ergodic Divertor, DED, on TEXTOR operating in the $m/n = 3/1$ mode. The REs were indeed suppressed, if the DED was switched on about 200 ms before the trigger of the disruption. The early onset of the DED is necessary, because the rise time of the DED current is limited by its inductivity. The investigations were resumed later again (see Sec. 7.4.2) where it was shown that at this mode of operation also a tearing mode is triggered inside the plasma.

7.1 Calorimetric measurements

For the calorimetric measurements, the probe shown in section 5.4 was constructed. The probe is inserted shortly before the disruption into the plasma edge at the limiter radius, i.e. $r = 46$ cm and stays there over the disruption. In this way, the probe intercepts all runaways which are lost during the disruption, however, without time resolution.

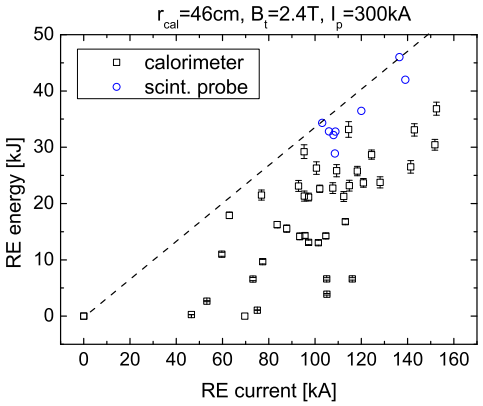

Fig. 31. Energies of REs measured by the calorimeter probe and by the scintillator probe during the RE current. The initial current is $I_p = 300$ kA. The upper limit of the data is indicated by a dashed line. (Reproduced with permission from [99]. Copyright 2012, AIP Publishing LLC.)

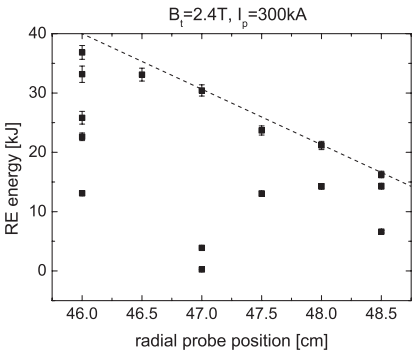

Fig. 32. Energies of REs measured by the calorimeter probe over the radial probe position. The upper limit of the data is indicated by a dashed line. (Reproduced with permission from [99]. Copyright 2012, AIP Publishing LLC.)

Figure 31 shows the dependence of the measured RE energy on the runaway current for the the toroidal magnetic field of B_t =2.4 and the predisruptive plasma current of $I_p = 300$ kA. The graph presents the measurements of the calorimeter probe and the scintillator probe. The REs sometimes strike the probe only partially or even miss it and hence the large scatter of the data points. There is, therefore, a tendency to underestimate the total RE energy. Nevertheless, it can be clearly seen that there is an upper limit of

the RE energy indicated by the dashed line in Fig. 31. Consequently, a linear dependence of the RE energy on the RE current can be concluded. This is strengthened by the scintillator probe results. Typical runaway current for TEXTOR disruptions is $I_{re} \approx 100$ kA corresponding to the RE energy of 30 to 35 kJ. As the probe is placed at the last closed flux surface (LCFS), the RE energy deposited on the probe decreases linearly with the radial position of the probe (see Fig. 32) because the runaway energy spreads over the plasma facing components (PFCs) increases.

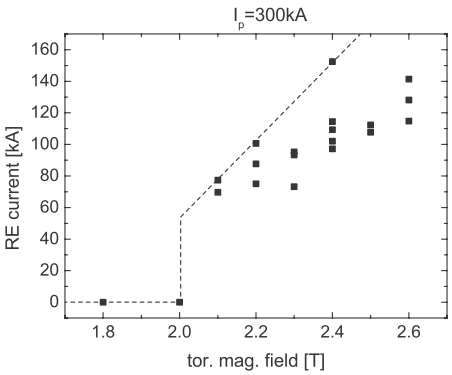

Fig. 33. RE currents as a function of the toroidal magnetic field B_t. The upper limit of the data is indicated by a dashed line. (Reproduced with permission from [99]. Copyright 2012, AIP Publishing LLC.)

As can be seen in Fig. 33, the magnetic threshold for runaway generation in TEXTOR is $B_t = 2$ T. For $B_t \leq 2$ T, no RE is observed. For higher magnetic field, the runaway current increases linearly with the toroidal field. If the magnetic field is kept constant at $B_t = 2.4$ T, the runaway current and energy increase with increasing plasma current. Figure 34 presents the conversion efficiency, i.e. the ratio between the runaway energy and the magnetic energy, $E_{mag} = \frac{1}{2} I_p^2 L_p$. The inductance is determined by

$$L_p = \mu_0 R \left(\ln \left(\frac{8R}{a} \right) - 2 + \frac{\ell_i}{2} \right). \tag{7.1}$$

Here, following parameters are used: the major radius $R = 1.75$ m, the minor radius $a = 46$ cm and the internal inductance $\ell_i = 1.2$. The energy conversion efficiency decreases with increasing current. This agrees well with the results from the scintillator probe. The maximum conversion efficiency is about 26% consistent with with the results at JET [123].

7.2 Runaway electrons at the plasma edge

The runaway heat load probe has been designed for a single shot measurement in which it will be destroyed. The probe was inserted 5 mm into the plasma

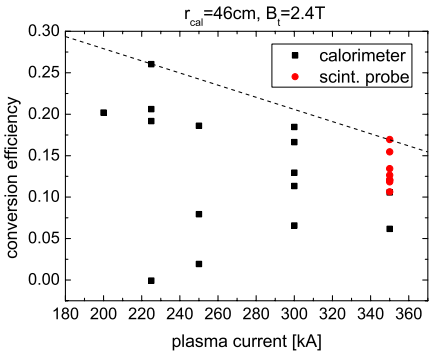

Fig. 34. Conversion efficiencies of the pre-disruptive magnetic plasma energy into RE energy over the plasma current measured by the calorimeter probe and by the scintillator probe over the RE current. The upper limit of the data is indicated by a dashed line. (Reproduced with permission from [99]. Copyright 2012, AIP Publishing LLC.)

shortly before the disruption is triggered. On the one hand, the low energy particles deposit the major part of their energies on the housing. The thermal shock causes cracks on the housing. On the other hand, the REs with energies exceeding 4 MeV penetrate through the housing and heat the core of the probe abruptly. After the runaway impact, a part of epoxy resin is evaporated leading to an increases of the pressure inside the probe. The top part of the housing, which has cracks, is then pushed off. The core of the probe after dismounting the housing is shown in Fig. 35. The damage to the core of the probe is located exclusively on the electron side. On the ion side of the probe, there is no visible damage found.

Fig. 35. The core of the heat load probe after runaway impact [98].

The scanning electron microscope picture of the damaged part shows no sign of the molten copper particles (see Fig. 36). The copper particles are dispersed randomly in the epoxy resin matrix and are not in contact with each other. As a part of epoxy resin is evaporated. The damaged area becomes

unstable. The copper particles then fall out resulting in the holes observed in Fig. 36. The view of the damage area is shown in Fig. 37. The damaged area are outlined by the yellow and green lines. Cracks parallel to the surface are observed but no damage deep inside the core is present.

The cross section of the probe core was obtained by applying an additional epoxy resin to the probe before cutting it by the wire erosion in order that the damaged part stay at its position and do not break apart during the bisection process.

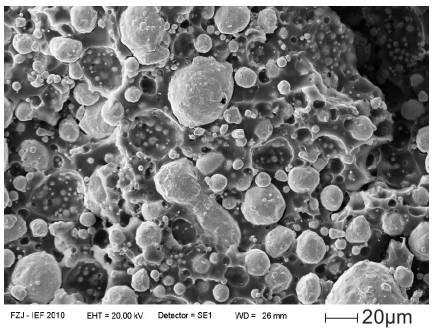

Fig. 36. Scanning electron microscope picture of part of the damaged region of the heat load probe [98].

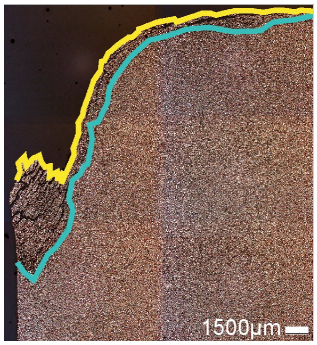

Fig. 37. Longitudinal cross section of the core of the probe. A yellow and green curves outlines the runaway damages, cracks and the holes [98].

The thermogravimetric analysis agrees well with the simulations done by using GEANT4 code for a runaway beam with exponential spectrum with an e-folding length between 4 MeV and 9 MeV, i.e. the exponential radial decay with an e-folding length between 13 mm and 6 mm. For the mono energetic parts of the exponential spectrum, the best match is found between the experimental result and the simulation for runaway energies between 8 MeV and 16 MeV.

7.3 Runaway electrons at the plasma core

In order to visualize the core part of the REs, the synchrotron measurement technique is applied. As already mentioned before, the plasma position control is much more sophisticated in a disrupting plasma than in a quiet discharge. In addition, we were hampered by the partial vignetting of the IR detection system at the high field side of the torus. Nevertheless, we succeeded to obtain sufficient data for achieving important characteristics of the runaways.

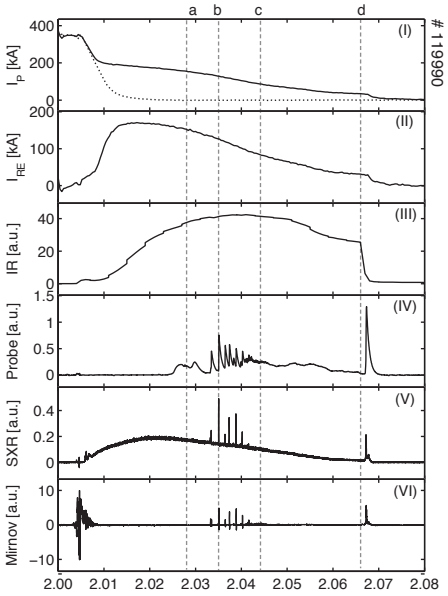

Fig. 38. Temporal evolution of disruption discharge # 119990 (top to bottom): (I) time trace of the plasma current and of the current without REs (dashed curve), (II) the runaway current, (III) the spatially integrated synchrotron radiation, (IV) the scintillator probe signal, (V) the soft X-ray signal and (VI) the Mirnov signal. Dashed lines a - d corresponds to the IR image shown in Fig. 39.

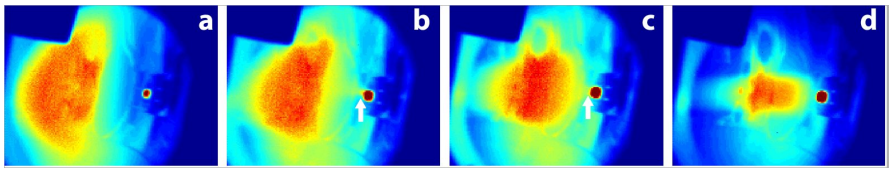

Fig. 39. IR images observed by the camera for discharge # 119990 taken at **(a)** $t = 2.029$ s, **(b)** $t = 2.035$ s, **(c)** $t = 2.044$ s, and **(d)** $t = 2.066$ s. A small red spot at the right field side of the image presents the heated scintillator probe tip. The loss channel is indicated by white arrows.

A typical example of an induced disruption in the TEXTOR tokamak is shown in Fig. 38 (see [85]). At the beginning of the current quench the

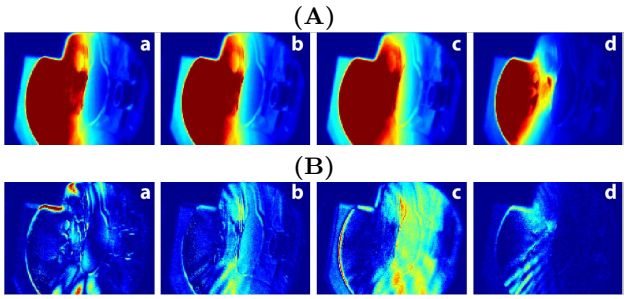

Fig. 40. **(A)** IR images observed by the camera and **(B)** the images obtained from subtracting consecutive images of the discharge # 119874 taken at **(a)** $t = 2.042$ s, **(b)** $t = 2.072$ s, **(c)** $t = 2.084$ s and **(d)** $t = 2.096$ s.

fast plasma current decay stops and it is replaced by slow decay forming a long plateau, which indicates the presence of runaways. In runaway-free disruptions, only an fast decay is observed as shown in Fig. 38 (I) (dashed curve). Runaway bursts, Mirnov signal spikes and SXR spikes are present during the plateau phase. During this phase the loss channel, which connects the plasma edge to the scintillator probe, builds up which can be seen in Fig. 39). An intensity of the IR radiation at the center of the runaway beam remains almost constant, while the intensity at the edge and inside the loss channel changes with time. Later in the disruption when the plasma current is already low, the runaway beam shrinks and takes an oval shape oriented horizontally before it suddenly disappears at the end of the discharge.

The Fig. 40 (A) shows another sequence of synchrotron radiation decay during the disruption. The Fig. itself is little spectacular. However, since the synchrotron radiation is recorded by a fast IR camera with a delay between consecutive images of 0.8 ms only, one can subtract consecutive images and obtain information of the time derivative of the synchrotron development. In some of the sequences one observes a characteristic stripe pattern as shown in Fig. 40 (B). This stripe pattern is characteristic for the laminar zone of an ergodic system [81, 47].

The observed stripes in synchrotron radiation patterns are related to the structure of the stochastic zone formed at the edge of RE beam. Such a stochastic zone is created due to the interaction of high energetic electron orbits with the $(m = 1, n = 1)$ MHD mode. The typical structure of a stochastic zone was shown in Fig. 16 by the Poincaré section of RE orbits in the (R, Z)-plane (see also Sec. 8.4 and Fig. 52 (b)). As seen it consists of stability islands embedded into stochastic layer near the separatrix that open to the wall. The characteristic escape time of REs from the stochastic layer is of order of 10 μs. However, REs trapped by the stability islands stay longer and their synchrotron radiation can be seen. Due to the rotation of the $m/n = 1/1$ helical magnetic perturbation the stability islands also rotate.

This can explain the observed stripes in subtracted synchrotron radiation patterns.

In about 25 % of the induced disruptions observed during this campaign, the runaways survive the obvious end of the discharge, where the plasma current drops to almost zero as shown in Fig. 41. The plasma current seems to stop at $t = 2.015$ s, while the IR-synchrotron signal (IV) develops further and ends at $t = 2.03$ s. At a first glance, the SXR-signal stops with the plasma current. However, if the SXR signals is enhanced by an order of magnitude, one observes also low activities.

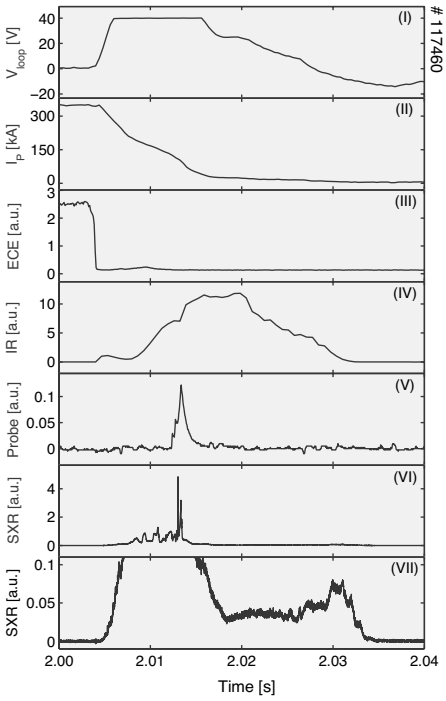

Fig. 41. Temporal evolution of the disruption of discharge # 117460: (top to bottom) time trace of the loop voltage, the plasma current, the electron cyclotron emission (ECE) signal, the intensities added over all pixels of the IR image, the scintillator probe signal, the soft X-ray (SXR) signal, and the magnified SXR signal [124].

The runaway current, I_{re}, is used to evaluate the total number of REs:

$$N_{tot} = \frac{2\pi R_0 I_{re}}{ce}. \tag{7.2}$$

In Fig. 38 (II), the maximum runaway current is 190 kA. It is corresponding to the total number of the REs of 4.33×10^{16}. If the radius of curvature of the runaways is known, the number of REs with energies higher than 25 MeV can be deduced from the synchrotron radiation integrated over the wavelength and the cross-section:

$$N_{RE} = \frac{L_\lambda A \Omega}{P_\lambda}. \tag{7.3}$$

Here A is the area of the runaway beam cross section, $\Omega = 2\pi \times 2\theta$, P_λ the power emitted by one RE and L_λ the absolute value of the radiance. The detailed description of the procedure can be found in [82, 4, 125]. Typical runaway parameters during an induced disruption in TEXTOR are $r_{beam} = 28 \pm 3$ cm and $\theta = 52 \pm 10$ mrad. From the IR image shown in Fig. 39 (c) the runaway number of 1.30×10^{16} is obtained. It is about 30% of the total RE number.

The measurements of the scintillator probe, the calorimeter probe, the bolometer probe and the synchrotron radiation show consistently that runaway electrons have exponential energy distribution. The number of REs decays exponentially from few MeV to 30 MeV with the decay rate of about $n_{r0} \approx 10$ MeV. The radial decay length amounts to about 5 mm $\leq \lambda_r \leq 10$ mm.

7.4 Mitigation of runaway electrons

Another goal was to investigate whether the REs generated during the current quench could be reduced by massive gas injection or by resonant magnetic perturbation fields. In a low density discharge, the REs had been successfully removed by gas injection. Therefore, we tried to investigate whether this method works also in case of disruptions, where the loop voltage is high. In our mitigation study, all disruptions are initiated by an argon puff injected at 2 s after the start up of the discharge.

7.4.1 Massive gas injection (MGI)

In addition to the disruption initiation valve, 2 similar valves are used to investigate the effects of massive gas injection on the runaway mitigation. The path of the injected gas has different lengths to the plasma for all three valves such that different delays have to be added to the given times of the valve trigger. In addition, the different path length of the gas results also in a different slope of the gas front of each valve. The two mitigation valves investigated here are mounted as close as possible to the plasma while the initiation valve has a distance of about 0.5 m. In this study, the biggest mitigation valve is not operated up to its full capacity.

The smaller mitigation valve was used first. The effect of 3 different types of gas puffs, namely helium, neon and argon, on the runaway confinement is investigated. 2.2 $\times 10^{22}$ atoms of gas is injected at different times. The injected gas enhances the runaway loss: the current decay rate increases and the Mirnov signal spikes and SXR spikes as well as the runaway bursts are present (see Fig. 42). The result from synchrotron observations is shown in Fig. 43 (A) for the "normal" IR recording and (B) for the subtraction mode, which enhances small changes by about an order of magnitude. In particular figure 43 (B) (a) indicates that the injected gas initiate the fluctuation at the

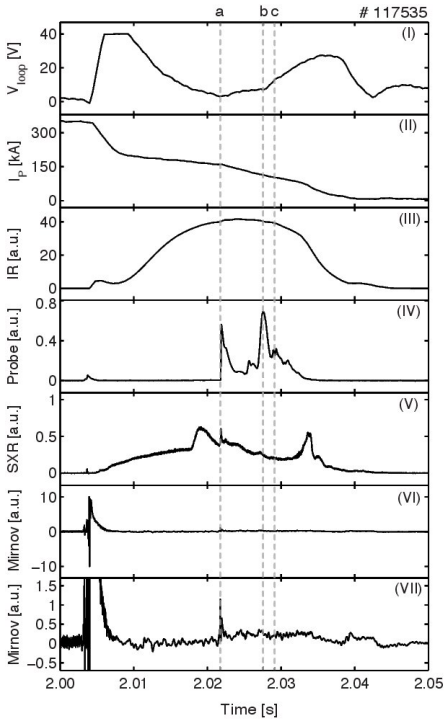

Fig. 42. Temporal evolution of the disruption of discharges # 117535, in which 2.2×10^{22} atoms of neon are injected at t = 2.015 s. Dashed lines a - c corresponds to the IR images shown in Fig. 43 [124].

edge of the runaway beam leading to the increased loss rate. However, the loss occurs mainly at the edge of the beam, while the REs at the center are still confined.

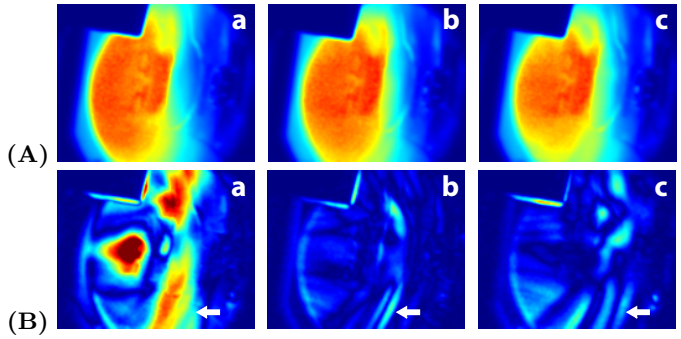

Fig. 43. **(A)** IR images observed by the camera and **(B)** the images obtained from subtracting consecutive images for discharge # 117535 at (a) t = 2.022 s, (b) t = 2.024 s, and (c) t = 2.027 s. White arrows indicate the structures which are not present in case of unmitigated disruption [124].

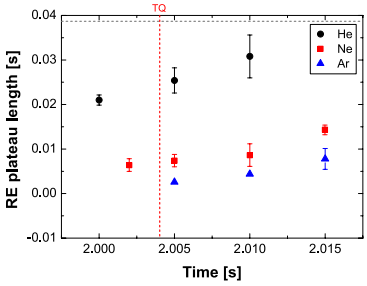

Fig. 44. Averaged runaway plateau length of disruptions mitigated by gas puffs of helium (black), neon (red), and argon (blue). 2.2 × 10^{22} atoms of gas is injected by the valve 2 at different times. The gray dashed line indicates an averaged plateau length of a typical induced disruption and the red dashed line the TQ time [124].

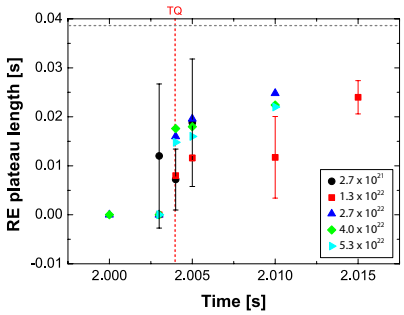

Fig. 45. Averaged runaway plateau length of discharge mitigated by an argon puff: 2.7 × 10^{21} atoms (black), 1.3 × 10^{22} atoms (red), 2.7 × 10^{22} atoms (blue), 4.0 × 10^{22} atoms (green), 5.3 × 10^{22} atoms (light blue). Gas puffing is performed by valve 3. The gray dashed line indicates an averaged plateau length of a typical induced disruption and the red dashed line the TQ time. The large error bars are caused by the strong deviation of the plateau lengths of some shots from the average values [124].

Figures 44 and 45 show the effect of the injected gas on the runaway confinement. The earlier the gas is injected, the shorter the runaway confinement time can be achieved. Among the test gases, argon provides the strongest effect. Therefore, in the investigation of the runaway mitigation effect of massive gas injection performed by the bigger valve only argon was used. The runaway beam develops slower and the runaway confinement time is shorter than that in case of unmitigated disruptions. The same trend as in previous case is observed, i.e. the stronger effect is achieved by earlier injection. As the bigger valve is located closer to the plasma and has a bigger orifice diameter, the injected gas can penetrate deeper in to the plasma in comparison with the case of the smaller valve. The disruption becomes runaway free if $\geq 1.3 \times 10^{22}$ atoms of argon is injected at t $\leq$ 3 ms after the disruption is triggered. For later injections, a significant amount of REs are present. The main constraint of this method is that the gas puff has to be injected prior to the thermal quench. Otherwise only a small part of REs are lost, while a major part is still confined.

7.4.2 Effect of resonant magnetic perturbations

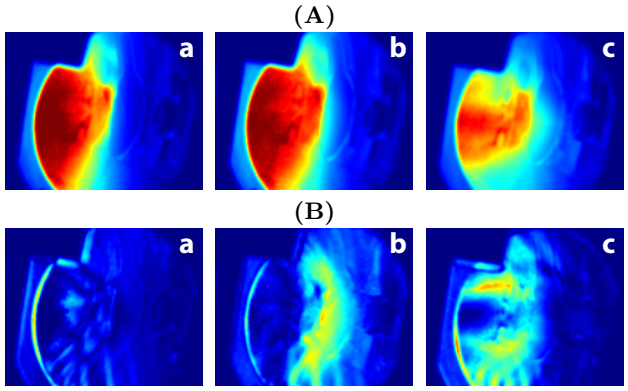

Fig. 46. **(A)** IR images observed by the camera and **(B)** the images obtained from subtracting consecutive images for discharge # 119889 at (a) $t = 2.047$ s, (b) $t = 2.050$ s, and (c) $t = 2.063$ s. The DED current of 1 kA is applied at $t = 1.82$ s [124].

Fig. 47. Averaged runaway plateau length of the induced disruptions mitigated by the DED 6/2 mode. DED currents of 4 kA (black), 6 kA (red), 6.5 kA (blue), and 7 kA (green) are applied (separately) at different times. The gray dashed line indicates an averaged plateau length of a typical induced disruption and the red dashed line the TQ time [124].

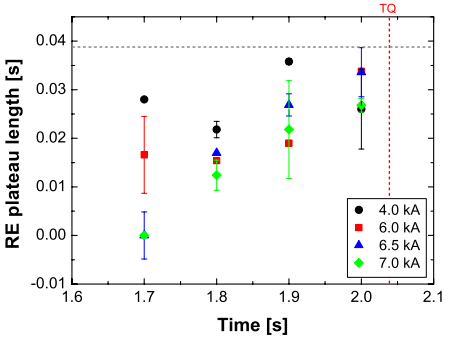

Effects of the resonant magnetic perturbations (RMPs) on the generation and transport of REs have been investigated in several tokamaks. In TEXTOR, the perturbations were created by the DED [126]. It has been shown experimentally that the the RMP produced by the DED 3/1 mode enhances the runaway loss [20]. On the contrary, in [84] no clear effect of the applied perturbation fields on the RE suppression has been found. In the recent study [85], the IR image of the synchrotron radiation emitted by REs during the mitigated disruptions, show the filamentary structures caused either by the

external ergodization of the DED or by the internal ergodization (see Fig. 46 (A) for the normal recording mode, (B) for the subtraction mode). The structures reach deep into the runaway beam and lead to enhanced losses.

In case of the DED 6/2 operational mode, it has been found that, the runaway current drops with increasing perturbation current. The avalanche generation which depends on the runaway current also drops. The suppression of high energy REs can be achieved if the perturbation levels is sufficiently high. The reduction of the plateau length and the synchrotron radiation intensity have been observed. The current decay rate, in contrast, appears to be unaffected by the perturbations. Figure 47 shows the averaged RE current length for the different DED currents and the time of its application. As seen from Figure REs are strongly suppressed if the DED-field is applied before the disruption is triggered by the gas injection at $t = 2$ s. However, the complete runaway mitigation still cannot be achieved.

8 Mechanism of RE beam formation during disruptions

In this chapter we describe a new physical mechanism of formation of RE beams during plasma disruptions in tokamaks proposed in [127, 128]. It is based on the analysis of numerous experimental results, mainly obtained in the TEXTOR tokamak and the ideas of magnetic field stochasticity [47]. The mechanism explains many features of plasma disruptions accompanied by RE generations.

8.1 Main conjectures

It is believed that the plasma disruption starts with the excitation of MHD modes with low poloidal m and toroidal n numbers, ($m/n = 1/1, 2/1, 3/2, 5/2, \dots$) that lead to a large–scale magnetic stochasticity (see, e.g., [129, 53, 130, 131] and references therein). The heat and particle transports in the strongly chaotic magnetic field causes the fast temperature drop and ceases the plasma current. This process depends on the structure of the stochastic magnetic field which depends on the spectra of magnetic perturbations and on the safety factor profile $q(\rho)$. At certain conditions the stochastic magnetic field may not extend up to the central plasma region due to the creation of the outermost intact magnetic surface ρ_c. The electrons confined by this magnetic surface are accelerated by the toroidal electric field induced by the current decay from the outer plasma region, which leads to the formation of the RE beam. The initial RE current $I_{RE}^{(0)}$ is mainly determined by the pre-disruption plasma current distribution $I_p(\rho)$ confined by the outermost intact magnetic surface ρ_c, i.e., $I_{RE}^{(0)} \approx I_p(\rho_c)$.

The lifetime of the RE beam mainly depends on two effects: the outward drift of RE orbits induced by the toroidal electric field $\mathcal{E}_\varphi$ [51, 48] (see Sec.3.4) and the resonant interactions of REs with helical magnetic perturbations (see Sec. 4.6.2). The first one is responsible for the smooth decay of the RE current, while the second one cause the sudden RE losses. According to (3.13) the outward drift velocity v_{dr} is determined by $\mathcal{E}_\varphi$ and the RE current,

$$v_{dr} \propto \frac{\mathcal{E}_\varphi}{I_{RE}^{(0)}} \propto \frac{\mathcal{E}_\varphi}{\rho_c^2}. \tag{8.1}$$

The most stable of the RE beams are expected to form when the corresponding drift velocity is lowest and the low–order rational surfaces within the RE beam are absent or one.

Consider, for example, the pre-disruption plasma with a monotonic safety factor profile $q(\rho)$ with $q(0) < 1$. Then the *most stable RE beam can be formed when the outermost intact magnetic surface is located between magnetic surface* $q = 1$ *and the nearest low–order rational surfaces* $q = 5/4$ [or $q = 4/3$, ...]. It occurs at the sufficiently small amplitude of the $m/n = 1/1$ mode. There is only one rational magnetic surface $q = 1$ within the RE beam that is resonant to the large–scale magnetic perturbations, particularly, to the RMPs. Such RE beams are relatively stable since low–energetic REs (up to 10–15 MeV) are not destabilized due to absence of a large scale stochasticity. The loss of REs mainly occurs due to the outward drift of RE orbits and the stochastic instability of high–energetic REs due to the interactions of high–mode harmonics of the $m/n = 1/1$ mode of magnetic perturbations.

In the case of plasma disruptions with $q(0) > 1$ the intact magnetic surface ρ_c would be smaller while the toroidal electric field E_φ would be larger than in the ones with $q(0) < 1$. Due to the large outward drift velocity v_{dr} such RE beams would cease faster.

8.1.1 Generic structures of magnetic field during plasma disruption

The two possible distinct generic structures of a stochastic magnetic field before the current quench with the RE-free discharge and with the RE discharge are shown in Figs. 48 (a) and (b) by the Poincaré sections of magnetic field lines (see Appendix C detailed discussions). It is assumed that the perturbation magnetic field contains several low–mode number m/n MHD modes with equal amplitudes B_{mn}: (a) the amplitude B_{11} of the $m/n = 1/1$ mode is equal to others; (b) B_{11} is four times smaller than the amplitudes of other modes. As seen from Fig. 48 (a) for the large amplitude of the $(m/n = 1/1)$ mode the stochastic magnetic field extends up to the central plasma region destroying the separatrix of the $m = n = 1$ island. For the low–amplitude of the $(m/n = 1/1)$ mode shown in Fig. 48 (b) the stochastic magnetic field does not reach the $q = 1$ magnetic surface. The last intact drift surface (red curve) is located between the resonant surfaces $q = 1$ and $q = 5/4$ (blue curves).

The existence of an intact magnetic surface and its location depends on the radial profile of the safety factor and on the spectrum of magnetic perturbations. The latter sensitively depend on the plasma disruption conditions and vary unpredictably from one discharge to another during plasma disruptions. This makes RE formation process unpredictable and may explain a shot–to–shot variability of the parameters of RE beams.

One should note the recent experimental work on RE suppression in the ADITYA tokamak [86]. Particularly, it was shown that the toroidally lo-

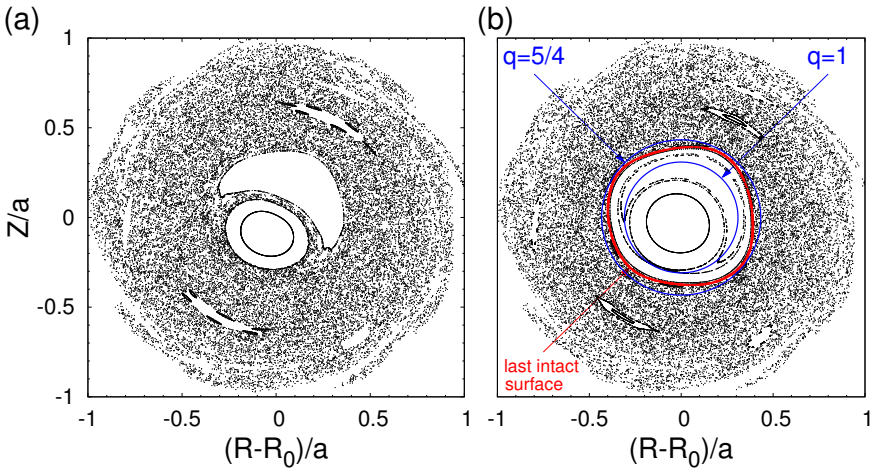

Fig. 48. Poincaré sections of magnetic field lines in a pre–disruption plasma caused by several m/n MHD modes, $(n = 1, 2, 3; m = 1, \dots 8)$: **(a)** all mode amplitudes $B_{mn} = 4 \times 10^{-3} B_0$ are equal; **(b)** the amplitude $B_{11} = 10^{-3} B_0$ of the $m/n = 1/1$ mode is four times smaller than other B_{mn}. Blue curves correspond to the magnetic surfaces $q = 1$ and $q = 5/4$, red curve corresponds to the last instact magnetic surface. The safety factor at the magnetic axis $q(0) = 0.8$ and at the plasma edge $q(a) = 4.7$.

calized external magnetic perturbation effective suppresses the formation of REs. Such a magnetic perturbation contains the predominant $n = 1$ toroidal mode and therefore it effective destroys all low–order rational magnetic surfaces and creates the stochastic zone extended up the plasma core like one shown in Fig. 48 (a).

8.1.2 Disruptions of plasmas with reversed magnetic shear

The role of the safety factor profile in the formation of RE beams can be pronounced during disruptions of plasmas with the reversed magnetic shear. In the plasmas with the non-monotonic radial profiles of the safety factor it has been observed an improved confinement of energy and particles due to the internal transport barrier located near the minimal value of the safety factor, i.e., near the shearless magnetic surface [132, 133]. During disruptions this magnetic surface acts as a robust magnetic barrier that separates a chaotic magnetic field formed in outer region from the penetration into the central plasma region. Electrons confined by the shearless magnetic surface can form a stable RE beam with a relatively large transversal size. The disruption experiments in the TFTR tokamak with the reversed magnetic shear indeed show the formation of a large RE beam with long confinement times [134].

Figure 49 (a) and (b) show the example of the non–monotonic radial profile of the safety factor $q(\rho)$ and the corresponding Poincaré section of stochastic magnetic field lines (More detailed description of this case is given in Appendix C). The intact magnetic surface located near the shearless magnetic surface (dashed curve), i.e. the magnetic surface with a minimal value of the safety factor $q(\rho)$, is not broken even at the relatively large magnetic perturbations. And it confines electrons in the central plasma region.

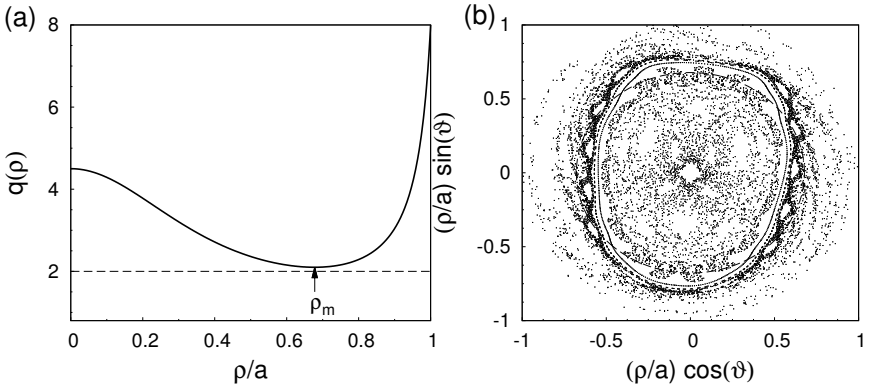

Fig. 49. (a) Radial profile of the safety factor $q(\rho)$ in the plasma with the reversed magnetic shear. **(b)** Poincaré section of magnetic field lines in a pre–disruption plasma caused by several MHD modes. Dashed curve corresponds to the shearless magnetic surface.

8.2 Experimental evidences

This conjecture on the mechanism of RE beam formation agrees with the important features of the experimental observations in the TEXTOR tokamak. In the experiments the plasma disruptions were triggered by gas injections (see, e.g., [21, 135, 24]): the disruptions with REs were triggered by argon (Ar) injection and the RE–free disruptions with Ne injection. The injection of these gases may finally give rise to different spectra of amplitudes of MHD modes. One can expect that the amplitude of the $m/n = 1/1$ MHD mode excited by the He/Ne injection is higher than in the case of Ar gas injection.

The plasma current decay in the current quench (CQ) and the RE plateau regimes for all discharges is well approximated by the linear function of time $I_p = I_{p0} + bt$, with the average CQ rate $b = \langle dI_p/dt \rangle$ as shown in Fig. 50 (a). The current decay rates $|\langle dI_p/dt \rangle|$ in the CQ stage and the RE plateau stage versus the initial RE current $I_{RE}^{(0)}$ for a number discharges are plotted Fig. 50

(b). The plausible radial profiles of $I_p(\rho)$ (A.4) and the corresponding safety factor $q(\rho)$ (A.6) are plotted for the two values of $q(0)$ in Fig. 51.

8.2.1 Existence of the finite interval of the initial RE currents $I_{RE}^{(0)}$

Since ρ_c is located between the magnetic surfaces ρ_1 and ρ_3 corresponding to $q(\rho_1) = 1$ and $q(\rho_3) = 4/3$, the RE current $I_{RE}^{(0)}$ should take values in the finite interval. This expectation is supported by the experimental values of the plasma current $I_{RE}^{(0)}$ as seen from Fig. 50 (a) and (b). These values of $I_{RE}^{(0)}$ also lie in the region between the resonance magnetic surfaces $q(\rho_1) = 1$ and $q(\rho_3) = 4/3$ [or $q(\rho_2) = 3/2$] as shown in Fig. 51 where the radial profile of the pre–disruption equilibrium plasma current $I_p(\rho)$ (curve 1) and the corresponding safety factor profile $q(\rho)$ (curve 2) are plotted.

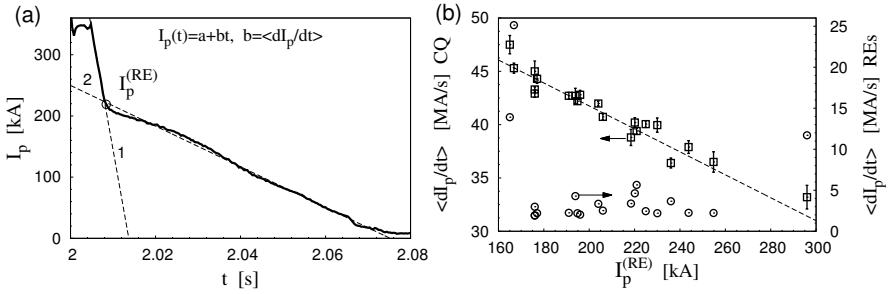

Fig. 50. (a) Typical time evolution of the plasma current with RE current. The average current decay rates $\langle dI_p/dt\rangle$ at the CQ and the RE plateau stages are determined by fitting with a linear function $I_p(t) = a + bt$. Symbol $\odot$ corresponds to the plasma current $I_{RE}^{(0)}$ at the initial stage of the RE plateau. **(b)** The decay rates $|\langle dI_p/dt\rangle|$ versus $I_{RE}^{(0)}$. Symbols $\boxdot$ correspond to the CQ rate (the left–hand side axis), and symbols $\odot$ correspond to the RE plateau (the right–hand side axis).

The average values of $\langle|dI_p/dt|\rangle$ for almost all discharges are confined in the interval (2.2, 5.6) MA/s, i.e., in one order lower than the current decay rate in the CQ stage. The values of $I_{RE}^{(0)}$ are in the range between 170 kA and 260 kA (see Fig. 50 (b)). These values of $\langle|dI_p/dt|\rangle$ and $I_{RE}^{(0)}$ are close to the ones observed in the similar experiments in the DIII-D tokamak (see, e.g., [136]).

As seen from Fig. 50 (a) there are untypical discharges with the highest and lowest values of $I_{RE}^{(0)}$ that correspond to ρ_c at the borders of region $\rho_1 < \rho < \rho_3$. For these discharges the CQ rates $\langle|dI_p/dt|\rangle$ take highest or lowest values. The RE current decay rates of these discharges take the highest values. They have the shortest duration time of RE currents. One expects that the presence of several low–order $m/n = 4/3$, $m/n = 3/2$, and $m/n = 1/1$

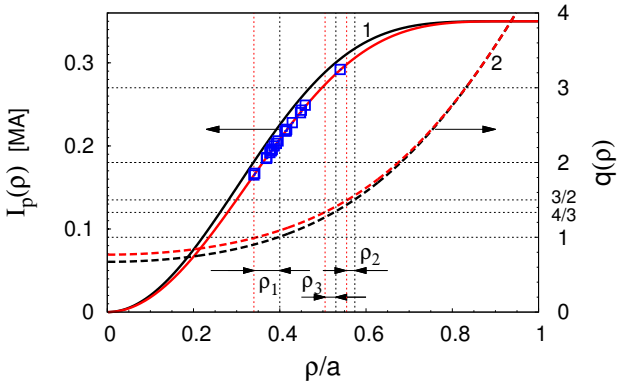

Fig. 51. Radial profile of the plasma current $I_p(\rho)$ (solid curves 1 on the left–hand side axis) and the corresponding safety factor profile $q(\rho)$ (dashed curves 2 on the right–hand side axis). The rectangular (blue) symbols ⊡ correspond to the experimentally measured values of $I_{RE}^{(0)}$ for several TEXTOR discharges. The plasma parameters are $I_p = 350$ kA, $B_0 = 2.4$ T, $R_0 = 1.75$ m, and $a = 0.46$ m. The values of $q(0)$ are 0.7 (dashed black curve) and 0.8 (dashed red curve), respectively. The radii ρ_1, ρ_2, and ρ_3 are the positions of the rational magnetic surfaces $q(\rho_1)$=1, $q(\rho_2)$=3/2, and $q(\rho_3)$=4/3, respectively.

resonant magnetic surfaces within the RE beam for the discharge with the highest $I_{RE}^{(0)}$ may lead to excitations of the corresponding MHD modes. The interactions of these modes may lead to the quick loss of REs due to the formation of a stochastic zone at the edge of the RE beam.

8.2.2 Dependence on the level of magnetic perturbations

The existence of the intact magnetic surface ρ_c between the $q = 1$ and the closest low–order rational $q = 5/4$ (or 4/3, ...) magnetic surfaces and its location depends on the spectrum of MHD modes B_{mn}. With increase of the amplitudes B_{mn} the radius ρ_c shrinks and it can be broken at the certain critical perturbation levels of B_{mn}. It leads to the total destruction of confinement of electrons and ions. This is in agreement with experimental observations of the existence of critical magnetic perturbations from which on runaway beams are not generated [135].

The shrinkage of ρ_c with increasing the magnetic perturbation B_{mn} leads to the decrease of the RE current $I_{RE}^{(0)}$ since $I_{RE}^{(0)} \approx I_p(\rho_c)$. On the other hand if one assumes that the plasma current decay is caused by the radial transport of particles in the stochastic magnetic field, the CQ rate dI_p/dt should be proportional to the square of the magnetic perturbation level ϵ_{MHD}, $|\langle dI_p/dt \rangle| \propto |B_{mn}|^2$. Therefore, one expects that to the higher values of $|\langle dI_p/dt \rangle|$ correspond the lower values of the RE current $I_{RE}^{(0)}$. This

expectation is in agreement with the experimental measured values of these quantities presented in Fig. 50 (b).

The formation of the RE beam inside the intact magnetic surface can be also confirmed by the spatial profiles of the synchrotron radiation of high–energy REs with energies exceeding 25 MeV. One observes that the radiation is localized within a finite radial extent in the central plasma region.

8.3 Estimations of thermal quench and current quench times

The strong radial transport along the stochastic magnetic field lines causes the losses of heat and plasma particles from the stochastic zone. The thermal quench (TQ) can be explained by the fact that the anomalously large heat transport in a stochastic magnetic field is mainly determined by the electron diffusion. The current quench (CQ) is determined by the particle transport in a stochastic magnetic field and has an ambipolar nature. Using the collisional test particle transport model in a stochastic magnetic field [137] we estimated the heat conductivity $\chi_r(\rho)$ and the ambipolar diffusion coefficient D_r of particles. These estimations are described in Appendix D.

For typical magnetic perturbations and pre-disruption plasma temperatures ($0.5 \div 1.0$ keV) the magnitude of $\chi_r(\rho)$ has the order of several 10^2 m^2/s. The characteristic heat diffusion time $\tau_H = a^2/2\chi_r$ is of the order of 10^{-4} s that agrees with the experimentally observed times. The quantitative analysis based on the numerical solution of the heat diffusion equation also gives similar values for τ_H.

The ambipolar particle transport in a stochastic magnetic field is strongly collisional due to the low plasma temperature (from 5 eV to 50 eV) after the TQ. At these plasma temperatures the corresponding diffusion time $\tau_p = a^2/D_r$ of particles changes from 1 s to 0.3 s. Since the diffusion coefficient $D_r \propto B_{mn}^2$ and therefore $\tau_p \propto B_{mn}^{-2}$, then τ_p can be reduced to one order smaller value for a three times larger perturbation than in Fig. 48 (see Table 1 in Appendix D where the results of calculations of D_r at the different plasma temperatures are listed). This timescale is still much longer than the experimental values. However, the collisional model does not takes into account the effect of the toroidal electric field. One expects that the acceleration of electrons and ions by the toroidal electric field increases the radial transport of particles. To include this effect in the collisional model one can assume that the effective temperature of the plasma is higher than the measured one. The particle diffusion time τ_p at the effective temperature 2 keV is about 8×10^{-3} s. This timescale gives the average current decay rate $dI_p/dt \approx I_p/\tau_p = 0.35/(8.0 \times 10^{-3}) \approx 44.0$ MA/s which is order of the experimental measured one given in Fig. 50 (b).

In general the transport of heat and particles in the presence of RMPs is a three–dimensional problem. Particularly, a stochastic magnetic field with

the topological structures like the ones in Figs. 48 leads to poloidally and toroidally localized heat and particle deposition patterns on the wall (see, e.g., [130]) similar to those in ergodic divertor tokamaks (see, e.g., [47]).

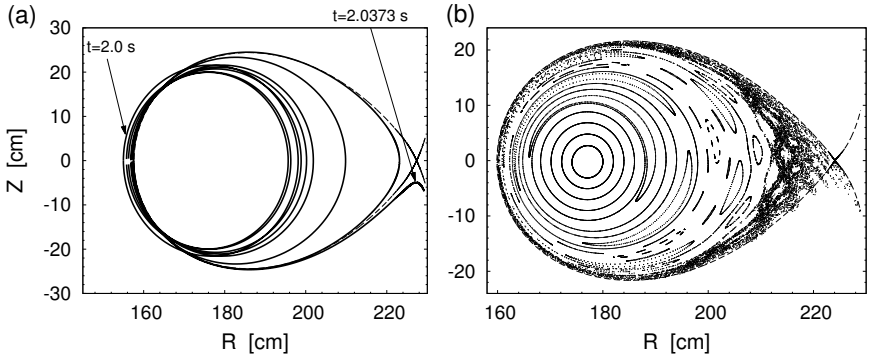

Fig. 52. **(a)** Evolution of RE orbit (solid curve) in the (R, Z)-plane for the TEXTOR discharge # 117527; dashed curve corresponds to the separatrix. **(b)** Poincaré section of RE orbit of energy E_k =20 MeV in the (R, Z)-plane in the presence of the $(m = 1, n = 1)$ MHD mode. The plasma current $I_{RE}^{(0)} = 100$ kA.

8.4 RE beam evolution

From the described scenario of plasma disruption it follows that a typical runaway beam current is localized inside the area enclosed by the last intact magnetic surface. In general the distribution of the current density j would depend not only on the radial coordinate ρ but also vary along the poloidal θ and the toroidal φ angles due to the presence of the $(m/n = 1/1)$ magnetic island. This agrees with the analysis of numerous disruptions in the JET tokamak [138]. One can assume that the radial profiles of the RE current density averaged along poloidal and toroidal angles are almost uniform. This gives the value of the safety factor at the beam axis $q(0)$ is less than unity. This assumption is supported by a number of experimental measurements of the current profile after the sawtooth crashes in the TEXTOR, the TFTR, and JET tokamaks [139, 140, 141, 142, 143, 144].

The toroidal electric field accelerates electrons to higher energies. As was shown in Sec. 3.4 with increasing electrons energy their orbits drifts outwardly and eventually hit the wall (see Fig. 5 and 6). This effect is illustrated in Fig. 52 (a) where the evolution of RE orbit in the toroidal electric field generated during plasma disruption is shown. It may be one of mechanisms of slow RE current decay. According to the formula (3.13) the outward drift velocity v_{dr} is of the order of a few m/s for typical discharges in TEXTOR.

The RE current decay rate dI_p/dt due to outward drift RE orbits can be roughly estimated as follows. This loss mechanism is mainly caused by the shrinkage of the beam radius a. The rate of such a shrinkage da/dt is of the order of the average outward velocity v_{dr}. Since $I_p \propto a^2$, we have $dI_p/dt \propto (2I_p/a)da/dt = (2I_p/a)v_{dr}$. For the typical values of $I_p \approx 0.2$ MA, $a \approx 0.2$ m, and $v_{dr} \sim 1$ m/s one has $dI_p/dt \approx 4$ MA/s. This estimation is in the order of the experimentally measured average decay rate of the runaway current plotted in Fig. 50 (b).

The effect of magnetic perturbation on RE beams depends on their safety factor profile q. The latter varies in the interval $[q(0) < 1, q(a)]$ with its edge value $q(a)$ less than 3/2 [or 4/3, 5/3]. Such a RE beam is relatively stable to the effect of magnetic perturbations. This is supported by the experimental fact described in Sec. 7.4.2 that the RE formation can be effectively suppressed if the DED magnetic perturbation is applied before the gas injection to initiate the plasma disruption. The magnetic perturbations applied after the gas injection does not suppress the REs or their effect is very weak. This is in agreement with the recent experiments in the TEXTOR tokamak [84].

As we have discussed in Sec. 4.6.2 the single $m/n = 1/1$ mode does not create the stochastic layer at the beam edge for REs with energies up to several MeVs since their drift surfaces are close to magnetic surfaces. With increasing the energy of electrons the drift surfaces strongly deviates from magnetic ones and thus creates the perturbation harmonics with higher mode numbers $m > 1$. The interactions of several resonance modes of perturbations may form the stochastic zone at the beam edge which leads to fast RE losses as illustrated in Fig. 52 (b). This process may explain the sudden RE current drop accompanied by magnetic activity and RE bursts observed in experiments (see, e.g., [8, 21]).

9 Summary

During the last several years we have carried out the series of theoretical and experimental studies of REs in the TEXTOR tokamak. The main results of these studies are the following:

1. Special attention has been paid to experimental investigations of high–energy REs ($\epsilon \geq 5$ MeV) in tokamak discharges. For this reason, three different types of probes have been developed and in addition, the synchrotron measurement technique has been applied.
   The *first and most important probe* is a scintillator probe, in which scintillators generate light from the incoming high–energy electrons. Each scintillating crystal is shielded by blocking material with different thickness. The optimum choice of the blocking material for the given case is iron. The whole assembly is shielded against light and low energy electrons by a 5 mm graphite housing. The probe allows an absolute energy resolved measurement of the REs.
   The *second probe* is a RE heat load probe, which gets intentionally destroyed by the incoming RE flux. Its active part consists of copper powder which is fixed by epoxy resin. The REs melt and evaporate part of the copper and the epoxy resin. From the damage, the radial decay length of the REs is deduced. Again this probe is shielded by a graphite housing.
   The *third probe* is a calorimeter in which the deposited energy of the REs from the electron approach direction is deposited in a thermally isolated graphite slab. The impact from the ion approach direction is shielded by a molybdenum slab. The temperatures of both layers are measured by thermocouples located at different positions. The graphite and molybdenum slabs are shielded from the low energy particles by 4 mm thick slabs of CFC.
2. On the one hand, the probes are mounted on a fast reciprocating drive and measure the runaways at the boundary. On the other hand, the synchrotron radiation technique measures the REs in the plasma core. The synchrotron radiation is a relativistic effect and is emitted only in forward direction of the electron flight. Therefore, the observation of the synchrotron radiation is a local measurement even though the optical path transits the whole plasma. The synchrotron radiation decays exponentially towards small wavelengths. As the IR camera is sensitive for

wavelengths between 3 μm and 5 μm, it detects only the REs with energies exceeding 25 MeV.

3. To support the experimental studies we have developed the rigorous theory of transport of REs in a background turbulent magnetic field and in the externally applied resonant magnetic perturbations. These theories are based on the Hamiltonian formulations of relativistic guiding–center motion. We employed the advanced methods of asymptotical analysis and symplectic integration (mapping) techniques to study the dynamics of REs and the structure of their regular and stochastic of motion. Particularly, we have found that the diffusion of high–energy REs in a turbulent magnetic field has a fractal nature with a reduced radial transport near the low–order rational drift surfaces.
   We have also investigated the drift motions of electron orbits induced by the toroidal electric field in tokamak. The general formula have been derived for the velocity of these drifts which describes the inward drift (the Ware pinch) as well as the outward drift of electron orbits. We have shown that the latter effect contributes significantly to the decay of RE current during a plasma disruption.
4. In the first part of the investigations, low density discharges ($n_e \leq 1 \times 10^{19} m^{-3}$), in which REs occur naturally, were analyzed. Here the main emphasis is to address basic physics questions namely measurements of the magnetic turbulence and its dependence of the toroidal magnetic field. The energy distribution function of REs in the range of few MeV to 30 MeV can be well described by an exponential function with an exponential decay rate of ~ 10 MeV. The diffusion coefficient of the RE is determined by the gradient of the runaways; it is of the order of a few times $10^{-3} m^2/s$. The runaway contend in the discharges increase with B_t while the loss decreases. Therefore the diffusion coefficient also decreases with B_t. For REs the diffusion is attributed to magnetic turbulence which ranges between 2.5 $\times 10^{-5}$ T at low B_t to 5×10^{-6} T at high B_t.
5. To analyze the transport of REs in a large–scale stochastic magnetic field we have used the $m/n = 6/2$ operational mode of the TEXTOR-DED. The diffusion coefficients were calculated taking also into account the background turbulent magnetic field and using the advanced symplectic mapping method. The diffusion eguations of REs with the diffusive loss term of a secondary RE generation and the RE acceleration terms are solved. The results of simulations were in a good agreement with the experimental measurements.
6. More important for practical applications than for basic physics are the efforts of measurements on REs during disruptions. The disruptions are triggered by a massive argon injection under nearly the same conditions. The measurements by the calorimetric probe shows that the efficiency of the conversion of magnetic energy into runaway energy decreases with the increasing plasma current. The runaway current increases with B_t,

consistent with the picture given at low densities that the diffusive losses are smaller there. The runaway edge structure is measured by the heat load probe. The damage is corresponding to a runaway beam of about 4×10^{16} runaway particles ($I_{RE} = 190$ kA) and a radial decay length of 5 mm $\leq$ 10 mm.

According to the observations of the synchrotron radiation, the loss of the runaways seem to be preferentially of diffusive nature. Only a few examples have been found where the loss of REs occurs along clear channels. This is consistent with the theoretical predictions of the evolution of REs in the presence of MHD modes. The resonant interaction of the high–energy REs explains the sudden RE losses accompanied by the spiky MHD signals which are often observed in the RE dominated current decay phase. A surprising observation is the fact that high energy runaways survive even when the plasma current is very low.

The removal of the REs generated during a disruption seems to be substantially more difficult than the removal of runaways in a low density discharge. The runaways seem to be robust against additional gas puffing and against resonant magnetic perturbations. To our experience the only recipe for eliminating the runaways is massive gas injection directly with the valve initiating the disruption or the excitation of a high amplitude tearing mode prior to the initiation of the disruption.

7. Finally based on the analysis of numerous experimental data obtained in the TEXTOR tokamak we have proposed a new possible mechanism of RE beam formation during the plasma disruption. The plasma disruption starts due to a large–scale magnetic stochasticity caused by nonlinearly excited of MHD modes with low (m, n) numbers ($m/n = 1/1, 2/1, 3/2, 5/2, \dots$). The RE beam is formed in the central plasma region confined by the intact magnetic surface. Its location depends on the safety factor profile $q(\rho)$ and the spectrum of MHD modes. In the cases of plasmas with the monotonic profile of $q(\rho)$ and at sufficiently small amplitude of the $m/n = 1/1$ mode the most stable RE beams are formed by the intact magnetic surface located between the magnetic surface $q = 1$ and the closest low–order rational surface $q = m/n > 1$ ($q = 5/4$, $q = 4/3$, or $q = 3/2$).

   This mechanism reproduces well the essential features of the measurements. Particularly, the TQ and the CQ are determined by the strong electron diffusion and ambipolar transport of particles in a stochastic magnetic field, respectively. The slow decay of the RE current is due to the outward drift of RE orbits induced by a toroidal electric field, and the spiky quick decay of REs is due to resonant interaction of high–energy REs with the $m/n = 1/1$ MHD mode. The effect of external resonant magnetic perturbations on low-energy electrons (up to 5-10 MeV) is weak and does not cause their loss.

A Models of equilibrium magnetic field

In this appendix we give a brief description of the analytical model of an equilibrium plasma with a circular cross-section which has been used in the main text to study the dynamics of REs in a toroidal plasmas. More detailed description can be found in [53] (see also [47]).

In a cylindrical plasma the safety factor profile can be found by the density profile of the toroidal plasma current $j(\rho)$. The poloidal magnetic field B_θ is determined by according to the Ampère's law

$$B_\theta(R,Z) = \frac{\mu_o I(\rho)}{2\pi\rho} = \frac{\mu_o}{\rho}\int_0^r j(\rho')\rho' d\rho',$$

where $I(\rho)$ is the current flowing inside the magnetic surface of radius ρ. The safety factor $q(\rho)$ in the cylindrical geometry is defined as

$$q_{cyl}(\rho) = \frac{\rho B_0}{R B_\theta} = \frac{2\pi\rho^2 B_0}{\mu_o R_0 I(\rho)}. \tag{A.1}$$

The value of the safety factor at the plasma edge $\rho = a$ is determined by the total plasma current I_p,

$$q_a = q_{cyl}(a) = \frac{2\pi a^2 B_0}{\mu_o R_0 I_p}. \tag{A.2}$$

Consider the model plasma current given by the density

$$j(\rho) = \begin{cases} \dfrac{I_p(\nu+1)}{\pi a^2}\left(1-\rho^2/a^2\right)^\nu, & \text{for } \rho \le a, \\ 0, & \text{for } \rho > a, \end{cases} \tag{A.3}$$

where ν in the constant parameter. Then

$$I(\rho) = \begin{cases} I_p\left[1-\left(1-\rho^2/a^2\right)^{\nu+1}\right], & \text{for } \rho \le a, \\ I_p, & \text{for } \rho > a. \end{cases} \tag{A.4}$$

The safety factor $q_{cyl}(r)$ corresponding to this plasma current distribution is given by

$$q_{cyl}(\rho) = \begin{cases} q_a \dfrac{\rho^2/a^2}{1-(1-\rho^2/a^2)^{\nu+1}}, & \text{for } \rho \le a, \\ q_a \rho^2/a^2, & \text{for } \rho > a. \end{cases} \tag{A.5}$$

The value of the safety factor at the magnetic axis $q(0)$ is determined by q_a and ν: $q(0) = q_a/(\nu+1)$.

The toroidal corrections to the safety factor can be also found in the limit of large aspect ratio $R/r \gg 1$. The expansion of the safety factor in a series of powers $\varepsilon = \rho/R_p(\rho)$ is given by (see, [145, 57]),

$$q(\rho) = q_{cyl}(\rho)\frac{R_0^2}{R_p^2(\rho)}\left(1+\frac{1}{2}a_2\varepsilon^2+\frac{3}{8}a_4\varepsilon^4\right)+O(\varepsilon^8), \tag{A.6}$$

where $q_{cyl}(\rho)$ is the safety factor in the cylindrical geometry (A.1). The coefficients a_m are polynomial functions of the plasma parameter $\Lambda = \beta_{pol} + l_i/2 - 1$:

$$a_m = (-1)^m \sum_{k=0}^{m} (m-k+1)\,\Lambda^k. \tag{A.7}$$

Here l_i is the plasma inductance.

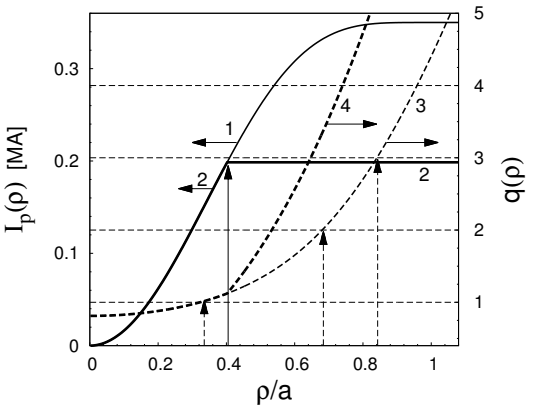

Fig. 53. Radial profiles of the plasma current $I_p(\rho)$ (A.4) (solid curve 1 on the left hand side axis) and the post–disruption current $I_{RE}(\rho)$ (solid curve 2 on the left hand side axis) (A.8), the corresponding safety factor profiles $q(\rho)$ (A.6) (dashed curves 3 and 4 on the right hand side axis). The plasma parameters are $I_p = 350$ kA, $B_0 = 2.2$ T, $R_0 = 1.75$ m, $a = 0.46$ m. The values of $q(0) = 0.8$.

The described model of the equilibrium plasma can be used to model the initial stage of the post–disruption plasma with REs. Let $I_{RE}^{(0)}$ be the total current of the plasma just after the current quench. Assume that the minor radius of the post–disruption current is b. The radial profiles of the current $I_{RE}(\rho)$ flowing inside the flux surface of radius ρ can be approximated as

$$I_{RE}(\rho) = \begin{cases} I_p(\rho), & \text{for } \rho \le b, \\ I_{RE}^{(0)}, & \text{for } \rho > b, \end{cases} \tag{A.8}$$

where $I_p(\rho)$ is the corresponding current of the pre–disruption plasma. The radius b is determined by $I_p(b) = I_{RE}^{(0)}$. The safety factor of the post–disruption plasma is determined by the formula similar to (A.6), (A.1) where $I(\rho)$ is replaced by $I_{RE}(\rho)$.

Figure 53 shows the typical example of the pre–disruption plasma current profiles $I(\rho)$ (A.4) (black solid curve 1) and the corresponding safety factor profile $q(\rho)$ (black dashed curve 3 on the right–hand side axis). In this Figure it is also plotted a possible profile of the post–disruption current $I_{RE}(\rho)$ (A.8) which may lead to the formation of RE beam (blue solid curve 2), and the corresponding safety factor profile $q(\rho)$. The full pre–disruption plasma current is taken equal to $I_p = 0.35$ MA, and the full post–disruption plasma current is $I_{RE}^{(0)} = 0.2$ MA. The value of the safety factor at the magnetic axis is taken $q(0) = 0.8$. The vertical dashed arrows show the positions of the rational magnetic surfaces ρ_m, $q(\rho_m) = m, m = 1, 2, 3$.

B Models of magnetic perturbations

In this appendix the analytical models of magnetic perturbations induced by MHD modes and the DED coils of the TEXTOR tokamak are presented. The detailed description of the TEXTOR-DED are given in [126] and Appendix A in [47].

B.1 Model of MHD modes

The magnetic perturbations due to the MHD modes can be described by the vector potential $A_\varphi^{(1)}(R, Z, \varphi, t)$. We present as sum

$$A_\varphi^{(1)}(R, Z,\varphi, t) = -\frac{B_0 R_0^2}{R} \sum_{mn} m^{-1} b_{mn}(\psi) \cos\left(m\vartheta_M - n\varphi + \Omega_{mn} t\right), \quad \text{(B.1)}$$

where Ω_{mn} is the frequency of the $(m, n)-$th mode and χ_{mn} is its phase. The quantity $b_{mn}(\psi)$ describes the normalized to B_0 amplitude and radial profile of the $(m, n)-$ mode. In (B.1) ϑ_M is the poloidal angle in which the field lines are linear functions of the toroidal angle φ: $\vartheta_M = \varphi/q(\psi) + \vartheta_0$.

The perturbation poloidal flux $\psi_\varphi^{(1)} = -RA_\varphi^{(1)}/B_0 R_0^2$ is given by

$$\psi_\varphi^{(1)}(R, Z, \varphi, t) = \sum_{mn} \epsilon_{mn} U_{mn}(\psi) \cos\left(m\vartheta_M - n\varphi + \omega_{mn} t + \chi_{mn}\right), \quad \text{(B.2)}$$

where $U_{mn}(\psi) = b_{mn}(\psi)/m b_{mn}(\psi_{mn})$ and ϵ_{mn} stands for the dimensionless perturbation parameter defined as

$$\epsilon_{mn} = |b_{mn}(\psi_{mn})| = |B_{mn}/B_0|. \quad \text{(B.3)}$$

The quantity $B_{mn} = b_{mn}(\psi_{mn})/B_0$ is the amplitude of $(m, n)-$ MHD mode at the rational magnetic surface ψ_{mn}, $q(\psi_{mn}) = m/n$. For example, for $\epsilon_{mn} = 7.0 \times 10^{-5}$ and B_0 =2.5 T we have $B_{mn} = 1.75 \times 10^{-4}$ T= 1.75 G.

Now we model the radial profiles of $U_{mn}(\psi)$ as a function of the normalized toroidal flux $\psi_t = \rho^2/a^2$. The main requirement is that the magnetic perturbations $U_{mn}(\psi_t)$ should go to zero at the magnetic axis $\psi_t = 0$ (or $\rho = 0$), i.e., $U_{mn}(\psi_t = 0) = 0$. As we will see below the structure of magnetic field

lines in the presence of magnetic perturbations is mainly determined by the amplitudes of modes $U_{mn}(\psi_t)$ at the resonant magnetic surfaces $\psi_t = \psi_{mn}$, it is less sensitive to the radial profiles of $U_{mn}(\psi_t)$, i.e., on the form of dependence of $U_{mn}(\psi_t)$ on ψ_t. Below we consider two models for the amplitudes $U_{mn}(\psi_t)$ satisfying the similar condition at the magnetic axis but having different radial profiles.

The first simple model is given by

$$U_{mn}(\psi_t) = \frac{1}{m}\left(1 - e^{-\psi_t/\Delta}\right), \tag{B.4}$$

which is determined by only one parameter Δ.

The several realistic models for the MHD modes have been proposed in literature (see, e.g., [146] and references therein). Below we use the model given in Ref. [147] (Eq. (9)) which has been reconstructed from ECE measurements in the ASDEX tokamak. We rewrite it in the form

$$U_{mn}(\psi_t) = \frac{1}{m}\begin{cases} \dfrac{1}{1-\beta}\left[1 - \beta\left(\bar{\psi}_t\right)^{1/2}\right]\left(\bar{\psi}_t\right)^{m/2}, \\ \qquad\qquad \text{for } \bar{\psi}_t \le 1, \\ \left[1 - \delta + \delta\left(\bar{\psi}_t\right)^{1/2}\right]\left(\bar{\psi}_t\right)^{-(m+1)/2}, \\ \qquad\qquad \text{for } \bar{\psi}_t > 1, \end{cases} \tag{B.5}$$

where $\bar{\psi}_t = \psi_t/\psi_{mn}$. In this form the profiles $mU_{mn}(\psi_t)$ takes a unit value at the resonant magnetic surface $\psi_t = \psi_{mn}$. The formula (B.5) depends on the parameters β and δ unlike the original one which depends on the three parameters. Then the amplitude of modes is given by the dimensionless perturbation parameters ϵ_{mn}.

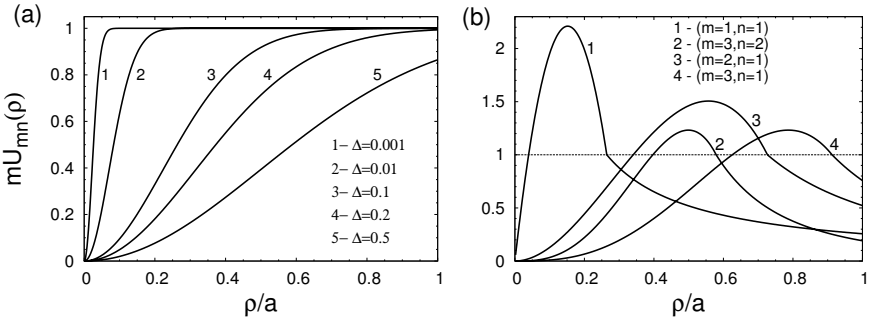

Fig. 54. Radial profiles of perturbation modes mU_{mn}: **(a)** corresponds to the profile (B.4); **(b)** corresponds to (B.5) with the parameters: $\alpha = 0.04$, $\beta = 0.87$, $\gamma = 0.005$, $\delta = 0.9615$. The radial positions $\rho_{mn} = a\sqrt{\psi_{mn}}$ correspond to the resonant surfaces $q(\psi_{mn}) = m/n$ for the safety factor (A.5) with $q_0 = 0.9$ and $q_a = 3.6$.

Figure 54 (a) and (b) show the profiles of $mU_{mn}(\psi_t)$ for the models (B.4) and (B.5), respectively, at the different values of Δ.

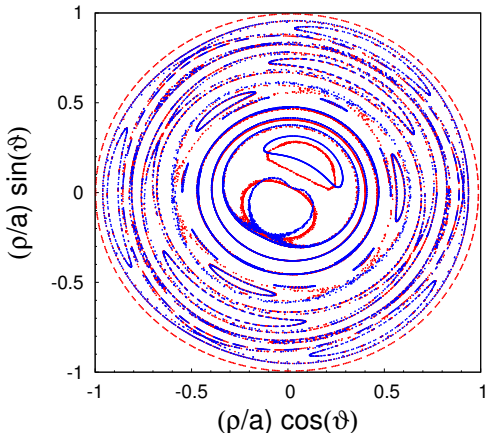

Fig. 55. Poincaré sections for the two different radial profiles of the MHD modes: blue dots corresponds (B.4) (see also Fig. 54 (a)); red dots corresponds to (B.5) (see also Fig. 54 (b)). The parameters: $\Delta = 0.001$, $\epsilon_{mn} = 2 \times 10^{-3}$ ($n = 1, 2$, $m = 1 - 4$), $q_0 = 0.9$ and $q_a = 3.6$.

The structure of field lines are mainly determined by the values of mode amplitudes U_{mn} at the resonant surfaces $\psi_t = \psi_{mn}$ rather then their radial profiles. It is illustrated in Fig. 55 by plotting Poincaré sections of field lines for the two different radial profiles of $U_{mn}(\psi_t)$ given by (B.4) and (B.5) (see Fig. 54 (a), (b)).

The structure of majority magnetic islands is less sensitive to the radial profiles of MHD modes. It is related with the fact in the pendulum approximation the form of the nonlinear resonance created by the MHD modes is mainly determined by the values of its amplitude $U_{mn}(\psi_t)$ at the resonant surfaces $\psi_t = \psi_{mn}$ (see, for example, Sec. 8.1 in [47]). Only the structure of the mode $n = 1, m = 1$ depends on the radial profile of $U_{mn}(\psi_t)$, especially at the region close to the magnetic axis. But the outer region of the island is less dependent on the profile of $U_{mn}(\psi_t)$.

B.2 Model of the DED magnetic perturbations

The TEXTOR tokamak has been equipped with the DED which consists mainly of 16 helically wound coils at the high field side of the torus plus two compensation coils. The coils follow the magnetic field lines of the $q = 3$ surface but can be interconnected in different ways. One can switch in parallel either each two neighboring coils, or four or eight and apply a DC current to the coils. The sketch of the DED coil configuration in the poloidal section is shown in Fig. 56.

The magnetic field created by the system of DED coils can be approximated by the toroidal component of the vector potential,

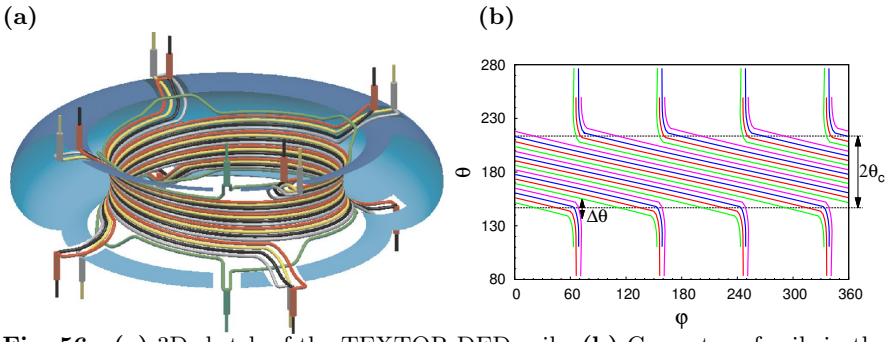

Fig. 56. **(a)** 3D-sketch of the TEXTOR-DED coils; **(b)** Geometry of coils in the (φ, θ)–plane.

$$\psi_{\varphi}^{(1)}(R, Z, \varphi) = \epsilon_{ded} \sum_{m} m^{-1} b_{mn}(r) \cos\left(m\theta + n\varphi + \phi_n - \Omega t\right), \tag{B.6}$$

where

$$\epsilon_{ded} = \frac{B_c}{B_0} = \frac{\mu_o m_0 I_{ded}}{\pi r_c B_0} \tag{B.7}$$

is the dimensionless perturbation parameter similar to ϵ_{MHD} (B.3). The coefficient b_{mn} determined by the geometrical configuration of coils is given by

$$b_{mn}(r) = \iota_n \sqrt{\frac{R_0}{R}} \frac{r_c g_{mn} R}{R_0^2} \left(\frac{r}{r_c}\right)^{|m|},$$
$$g_{mn} = (-1)^m \frac{\sin[x_{mn}\theta_c]}{x_{mn}\pi} \frac{\sin[x_{mn}\Delta\theta/2]}{x_{mn}\Delta\theta/2}, \qquad x_{mn} = m + \frac{nm_0}{4}. \tag{B.8}$$

It describes the poloidal mode spectrum at the given toroidal mode n. In Eq. (B.7) the quantity $B_c = \mu_0 m_0 I_{ded}/\pi r_c$ is the characteristic magnitude of the DED magnetic field, I_{ded} is the DED current, the constant m_0 determines the central poloidal mode number $nm_0/4$. The geometrical parameters: r_c is the minor radius of the DED coils, $2\theta_c$ is the average poloidal width of the coil set, $\Delta\theta$ is the angular measure of deviation of coils from the average locations shown in Fig. 56 (b) by dashed lines. Finally Ω is the rotation frequency of the perturbation field.

In (B.6) (r, θ, φ) are the quasi-toroidal coordinates related to the cylindrical coordinates R, Z as $r = \sqrt{(R - R_o)^2 + Z^2}$ and $\theta = \arctan(Z/[R - R_0])$. In a toroidal system the angle θ does not coincide with the poloidal ϑ.

The phases ϕ_n and the factor ι_n in Eq. (B.6) are determined by the coil configuration. For the particular configuration they given by

$$\phi_n = \frac{m_0 n}{4}(\pi - \theta_0) - \tilde{\phi}_n + \frac{\pi}{2}, \tag{B.9}$$

n	$\tilde{\phi}_n$	ι_n
1	$3\pi/16$	$\sin(\pi/4)/[4\sin(\pi/16)]$
2	$3\pi/8$	$1/[2\sin(\pi/8)]$
4	$5\pi/4$	$\sqrt{2}$

Table 1. Coefficients ϕ_h and ι_n for the different mode numbers n.

where θ_0 is a poloidal angle of the first coil at the section $\varphi = 0$. The coefficients $\tilde{\phi}_n$ and ι_n for the different values of$n$ are given in Table 1. The parameters r_c, θ_c, θ_0, $\Delta\theta$, and m_0 are determined by the geometry of coil configuration, and take fixed values, $r_c = 0.5325$ m, $\theta_c = 35.49°$, $\theta_0 = 169.35°$, $\Delta\theta = 17.745°$, and $m_0 \approx 20$.

The toroidal mode number n takes the value $n = 4$ for the so–called $m/n = 12/4$ operational mode, $n = 2$ for the $m/n = 6/2$ mode, and $n = 1$ for the $m/n = 3/1$ mode, respectively.

The radial decay of the radial component of the perturbation field $B_r = -r^{-1}\partial A_\varphi/\partial\theta$ in these modes is proportional to $(r/r_c)^{nm_0/4}$. The field of the $n = 4$ mode decays radially rather fast ($B_r \propto (r/a)^{m_0}$) and has only a shallow penetration while that of the mode $n = 1$ ($B_r \propto (r/a)^{m_0/4}$) penetrates nearly fully into the plasma [1]

This model of the DED fields well describes the qualitative and quantitative features of heat deposition patterns observed in the TEXTOR–DED experiments [148, 126].

[1] It is true only a vacuum approximation when plasma response to a relatively rotating perturbation field is neglected. In the latter case the RMP field does not penetrate into plasma fully due to the formation of shielding current at resonant magnetic surfaces (see a review by T.E. Evans [80] and references therein).

C Generic structures of a stochastic magnetic field during plasma disruptions

As was discussed in Sec. 8.1 that the plasma disruption is caused by the large–scale magnetic stochasticity created by the interactions of nonlinearly excited low-order (m, n) MHD modes: $(1/1, 2/1, 3/2, 4/3, \dots)$. In this section we explore possible generic structures of magnetic field during plasma disruptions. For this study we use the models of magnetic field described in Sec. B.1.

First we consider structures of magnetic field during plasma disruptions corresponding to the plasma with a monotonic radial profile of the safety factor $q(\psi_t)$ (A.6) shown in Fig. 53. Figures 57 (a)–(d) shows Poincaré sections of field lines in the presence several low–order MHD modes and with the different amplitudes ϵ_{11} of the $(m = 1, n = 1)$ mode. The interaction of these modes leads to the strong chaotic behavior of field lines. At the small amplitudes of the $(m = 1, n = 1)$ mode, shown in Fig. 57 (a), the chaotic field lines are formed only in outer region. The central plasma region is separated from the chaotic region by the *magnetic transport barrier* formed between the magnetic surface $q = 1$ and $q = 5/3$. The stochastic layer formed near the separatrix of the magnetic island $(m = 1, n = 1)$ is negligible small. With increasing ϵ_{11} the magnetic transport barrier moves toward toward the plasma center and the width of the stochastic layer of the the magnetic island $(m = 1, n = 1)$ grows as shown in Fig. 57 (b). Starting from the certain level of ϵ_{11} the transport barrier disappears and the stochastic layer of the island $(m = 1, n = 1)$ joins the outer chaotic zone (Fig. 57 (c)). The further increase of ϵ_{11} shrinks the stability region of of the island $(m = 1, n = 1)$ (Fig. 57 (d)).

Now we consider the plasmas with a reversed magnetic shear, i.e., with a *non-monotonic radial profile* of the safety factor $q(\psi_t)$. The formation of the stochastic zone in this case is different from the case with the monotonic safety factor profile. The magnetic transport barrier is formed near the so–called *shearless magnetic surface* where $q(\psi_t)$ takes minimal value. Such a magnetic surface is relatively stable even to large magnetic perturbations. The latter does not shrink the shearless magnetic surface but only deforms it [1].

[1] The detailed description such systems known as *non-twist systems* and references can be found in monographs by [57, 47].

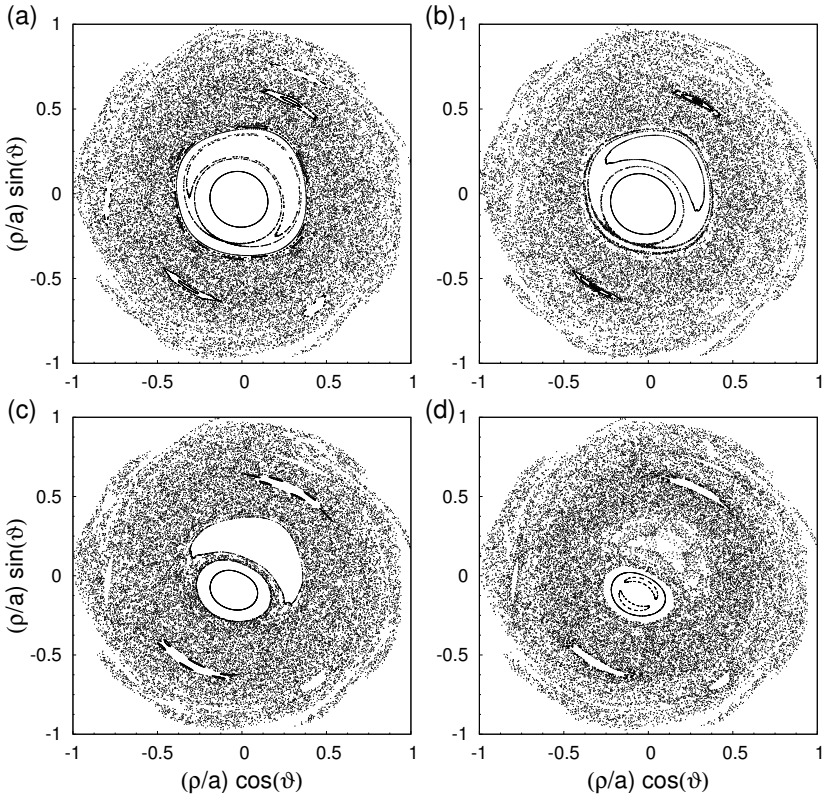

Fig. 57. Poincaré sections of field lines in a pre–disruption plasma caused by a several MHD modes with the different amplitudes of the $(m = 1, n = 1)$ mode: **(a)** $\epsilon_{11} = 10^{-3}$; **(b)** $\epsilon_{11} = 2 \times 10^{-3}$; **(c)** $\epsilon_{11} = 4 \times 10^{-3}$; **(d)** $\epsilon_{11} = 8 \times 10^{-3}$. The amplitudes of all other modes are $\epsilon_{mn} = 4 \times 10^{-3}$ $(n = 1 - 3,\ m = 1 - 11)$. The safety factor at the magnetic axis is $q(0) = 0.8$ and at the plasma edge $q_a = 4.7$.

To illustrate this we consider the plasma with the following safety factor profile

$$q(\rho) = \frac{q_m}{1 - b(\rho^2 - \rho_m^2)^2}, \tag{C.1}$$

shown in Fig. 58 (a). Here q_m is a minimal value of $q(\rho)$, ρ_m is the shearless magnetic surface, b is constant. The parameters ρ_m and b can be expressed through the values of the safety factor at the magnetic axis $q(0)$, the plasma edge $q(a)$, and q_m.

Poincaré sections of magnetic field lines are plotted in Fig. 58 (b)-(d) for the different amplitudes of magnetic perturbations ϵ_{mn} with the radial profiles (B.4). As seen the magnetic transport barrier (a red curve) located

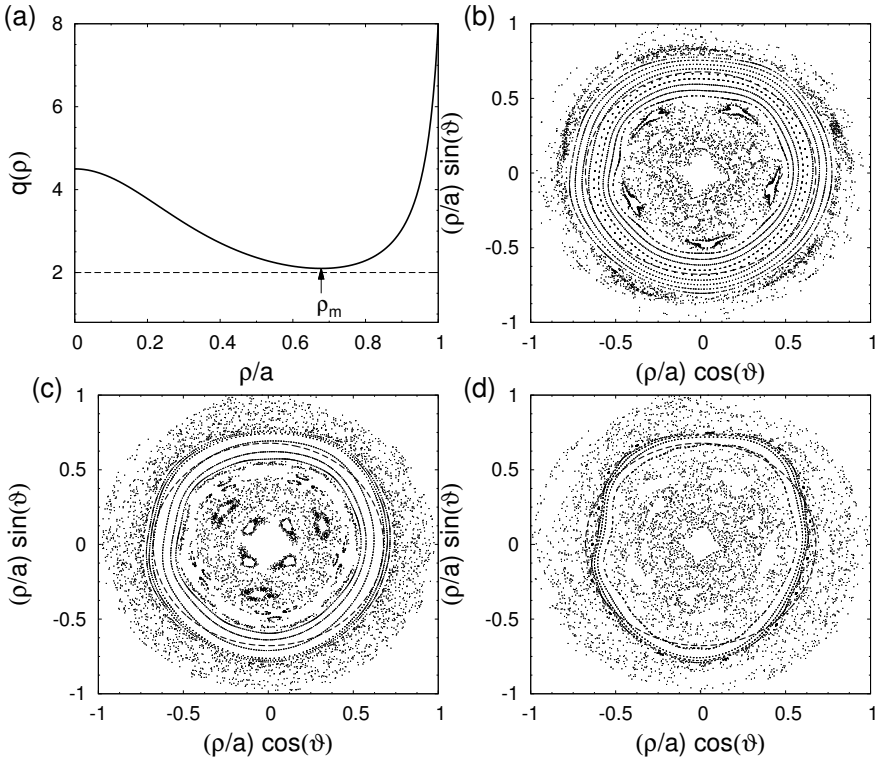

Fig. 58. The same as in Fig. 57 but for the plasma with the reverse magnetic shear. **(a)** the safety factor profile $q(\rho)$; The amplitudes of all MHD modes are equal: **(b)** $\epsilon_{mn} = 10^{-3}$; **(c)** $\epsilon_{mn} = 5 \times 10^{-3}$; **(d)** $\epsilon_{mn} = 10^{-2}$; The safety factor at the magnetic axis is $q(0) = 4.5$, the minimal value $q_m = 2.1$, and at the plasma edge $q_a = 8.0$. The parameter Δ in (B.4) is taken equal to 0.5. Dashed curve corresponds to the unperturbed shearless magnetic surface $\rho = \rho_m$.

near the shearless magnetic surface $\rho = \rho_m$ does not shrink with the increase of perturbations.

In the cases shown in Figs. 57 (a), (b) and Fig. 58 (b)-(d) the central region of plasma is confined and the radial transport of particles there is much small than in the chaotic region. The acceleration of electrons in this confined region by the toroidal electric field may lead to the formation of RE beams.

D Collisional heat and particle transport in a stochastic magnetic field

The transport of heat and charged particles in a stochastic magnetic field has been studied since early 1970s in the numerous works (see [137], Sec. 10.4 in [47] and Sec. 9.8 in [149] for references). In general this problem has a three–dimensional nature because of the system's asymmetry along poloidal and toroidal directions in the presence of magnetic perturbations ([150, 151, 152] and references therein). However, the problem can be simplified when we are interested only in the radial transport averaged over poloidal and toroidal angles. In this case the heat transport along the radial coordinate can be characterized by only the radial heat conductivity coefficient χ_r which in turn is determined by the radial diffusion coefficient D_r of electrons.

Below we calculate the diffusion coefficient D_r in a stochastic magnetic field during the plasma disruption. For this purpose we use the collisional test particle transport model described in [137, 47] (see also [153]). In this model a collisional particle motion in the presence of magnetic perturbations is considered as a random walk process along field lines and random jumps across magnetic surfaces.

The numerical procedure of this process is carried out in a following way: a particle moves freely along the field line with a step l after which it collides with other particle with the probability p, $(0 < p < 1)$. After the collision it changes the direction of motion to the opposite one being simultaneously displaced to the distance $\delta\rho$ across a field line. The probability p is determined by the mean free path λ_{mfp}: $p = l/(l + \lambda_{mfp})$, while the displacement $\delta\rho$ is determined by the perpendicular diffusion coefficient $\chi_\perp$: $\delta\rho = \sqrt{2\chi_\perp/pv_\parallel}$, where $v_\parallel$ is a parallel velocity of a particle. The mean free path depends of the plasma temperature T_e and electrons,

$$\lambda_{mfp} = 8.5 \times 10^{21} T_e^2/n_e, \ [\mathrm{m}],$$

where the electron temperature T_e [in keV] and the density n_e [in m^{-3}]. One should note that the temperature and the density are local functions of the radial coordinate ρ: $T_e = T_e(\rho)$ and $n_e = n_e(\rho)$. The parallel velocity $v_\parallel$ can be taken equal to the electron thermal velocity $v_{T_e} = \sqrt{kT_e/m_e} = 1.33 \times 10^7 \ T_e^{1/2}$ m/s, where k is the Boltzmann's constant.

The calculations are performed by integrating the field line equations (4.6) using the forward and the backward mapping procedures described in [137,

57, 47]. The local diffusion coefficients D_r are found by fitting the dependence of the second moment $\langle(\Delta\rho)^2\rangle$ on time t by a linear function $2D_r t$ at the initial growth range of t. Figure 59 shows an example of the dependence of the local diffusion coefficient D_r of electrons on the local temperature T_e at the magnetic surface $\rho = 0.71a$ in a stochastic magnetic field shown in Fig. 57 (b).

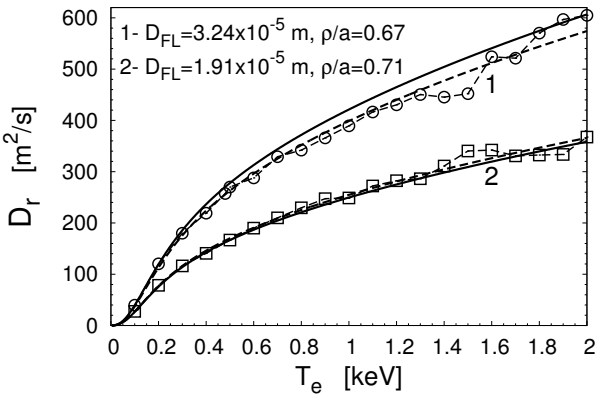

Fig. 59. Dependences of the local radial diffusion coefficients D_r on the electron temperature T_e at the magnetic surfaces $\rho = 0.5a$ (curves 1) and $\rho = 0.71a$ (curves 2). The plasma density $n = 2\times10^{19}$ m^{-3}. Symbols $\odot$, $\boxdot$ correspond to the numerical calculated D_r, solid curves correspond to the empirical formula (D.1) for D_r, and dashed curves correspond to the formula $D_r = \alpha\sqrt{T}/(1+\beta/T^2)$ with the fitted coefficients α and β. The non–zero MHD mode amplitudes $b_{mn} = (b_{11}, b_{21}, b_{32}, b_{52}) = (1,1,1,1)\times\epsilon$, where the perturbation parameter is $\epsilon = 1.5\times10^{-4}$. The plasma current $I_p = 350$ kA, the toroidal field $B_t = 2.5$ T, and the safety factor at the magnetic axis is $q(0) = 0.8$.

As was shown in [137] the collisional diffusion coefficient D_r can be quite well described by the empirical formula

$$\chi_r(\rho, T_e) = \frac{v_\parallel D_{FL}(\rho)}{1 + L_c/\lambda_{mfp}}, \tag{D.1}$$

determined only by a few plasma parameters: the mean free path λ_{mfp}, the thermal velocity v_{T_e}, the radial diffusion coefficient of field lines, D_{FL}, and the characteristic length L_c. The latter is an empirical parameter which has an order of the connection length $\pi q R_0$. As seen from Fig. 59 the empirical formula (red curve) well describes the temperature dependence of D_r.

The particle transport in a stochastic magnetic field can be also treated in a similar way. However, because of the ambipolarity of a particle transport instead of the thermal velocities of electrons v_{T_e} and ions v_{T_i} =

$\sqrt{kT_i/m_i}$ in the test particle simulations one should use the sound speed $c_s = \sqrt{k(T_e + \gamma_i T_i)/m_i}$ where T_i is the ion temperature, m_i is the ion mass, and γ_i is the adiabatic index. This condition comes from the fact that the loss rates of electrons and ions are equal.

T_i [keV]	D_r [m^2/s]	$\tau_p = a^2/2D_r$ [s]
0.005	0.0986057	1.072
0.050	0.386249	2.739×10^{-1}
0.100	1.01251	1.045×10^{-1}
0.500	6.46228	1.637×10^{-2}
1.000	9.51915	1.111×10^{-2}
2.000	13.1030	8.074×10^{-3}
4.000	17.8366	5.932×10^{-3}
5.000	23.7424	4.456×10^{-3}
10.00	27.0265	3.915×10^{-3}

Table 1. Ambipolar diffusion coefficients D_r of particles and the diffusion times $\tau_p = a^2/2D_r$ from the stochastic zone at the different effective plasma temperatures. The plasma radius $a = 0.46$ m.

In Table 1 we have listed the values of the ambipolar diffusion coefficients D_r and the characteristic diffusion times $\tau_p = a^2/2D_r$ of particles from the stochastic zone at the different plasma temperatures $T_e = T_i$.

References

1. H. Dreicer. Electron and ion runaway in a fully ionized gas. *Phys. Rev.*, **115**, 238–249 (1959).
2. H. Dreicer. Electron and ion runaway in a fully ionized gas. II. *Phys. Rev.*, **117**, 329–342 (1960).
3. J.W. Connor and R.J. Hastie. Relativistic limitations on runaway electrons. *Nucl. Fusion*, **15**, 415 (1975).
4. K. H. Finken, J. G. Watkins, D. Rüsbuldt, W. J. Corbett, K. H. Dippel, D. M. Goebel, and R. A. Moyer. Observation of synchrotron radiation from tokamak runaway electrons in TEXTOR. *Nucl. Fusion*, **30**, 859 (1990).
5. R. Nygren, T. Lutz, D. Walsh, G. Martin, M. Chatelier, T. Loarer, and D. Guilhem. Runaway electron damage to the Tore Supra phase III outboard pump limiter. *J. Nucl. Mater.*, **241-243**, 522–527 (1997).
6. A.N. James, M.E. Austin, N. Commaux, N.W. Eidietis, T.E. Evans, and *et al.* Measurements of hard X-ray emission from runaway electrons in DIII-D. *Nucl. Fusion*, **52**, 013007 (2012).
7. Z. Y. Chen, W.C. Kim, Y.W. Yu, A.C. England, J.W. Yoo, and *et al.* Study of runaway current generation following disruptions in KSTAR. *Plasma Phys. Control. Fusion*, **55**, 035007 (2013).
8. R. D. Gill, B. Alper, A. W. Edwards, L. C. Ingesson, M. F. Johnson, and D. J. Ward. Direct observations of runaway electrons during disruptions in the JET tokamak. *Nucl. Fusion*, **40**, 163–174 (2000).
9. R. Yoshino, S. Tokuda, and Y. Kawano. Generation and termination of runaway electrons at major disruptions in JT-60U. *Nucl. Fusion*, **39**, 151 (1999).
10. A. V. Gurevich and R. N. Sudan. Runaway electrons in plasma current sheets. *Phys. Rev. Lett.*, **72**, 645–648 (1994).
11. A.V. Gurevich, G.M. Milikh, and R. Roussel-Dupre. Runaway electron mechanism of air breakdown and preconditioning during a thunderstorm. *Phys. Lett. A*, **165**, 463 – 468 (1992).
12. F.C. Schüller. Disruptions in tokamaks. *Plasma Phys. Control. Fusion*, **37**, A135–A162 (1995).
13. J. R. Martín-Solís, R. Sánchez, and B. Esposito. Effect of magnetic and electrostatic fluctuations on the runaway electron dynamics in tokamak plasmas. *Phys. Plasmas*, **6**, 3925–3933 (1999).
14. M. Bakhtiari, G. J. Kramer, M. Takechi, H. Tamai, Y. Miura, Y. Kusama, and Y. Kamada. Role of bremsstrahlung radiation in limiting the energy of runaway electrons in tokamaks. *Phys. Rev. Lett.*, **94**, 215003 (2005).
15. D. G. Whyte, R. Granetz, M. Bakhtiari, V. Izzo, T. Jernigan, J. Terry, M. Reinke, and B. Lipschultz. Disruption mitigation on Alcator C-Mod us-

ing high-pressure gas injection: Experiments and modeling toward ITER. *J. Nucl. Mater.* **363-365**, 1160–1167 (2007).
16. E.M. Hollmann, T. C. Jernigan, P. B. Parks, J. A. Boedo, T. E. Evans,and *et al.* Measurements of injected impurity assimilation during massive gas injection experiments in DIII-D. *Nucl. Fusion*, **48**, 115007 (2008).
17. C. Reux, J. Bucalossi, F. Saint-Laurent, C. Gil, P. Moreau, and P. Maget. Experimental study of disruption mitigation using massive injection of noble gases on Tore Supra. *Nucl. Fusion*, **50**, 095006 (2010).
18. A. J. Thornton, K. J. Gibson, J. R. Harrison, A. Kirk, S. W. Lisgo, *et al.* Disruption mitigation studies on the Mega Ampere Spherical Tokamak (MAST). *J. Nucl. Mater.*, **415**, S836–S840 (2011).
19. G. Pautasso, D. Coster, T. Eich, J. C. Fuchs, O. Gruber, *et al.* Disruption studies in ASDEX Upgrade in view of ITER. *Plasma Phys. Control. Fusion*, **51**, 124056 (2009).
20. M. Lehnen, S. A Bozhenkov, S. S. Abdullaev, the TEXTOR team, and M. W. Jakubowski. Suppression of runaway electrons by resonant magnetic perturbations in TEXTOR disruptions. *Phys. Rev. Lett.*, **100**, 255003 (2008).
21. M. Forster, S.S. Abdullaev, K.H. Finken, T. Kudyakov, M. Lehnen, G. Sewell, O. Willi, Y. Xu, and the TEXTOR team. Runaway electron transport in turbulent and resonantly perturbed magnetic topologies of TEXTOR. *Nucl. Fusion*, **52**, 083016 (2012).
22. F. Saint-Laurent, C. Reux, J. Bucalossi, S. Bremond, C. Gil, P. Maget, Ph. Moreau, and J.L Seguin. Disruption and Runaways Electron Mitigation Studies on Tore Supra. In *Proc. 23th IAEA Fusion Energy Conference, 11-16 October 2010 Daejon, Korea*, Vienna, 2010. IAEA. EXS/P2-16.
23. N. W Eidietis, N. Commaux, E. M. Hollmann, D. A. Humphreys, T. C. Jernigan, and *et al.* Control of post-disruption runaway electron beams in DIII-D. *Phys. Plasmas*, **19**, 056109 (2012).
24. K. Wongrach, K.H. Finken, S.S. Abdullaev, R. Koslowski, O. Willi, L. Zeng, and the TEXTOR team. Measurement of synchrotron radiation from runaway electrons during TEXTOR tokamak disruptions. *Nucl. Fusion*, **54**, 043011 (2014).
25. R. J. E. Jaspers. *Relativistic Runaway Electrons in Tokamak Plasmas.* PhD thesis, Eidenhoven University of Technology, The Netherlands,
26. I. Entrop. *Confinement of relativistic runaway electrons in tokamak plasmas.* PhD thesis, Technical University of Eindhoven, Eindhoven, 1999.
27. P. Helander, L.-G. Eriksson, and F. Andersson. Runaway acceleration during magnetic reconnection in tokamaks. *Plasma Phys. Control. Fusion*, **44**, B247–B262 (2002).
28. R. H. Cohen. Runaway electrons in an impure plasma. *Phys. Fluids*, **19**, 239–244 (1976).
29. R. W. Harvey, V. S. Chan, S. C. Chiu, T. E. Evans, M. N. Rosenbluth, and D. G. Whyte. Runaway electron production in DIII-D killer pellet experiments, calculated with the CQL3D/KPRAD model. *Phys. Plasmas*, **7**, 4590–4599 (2000).
30. P. Helander, H. Smith, T. Fülöp, and L.-G. Eriksson. Electron kinetics in a cooling plasma. *Phys. Plasmas*, **11**, 5704–5709 (2004).
31. H. Smith, P. Helander, L.-G. Eriksson, and T. Fülöp. Runaway electron generation in a cooling plasma. *Phys. Plasmas*, **12**, 122505 (2005).

32. H. M. Smith and E. Verwichte. Hot tail runaway electron generation in tokamak disruptions. *Phys. Plasmas*, **15**, 072502 (2008).
33. P. L. Taylor, A. G. Kellman, T. E. Evans, D. S. Gray, D. A. Humphreys, and *et al.* Disruption mitigation studies in DIII-D. *Phys. Plasmas*, **6**, 1872–1879 (1999).
34. L. Zeng, H. R. Koslowski, Y. Liang, A. Lvovskiy, M. Lehnen, D. Nicolai, J. Pearson, M. Rack, P. Denner, K. H. Finken, and K. Wongrach. Experimental observation of hot tail runaway electron generation in TEXTOR disruptions. *J. Plasma Phys.*, **81**, 475810402 (2015).
35. Yu. A. Sokolov. Multiplication of accelerated electrons in a tokamak. *JETP Letters*, **29**, 218–221 (1979).
36. N.T. Besedin and I.M. Pankratov. Stability of a runaway electron beam. *Nucl. Fusion*, **26**, 807 (1986).
37. R. Jayakumar, H.H. Fleischmann, and S.J. Zweben. Collisional avalanche exponentiation of runaway electrons in electrified plasmas. *Phys. Lett. A*, **172**, 447 – 451 (1993).
38. M. N. Rosenbluth and S. V. Putvinski. Theory for avalanche of runaway electrons in tokamaks. *Nucl. Fusion*, **37**, 1355–1362 (1997).
39. P. Helander, L.-G. Eriksson, and F. Andersson. Suppression of runaway electron avalanches by radial diffusion. *Phys. Plasmas*, **7**, 4106–4111 (2000).
40. T. Fülöp, H. M. Smith, and G. Pokol. Magnetic field threshold for runaway generation in tokamak disruptions. *Phys. Plasmas*, **16**, 022502 (2009).
41. R. Jaspers, K. H. Finken, G. Mank, F. Hoenen, J. Boedo, N. J. Lopes Cardozo, and F. C. Schüller. Experimental investigation of runaway electron generation in TEXTOR. *Nucl. Fusion*, **33**, 1775 (1993).
42. R. Jaspers, N. J. Lopes Cardozo, F. C. Schüller, K. H. Finken, T. Grewe, and G. Mank. Disruption generated runaway electrons in TEXTOR and ITER. *Nucl. Fusion*, **36**, 367–374 (1996).
43. H. Smith, P. Helander, L.-G. Eriksson, D. Anderson, M. Lisak, and F. Andersson. Runaway electrons and the evolution of the plasma current in tokamak disruptions. *Phys. Plasmas*, **13**, 102502 (2006).
44. T Fehér, H M Smith, T Fülöp, and K Gál. Simulation of runaway electron generation during plasma shutdown by impurity injection in ITER. *Plasma Phys. Control. Fusion*, **53**, 035014 (2011).
45. S. S. Abdullaev and K. H. Finken. Hamiltonian guiding center equations in a toroidal system. *Phys. Plasmas*, **9**, 4193–4204 (2002).
46. A. Wingen, S. S. Abdullaev, K. H. Finken, and K. H. Spatschek. Influence of stochastic fields on relativistic electrons. *Nucl. Fusion*, **46**, 941–952 (2006).
47. S. S. Abdullaev. *Magnetic Stochasticity in Magnetically Confined Fusion Plasmas*. Springer-Verlag, Cham–Heidelberg, 2014.
48. S.S. Abdullaev. Drifts of electron orbits induced by toroidal electric field. *Phys. Plasmas*, **22**, 030702 (2015). 1995.
49. H. Knoepfel and D. A. Spong. Runaway electrons in toroidal discharges. *Nucl. Fusion*, **19**, 785–829 (1979).
50. H.P. Zehrfeld, G. Fussmann, and B. J. Green. Electric field effects on relativistic charged particle motion in tokamaks. *Plasma Physics*, **23**, 473 (1981).
51. X. Guan, H. Qin, and N.J. Fisch. Phase-space dynamics of runaway electrons in tokamaks. *Phys. Plasmas*, **17**, 092502 (2010).
52. A. A. Ware. Pinch effect for trapped particles in a tokamak. *Phys. Rev. Lett.*, **25**, 15-17 (1970).

53. J. Wesson. *Tokamaks*. Clarendon Press, Oxford, 3 edition, 2004.
54. S. J. Zweben, D. W. Swain, and H. H. Fleischmann. Radial transport of high-energy runaway electrons in ORMAK. *Nucl. Fusion*, **18**, 1679 (1978).
55. S. S. Abdullaev, K.H. Finken, T. Kudyakov, and M. Lehnen. Asymptotical theory of runaway electron diffusion due to magnetic turbulence in tokamak plasmas. *Contrib. Plasma Phys.*, **50**, 929–941 (2010).
56. S. S. Abdullaev, K.H. Finken, and M. Forster. New mechanism of runaway electron diffusion due to mircoturbulence in tokamaks. *Phys. Plasmas*, **19**, 072502 (2012).
57. S. S. Abdullaev. *Construction of Mappings for Hamiltonian Systems and Their Applications*. Springer-Verlag, Berlin Heidelberg, 2006.
58. R. J. Zhou, L. Q. Hu, E. Z. Li, M. Xu, G. Q. Zhong, L. Q. Xu, S. Y. Lin, J. Z. Zhang, and the EAST Team. Investigation of ring-like runaway electron beams in the EAST tokamak. *Plasma Phys. Control. Fusion*, **55**, 055006 (2013).
59. R. J. Zhou, I.M. Pankratov, L. Q. Hu, M. Xu, and J. H. Yang. Synchrotron radiation spectra and synchrotron radiation spot shape of runaway electrons in Experimental Advanced Superconducting Tokamak. *Phys. Plasmas*, **21**, 063302 (2014).
60. A. B. Rechester and M. N. Rosenbluth. Electron heat transport in a tokamak with destroyed magnetic surfaces. *Phys. Rev. Lett.*, **40**, 38–41 (1978).
61. T. H. Stix. Plasma transport across a braided magnetic field. *Nucl. Fusion*, **18**, 353–358 (1978).
62. A. H. Boozer and R. B. White. Particle diffusion in tokamaks with partially destroyed magnetic surfaces. *Phys. Rev. Lett.*, **49**, 786–789 (1982).
63. H. E. Mynick and J. Strachan. Transport of runaway and thermal electrons due to magnetic microturbulence. *Phys. Fluids*, **24**, 695–702 (1981).
64. J. R. Myra, P. J. Catto, A. J. Wootton, R. D. Bengtson, and P. W. Wang. Runaway electrons as a diagnostic of magnetic fluctuations in the edge plasma of the Texas Experimental Tokamak. *Phys. Fluids B*, **4**, 2092–2097 (1992).
65. J. R. Myra and P.J. Catto. Effects of drifts on the diffusion of runaway electrons in tokamak stochastic magnetic fields. *Phys. Fluids B*, **4**, 176–186 (1992).
66. J. R. Myra, P. J. Catto, H. E. Mynick, and R. E. Duvall. Quasilinear diffusion in stochastic magnetic fields: Reconciliation of drift-orbit modification calculations. *Phys. Fluids B*, **5**, 1160–1163 (1993).
67. M. de Rover, N. J. Lopes Cardozo, and A. Montvai. Hamiltonian description of the topology of drift orbits of relativistic particles in a tokamak. *Phys. Plasmas*, **3**, 4468–4477 (1996).
68. M. de Rover, N. J. LopesCardozo, and A. Montvai. Motion of relativistic particles in axially symmetric and perturbed magnetic fields in a tokamak. *Phys. Plasmas*, **3**, 4478–4488 (1996).
69. M. de Rover, A. M. Schilham, A. Montvai, and N. J. Lopes Cardozo. Test particle transport in perturbed magnetic fields in tokamaks. *Phys. Plasmas*, **6**, 2443–2451 (1999).
70. T. Hauff and F. Jenko. Runaway electron transport via tokamak microturbulence. *Phys. Plasmas*, **16**, 102308 (2009).
71. A. Matsuyama, M. Yagi, Y. Kagei, and N. Nakajima. Drift resonance effect on stochastic runaway electron orbit in the presence of low-order magnetic perturbations. *Nucl. Fusion*, 54(12):123007, 2014.

72. Y. Kawano, R. Yoshino, T. Kondoh, N. Isei, S. Ishida, K. Tobita, T. Hatae, K. Itami, S. Sakasai, and the JT-60 team. Suppression of runaways - electrons generation during disruptive discharge - termination in JT-60U. In *Controlled Fusion and Plasma Physics. Proc. 24-th Eur. Conf. Berchtesgaden, 1997*, volume 21A, pages 501–504, Geneva, 1997. European Physical Society.
73. S. Tokuda and R. Yoshino. Simulation study on collisionless loss runaway electrons by magnetic perturbations in a tokamak *Nucl. Fusion*, **39**, 1123–1132 (1999).
74. R. Yoshino and S. Tokuda. Runaway electrons in magnetic turbulence and runaway current termination in tokamak discharge. *Nucl. Fusion*, **40**, 1293–1309 (2000).
75. H. Tamai, R. Yoshino, S. Tokuda, *et al.*. Runaway current termination in JT-60U. *Nucl. Fusion*, **42**, 290–294 (2002).
76. M. Lehnen, S. S. Abdullaev, G. Arnoux, S. A Bozhenkov, M. W. Jakubowski, R. Jaspers, V. V. Plyusnin, V. Riccardo, U. Samm, JET EFDA Contributors, and the TEXTOR team. Runaway generation during disruptions in JET and TEXTOR. *J. Nucl. Mater.*, **390-391**, 740–746 (2009).
77. E.M. Hollmann, N. Commaux, N. W. Eidietis, T. E. Evans, D. A. Humphreys, and *et al.* Experiments in DIII-D toward achieving rapid shutdown with RE suppression. *Phys. Plasmas*, **17**, 056117 (2010).
78. G. Papp, M. Drevlak, T. Fülöp, P. Helander, and G-I. Pokol. Runaway electron losses caused by resonant magnetic perturbations in ITER. *Plasma Phys. Control. Fusion*, **53**, 095004 (2011).
79. G. Papp, M. Drevlak, T. Fülöp, and G-I. Pokol. The effect of resonant magnetic perturbations on runaway electron transport in ITER. *Plasma Phys. Control. Fusion*, **52**, 125008 (2012).
80. T. E. Evans. Resonant magnetic perturbations of edge-plasmas in toroidal confinement devices. *Plasma Phys. Control. Fusion*, **57**, 123001 (2015).
81. K. H. Finken, S. S. Abdullaev, M. Jakubowski, R. Jaspers, M. Lehnen, and O. Zimmermann. Losses of runaway electrons during ergodization. *Nucl. Fusion*, **46**, S139–S144 (2006).
82. K. H. Finken, S. S. Abdullaev, M. Jakubowski, R. Jaspers, M. Lehnen, R. Schlikeiser, K. H. Spatschek, R. Wolf, and the TEXTOR Team. Runaway losses in ergodized plasmas. *Nucl. Fusion*, **47**, 91–102 (2007).
83. R J Zhou, L Q Hu, E Z Li, M Xu, G Q Zhong, L Q Xu, S Y Lin. Effect of magnetic fluctuations on the confinement and dynamics of runaway electrons in the HT-7 tokamak. *Phys. Plasmas*, **20**, 032511 (2013).
84. H. R. Koslowski, L. Zeng, M. Lehnen, A. Lvovskiy, K. Wongrach, and TEXTOR Team. Influence of massive gas injection and resonant magnetic perturbations on the generation of runaway electrons during disruptions in TEXTOR. In *Proc. 41st EPS Conf. on Plasma Physics (Berlin, June 22-28, 2014)*, 2014. P5.028.
85. K. Wongrach, K. H. Finken, S. S. Abdullaev, O. Willi, L. Zeng, and Y. Xu. Structure of the runaway electron loss during induced disruptions in TEXTOR. *Phys. Plasmas*, **22**, 102508 (2015).
86. R. L. Tanna, J. Ghosh, P. K. Chattopadhyay, Pravesh Dhyani, Shishir Purohit, and *et al.* Novel approaches for mitigating runaway electrons and plasma disruptions in ADITYA tokamak. *Nucl. Fusion*, **55**, 063010 (2015).

87. M. Forster, K.H. Finken, T. Kudyakov, M. Lehnen, O. Willi, Y. Xu, L. Zeng, and the TEXTOR team. Temporal and spectral evolution of runaway electron bursts in TEXTOR disruptions. *Phys. Plasmas*, **19**, 092513 (2012).
88. W. Bernstein, F. F. Chen, M. A. Heald, and A. Z. Kranz. Runaway electrons and cooperative phenomena in B-1 stellarator discharges. *Phys. Fluids*, **1**, 430–437 (1958).
89. R. A. Ellis, L. P. Goldberg, and J. G. Gorman. Possibility of an electrostatic instability in a stellarator. *Phys. Fluids*, **3**, 797–799 (1960).
90. H. Knoepfel, D. A. Spong, and S. J. Zweben. Relativistic runaway electron beams in the Oak Ridge tokamak. *Phys. Fluids*, **20**, 511–519 (1977).
91. V.S. Vlasenkov, V.M. Leonov, V.G. Merezhkin, and V.S. Mukhovatov. The runaway electron discharge regime in the Tokamak-6 device. *Nucl. Fusion*, **13**, 509-516 (1973).
92. D. A. Boyd, F. J. Stauffer, and A. W. Trivelpiece. Synchrotron radiation from the ATC tokamak plasma. *Phys. Rev. Lett.*, **37**, 98–101 (1976).
93. P. H. Rebut, R. Dei-Cas, P. Ginot, J.P. Girard, M. Huguet, P. Lecoustey, P. Moriette, Z. Sledziewski, J. Tachon, and A. Torossian. Plasma–wall interactions in the TFR machine. *J. Nucl. Mater.*, **53**, 16–24 (1974).
94. U. Ascoli-Bartoli, C. Bosla, G. Boxman, P. Brossier, , B. Coppi, L. Dekock, B. Meddens, B. Montgomery, A. Oomens, L. Ornstein, R. Parker, L. Pieroni, S. Segre, R. Taylor, P. Van der Laan, and P. van Heyningen. High and low current density plasma experiments within the M.I.T. Alcator programme. In *Plasma Physics and Controlled Fusion (Proc. 5-th Int. Conf. Tokyo, 1975)*, Vienna, 1975. IAEA.
95. T. Kudyakov, K. H. Finken, M. Jakubowski, M. Lehnen, Y. Xu, and O. Willi. Spectral measurements of runaway electrons by a scanning probe in the TEXTOR tokamak. *Rev. Sci. Insrum.*, **79**, 10F126 (2008).
96. T. Kudyakov, A. Jochmann, K. Zeil, S. Kraft, K. H. Finken, U. Schramm, and O. Willi. High energy electron crystal spectrometer. *Rev. Scient. Instrum*, **80**, 076106 (2009).
97. T. Kudyakov. *Spectral measurements of runaway electrons in the TEXTOR tokamak*. PhD thesis, Universität Düsseldorf, Düsseldorf, Germany, 2009. PhD thesis.
98. M. Forster, K.H. Finken, M. Lehnen, J. Linke, B. Schweer, C. Thomser, O. Willi, Y. Xu, and the TEXTOR team. Energy deposition and radial decay of runaway electrons in a disruption at TEXTOR. *Nucl. Fusion*, **51**, 043003 (2011).
99. M. Forster, K. H. Finken, M. Lehnen, O. Willi, Y. Xu, and TEXTOR Team. Measurements of the runaway electron energy during disruptions in the tokamak TEXTOR. *Phys. Plasmas*, **19**, 052506 (2012).
100. M. Forster. *Runaway Electrons in Disruptions and Perturbed Magnetic Topologies of Tokamak Plasmas*. PhD thesis, Heinrich-Heine-Universität Düsseldorf, Düsseldorf, Germany, 2012.
101. D. D. Ivanenko and A. A. Sokolov. K teorii "svetyashego" elektrona (To the theory of a "luminous" electron). *Dokl. Akad. Nauk USSR*, **59**, 1551-1554 (1948).
102. J. Schwinger. On the classical radiation of accelerated electrons. *Phys. Rev.*, **75**, 1912–1925 (1949).
103. I. M. Pankratov. Analysis of the synchrotron radiation spectra of runaway electrons. *Plasma Phys. Reports*, **25**, 145–148 (1999).

104. Z.Y. Chen, B.N. Wan, S.Y. Lin, Y.J. Shi, and L.Q. Hu. Energy limit of runaway electrons in the HT-7 tokamak. *Phys. Lett. A*, **351**, 413 – 416 (2006).
105. Yuejiang Shi, Jia Fu, Jiahong Li, Yu Yang, Fudi Wang, Yingying Li, Wei Zhang, Baonian Wan, and Zhongyong Chen. Observation of runaway electron beams by visible color camera in the Experimental Advanced Superconducting Tokamak. *Rev. Sci. Instrum.*, **81**, 033506 (2010).
106. J. H. Yu, E. M. Hollmann, N. Commaux, N. W. Eidietis, D. A. Humphreys, A. N. James, T. C. Jernigan, and R. A. Moyer. Visible imaging and spectroscopy of disruption runaway electrons in DIII-D. *Phys. Plasmas*, **20**, 042113 (2013).
107. I. Entrop, R. Jaspers, N. J. Lopes Cardozo, and K. H. Finken. Runaway snakes in TEXTOR–94. *Plasma Phys. Control. Fusion*, **41**, 377 (1999).
108. R. Jaspers, N. J. Lopes Cardozo, A. J. H. Donné, H. L. M. Widdershoven, and K. H. Finken. A synchrotron radiation diagnostic to observe relativistic runaway electrons in a tokamak plasma. *Rev. Sci. Instrum.*, **72**, 466–470 (2001).
109. T. Kudyakov, K. H. Finken, M. Jakubowski, M. Lehnen, Y. Xu, B. Schweer, T. Toncian, G. Van Wassenhove, and O. Willi. Spatially and temporally resolved measurements of runaway electrons in the TEXTOR tokamak. *Nucl. Fusion*, **48**, 122002 (2008).
110. M. Balcerzyk, M. Moszynski, M. Kapusta, D. Wolski, J. Pawelke, and C.L. Melcher. YSO, LSO, GSO and LGSO. A study of energy resolution and nonproportionality. *IEEE Trans. Nucl. Sci.*, **47**, 1319–1323 (2000).
111. *YSO cristals produced by Proteus Inc.:* . http://www.proteus-pp.com.
112. S. Agostinelli, J. Allison, K. Amako, J. Apostolakis, H. Araujo, P. Arce, M. Asai, D. Axen, S. Banerjee, G. Barrand, and *et al.* Geant4–a simulation toolkit. *Nucl. Instrum. Meth. A*, **506**, 250–303 (2003).
113. J. Allison, K. Amako, J. Apostolakis, H. Araujo, P.A. Dubois, M. Asai, G. Barrand, R. Capra, and *et al.* Geant4 Developments and Applications. *IEEE Trans. Nucl. Sci.*, **53**, 270–278 (2006).
114. *Geant4 website:*. http://www.geant4.com//geant4.
115. M. J. Berger and *et al.* *Estar database online 1998.* http://www.nist.gov/pml/data/star/index.cfm.
116. R. Jaspers, N. J. Lopes Cardozo, K. H. Finken, B. C. Schokker, G. Fuchs G. Mank, and F. C. Schüller. Island of runaway electrons in the TEXTOR tokamak and relation to transport in a stochastic field. *Phys. Rev. Lett.*, **72**, 4093–4097 (1994).
117. T. Kudyakov, S.S. Abdullaev, S.A. Bozhenkov, K. H. Finken, M.W. Jakubowski, M. Lehnen, G. Sewell, O. Willi, Y. Xu, and the TEXTOR team. Influence of B_t on the magnetic turbulence and on the runaway transport in low-density discharges. *Nucl. Fusion*, **52**, 023025 (11 pp) (2012).
118. R. D. Bengtson, M. R. Freeman, A. J. Wootton, P. W. Wang, J. R. Myra, and P. J. Catto. Runaway electrons as a diagnostic of magnetic fluctuations (invited). *Rev. Sci. Instrum.*, **63**, 4595–4598 (1992).
119. L. Rodriguez-Rodrigo, A. Rodriguez-Yunta, F. Castejon, J. Vega, C. Pardo, and A.P. Navarro. Runaway transport studies in the TJ-I tokamak. *Nucl. Fusion*, **34**, 649 (1994).
120. I. Entrop, N. J. Lopes Cardozo, R. Jaspers, and K. H. Finken. Diffusion of runaway electrons in TEXTOR–94. *Plasma Phys. Control. Fusion*, **40**, 1513 (1998).

121. B. Esposito, R. Martin-Solis, P. van Belle, O. N. Jarvis, F. B. Marcus, and *et al.* Runaway electron measurements in the JET tokamak. *Plasma Phys. Control. Fusion*, **38**, 2035–2049 (1996).
122. G. Sewell. Solving PDEs in non-rectangular 3D regions using a collocation finite element method. *Advances in Engineering Software*, **41**, 748–753 (2010).
123. T. C. Hender, J. C Wesley, J. Bialek, A. Bondeson, A. H. Boozer, R. J. Buttery, A. Garofalo, T. P Goodman, R. S. Granetz, Y. Gribov, et al. the ITPA MHD, Disruption and Magnetic Control Topical Group. Progress in the ITER Physics Basis. Chapter 3: MHD stability, operational limits and disruptions. *Nucl. Fusion*, **47**, S128–S202 (2007).
124. K. Wongrach, K.H. Finken, S.S. Abdullaev, R. Koslowski, O. Willi, Y. Xu, L. Zeng, and the TEXTOR team. Runaway electron studies in TEXTOR. *Nucl. Fusion*, **55**, 053008 (2015).
125. I. Entrop, N. J. Lopes Cardozo, R. Jaspers, and K. H. Finken. Scale size of magnetic turbulence in tokamaks probed with 30–MeV electrons. *Phys. Rev. Lett.*, **84**, 3606–3609 (2000).
126. K. H. Finken, S. S. Abdullaev, M. Jakubowski, M. Lehnen, A. Nicolai, and K. H. Spatschek. *The structure of magnetic field in the TEXTOR-DED*, Forschungszentrum Jülich, Jülich, Germany, 2005.
127. S. S. Abdullaev, K.H. Finken, K. Wongrach, M. Tokar, H. R. Koslowski, O. Willi, L. Zeng, and the TEXTOR team. Mechanism of runaway electron beam formation during plasma disruptions in tokamaks. *Phys. Plasmas*, **22**,040704 (2015).
128. S. S. Abdullaev, K. H. Finken, K. Wongrach, M. Tokar, H. R. Koslowski, O. Willi, L. Zeng, and the TEXTOR team. Mechanisms of plasma disruption and runaway electron losses in the TEXTOR tokamak. *J. Plasma Phys.*, **81**, 475810501 (2015).
129. B. B. Kadomtsev. Behavior of disruptions in tokamaks. *Plasma Phys. Control. Fusion*, **26**, 217–226 (1984).
130. S. E. Kruger, D. D. Schnak, and C. R. Sovinec. Dynamics of the major disruption of a DIII-D plasma. *Phys. Plasmas*, **12**, 056113 (2005).
131. V. A. Izzo, D. A. Humphreys, and M. Kornbluth. Analysis of shot-to-shot variability in post-disruption runaway electron currents for diverted DIII-D discharges. *Plasma Phys. Control. Fusion*, **54**, 095002 (2012).
132. F. M. Levinton, M. C. Zarnstorff, S. H. Batha, M. Bell, R. E. Bell, and *et al.* Improved Confinement with Reversed Magnetic Shear in TFTR. *Phys. Rev. Lett.*, **75**, 4417–4420 (1995).
133. E. J. Strait, L. L. Lao, M. E. Mauel, B. W. Rice, T. S. Taylor, and *et al.* Enhanced confinement and stability in DIII-D discharges with reversed magnetic shear. *Phys. Rev. Lett.*, **75**, 4421–4424 (1995).
134. E.D. Fredrickson, M.G. Bell, G. Taylor, and S.S. Medley. Control of disruption-generated runaway plasmas in TFTR. *Nucl. Fusion*, **55**, 013006 (2015).
135. L. Zeng, H. R. Koslowski, Y. Liang, A. Lvovskiy, M. Lehnen, D. Nicolai, and *et al.* Experimental observation of a magnetic-turbulence threshold for runaway generation in the TEXTOR tokamak. *Phys. Rev. Lett.*, **110**, 235003 (2013).
136. E. M. Hollmann, M. E. Austin, J. A. Boedo, N. H. Brooks, N. Commaux, and *et al.* Control and dissipation of runaway electron beams created during rapid shutdown experiments in DIII-D. *Nucl. Fusion*, **53**, 083004 (2013).

137. S. S. Abdullaev. On collisional diffusion in a stochastic magnetic field. *Phys. Plasmas*, **20**, 082507 (2013).
138. S. N. Gerasimov, T.C. Hender, J. Morris, V. Riccardo, L.E. Zakharov, and JET EFDA Contributors. Plasma current asymmetries during disruptions in JET. *Nucl. Fusion*, **54**, 073009 (2014).
139. H. Soltwisch, W. Stodiek, J. Manickam, and J. Schlüter. Current density profiles in the TEXTOR tokamak. In *Proc. 11-th IAEA Conf. on Plasma Physics and Controlled Fusion Research, Kyoto, 13–20 November, 1986*, volume 1, pages 263–273, Vienna, 1987. IAEA. IAEA-CN-47/A-V-1.
140. M. Yamada, F.M. Livinton, N. Pomphrey, R. Budny, J. Manickam, and Y. Nagayama. Investigation of magnetic reconnection during a sawtooth crash in a high–temperature tokamak plasmas. *Phys. Plasmas*, **1**, 269–3276 (1994).
141. H Soltwisch and H R Koslowski. Sawtooth modulation of the poloidal field in textor under ohmic heating conditions. *Plasma Phys. Control. Fusion*, **37**, 667–678 (1995).
142. J. O'Rourke. The change in the safety factor profile at a sawtooth collapse. *Plasma Phys. Control. Fusion*, **33**, 289–296 (1991).
143. H. R. Koslowski, H. Soltwisch, and W. Stodiek. Polarimetric measurement of $m = 1$ sawtooth precursor oscillations in the TEXTOR tokamak. *Plasma Phys. Control. Fusion*, **38**, 271–278 (1996).
144. H Soltwisch and H R Koslowski. Observation of magnetic field perturbations during sawtooth activity in tokamak plasmas. *Plasma Phys. Control. Fusion*, **39**, A341–A349 (1997).
145. S. S. Abdullaev, K. H. Finken, and K. H. Spatschek. Asymptotical and mapping methods in study of ergodic divertor magnetic field in a toroidal system. *Phys. Plasmas*, **6**, 153–174 (1999).
146. V. Igochine, O. Dumbrajs, D. Constantinescu, H. Zohm, G. Zvejnieks, and ASDEX Upgrade Team. Stochastic sawtooth reconnection in ASDEX Upgrade. *Nucl. Fusion*, **46**, 741–751 (2006).
147. D. Constantinescu, O. Dumbrajs, V. Igochine, and B. Weyssow. On the accuracy of some mapping techniques used to study the magnetic field dynamics in tokamaks. *Nucl. Fusion*, **48**, 024017 (2008).
148. M. W. Jakubowski, O. Schmitz, S. S. Abdullaev, S. Brezinsek, K. H. Finken, and *et al.* Change of the magnetic-field topology by an ergodic divertor and the effect on the plasma structure and transport. *Phys. Rev. Lett.*, **96**, 035004 (2006).
149. R. B. White. *The Theory of Toroidally Confined Plasmas*. Imperial College Press, London, 3 edition, 2014.
150. A. M. Runov, D. Reiter, S. V. Kasilov, M. F. Heyn, and W. Kernbicher. Monte carlo study of heat conductivity in stochastic boundaries: Application to the TEXTOR ergodic divertor. *Phys. Plasmas*, **8**, 916–930 (2001).
151. Y. Feng, M. Kobayashi, T. Morisaki, S. Masuzaki, J. Miyazawa, and *et al.* Fluid features of the stochastic layer transport in LHD. *Nucl. Fusion*, **48**, 024012 (2008).
152. H. Frerichs, M. Clever, Y. Feng, M. Lehnen, D. Reiter, and O. Schmitz. Numerical analysis of particle recycling in the TEXTOR helical divertor. *Nucl. Fusion*, **52**, 023001 (2012).
153. J. M. Rax and R. B. White. Effective diffusion and nonlocal heat transport in a stochastic magnetic field. *Phys. Rev. Lett.*, **68**, 1523–1526 (1992).

Band / Volume 305
Untersuchungen zu suspensionsplasmagespritzten Wärmedämmschichtsystemen
N. Schlegel (2016), X, 136 pp
ISBN: 978-3-95806-118-7

Band / Volume 306
Laser processing for the integrated series connection of thin-film silicon solar cells
B. Turan (2016), xii, 188 pp
ISBN: 978-3-95806-119-4

Band / Volume 307
Development and Application of a Multiscale Model for the magnetic Fusion Edge Plasma Region
F. Hasenbeck (2016), 190 pp
ISBN: 978-3-95806-120-0

Band / Volume 308
Emissions of Biogenic Volatile Organic Compounds and Ozone Balance under Future Climate Conditions
C. Wu (2016), VI, 105 pp
ISBN: 978-3-95806-121-7

Band / Volume 309
Computerunterstützte Auslegung eines Brennstoffzellen-Batterie-Hybridsystems für die Bordstromversorgung
C. Krupp (2016), iii, 207 pp
ISBN: 978-3-95806-124-8

Band / Volume 310
Influence of H_2O, HCl and H_2S on the Release and Condensation of Trace Metals in Gasification
M. Benito Abascal (2016), XIX, 172 pp
ISBN: 978-3-95806-125-5

Band / Volume 311
Mechanical and Thermochemical Properties of Nano-structured Membranes for Gas Separation in Fossil-fired Power Plants
J. Zhang (2016), II, 134 pp
ISBN: 978-3-95806-126-2

Band / Volume 312
Development of Embedded Thermocouple Sensors for Thermal Barrier Coatings (TBCs) by a Laser Cladding Process
Y. Zhang (2016), II, 108 pp
ISBN: 978-3-95806-129-3

Band / Volume 313
Streamwater transit time distributions at the catchment scale: constraining uncertainties through identification of spatio-temporal controls
M. Stockinger (2016), XIX, 161 pp
ISBN: 978-3-95806-131-6

Band / Volume 314
Entwicklung eines metallbasierten Substratkonzepts für energieeffiziente Gastrennmembranen
J. A. Kot (2016), xi, 201 pp
ISBN: 978-3-95806-134-7

Band / Volume 315
Langzeitbeobachtung der Dosisbelastung der Bevölkerung in radioaktiv kontaminierten Gebieten Weißrusslands – Korma-Studie II (1998 – 2015)
P. Zoriy, H. Dederichs, J. Pillath, B. Heuel-Fabianek, P. Hill, R. Lennartz (2016), ca 104 pp
ISBN: 978-3-95806-137-8

Band / Volume 316
Oxidation Mechanisms of Metallic Carrier Materials for Gas Separation Membranes
M. Schiek (2016), 148 pp
ISBN: 978-3-95806-138-5

Band / Volume 317
Thermoschockverhalten und temperaturabhängige Eigenschaften kohlenstoffarmer und -freier Feuerfestwerkstoffe
A. Böhm (2016), VI, 153 pp
ISBN: 978-3-95806-139-2

Band / Volume 318
Theoretical and experimental studies of runaway electrons in the TEXTOR tokamak
S.S. Abdullaev, K.H. Finken, K. Wongrach, O. Willi (2016), X, 109 pp
ISBN: 978-3-95806-140-8

Energie & Umwelt /
Energy & Environment
Band / Volume 318
ISBN 978-3-95806-140-8